LUND UNIVERSITY

Comprehensive Gamma-Ray Spectroscopy of 62Zn and Studies of Nilsson Parameters in the Mass A = 60 Region

Gellanki, Jnaneswari

2013

COMPREHENSIVE GAMMA-RAY SPECTROSCOPY OF ^{62}Zn AND STUDIES OF NILSSON PARAMETERS IN THE MASS $A = 60$ REGION

JNANESWARI GELLANKI

DIVISION OF NUCLEAR PHYSICS
DEPARTMENT OF PHYSICS
LUND UNIVERSITY
SWEDEN

FACULTY OPPONENT : Prof. MARK RILEY,
DEPARTMENT OF PHYSICS, FLORIDA STATE UNIVERSITY, USA

ACADEMIC DISSERTATION WHICH, BY THE PERMISSION OF THE FACULTY OF SCIENCE AT LUND UNIVERSITY, WILL BE PUBLICLY DEFENDED ON MONDAY THE 16^{th} OF SEPTEMBER 2013 AT 15.15 IN LECTRUE HALL B AT THE DEPARTMENT OF PHYSICS, SÖLVEGATAN 14A, LUND.

Organization LUND UNIVERSITY Department of Physics Box 118 SE-22100 Lund Sweden	Document name DOCTORAL DISSERTATION Date of issue August 15th, 2013 Sponsoring organization
Author(s) Jnaneswari Gellanki	

Title and subtitle

Comprehensive Gamma-Ray Spectroscopy of ^{62}Zn and Studies of Nilsson Parameters in the Mass A ~ 60 Region

Abstract

Comprehensive experimental knowledge of the ^{62}Zn nucleus has been obtained from the combined statistics of four different experiments. The Gammasphere Ge-detector array in conjunction with the 4π charged-particle detector array Microball was used to detect the γ-rays in coincidence with evaporated light charged particles. In total twenty seven band structures have been observed in ^{62}Zn, twenty for the first time. The resulting extensive decay scheme comprises almost 260 excited states, which are connected with more than 450 γ-ray transitions. The multipolarities have been determined for the γ-ray transitions and as a result spin-parity assignments are given for nearly all energy levels. The collective structures are compared with results from configuration dependent Cranked Nilsson-Strutinsky calculations.

The effective alignment method has been applied to check out the spin, parity and theoretical configuration assignments of the existing experimental bands and thereby identify the behaviour of the band structures in the A ~ 60 mass region. Confirmed experimental bands and their theoretical configuration assignments are used to investigate an improved Nilsson parameter set in the A ~ 60 mass region. These new Nilsson parameters give an improved overall description of data.

Key words: High-spin gamma-ray spectroscopy, Superdeformed bands, 62Zn, Cranked Nilsson- Strutinsky, Effective alignments.

Classification system and/or index termes (if any):

Supplementary bibliographical information:		Language English
ISSN and key title:		ISBN 978-91-7473-619-9
Recipient's notes	Number of pages 126	Price
	Security classification	

Comprehensive Gamma-ray Spectroscopy of ^{62}Zn and Studies of Nilsson Parameters in the Mass $A \sim 60$ Region
Thesis for the Degree of Doctor of Philosophy

Printed in Sweden by Mediatryck, Lund, 2013

Division of Nuclear Physics
Department of Physics
Lund University
Box 118
SE-221 00 Lund
Sweden

ISBN: 978-91-7473-619-9
LUNFD6 / (NFFR - 3112)/ 1-123 / (2013)

Typeset by the author using LaTeX 3.141592
The coverpage picture is used with the permission from the editor and taken from CERN Courier March 2002 p15.

List of Publications

This thesis is based on the results presented in the following publications and submitted manuscripts.

PAPER I: **Characterization of superdeformed bands in ^{62}Zn**
Phys. Rev. C **80**, *051304(R) (2009).*
J. Gellanki, I. Ragnarsson, D. Rudolph, C.E. Svensson, L.-L. Andersson, C. Andreoiu, C. Baktash, M.P. Carpenter, R.J. Charity, C.J. Chiara, J. Eberth, J. Ekman, C. Fahlander, D.S. Haslip, E.K. Johansson, D.R. LaFosse, S.D. Paul, O.L. Pechenaya, W. Reviol, R. du Rietz, D.G. Sarantites, D. Seweryniak, L.G. Sobotka, H.G. Thomas, D.A. Torres, J.C. Waddington, J.N. Wilson, C.H. Yu and S. Zhu.

PAPER II: **High-spin structure studies in ^{62}Zn**
*Proceedings Nordic Conference on Nuclear Physics 2011- Phys. Scr. T***150**, *014013 (2012).*
J. Gellanki, D. Rudolph, I. Ragnarsson, L.-L. Andersson, C. Andreoiu, M.P. Carpenter, J. Ekman, C. Fahlander, E.K. Johansson, W. Reviol, D.G. Sarantites, D. Seweryniak, and C.E. Svensson.

PAPER III: **Extensive γ-ray spectroscopy of band structures in $^{62}_{30}$Zn$_{32}$**
Phys. Rev. C **86**, *034304 (2012).*
J. Gellanki, D. Rudolph, I. Ragnarsson, L.-L. Andersson, C. Andreoiu, M.P. Carpenter, J. Ekman, C. Fahlander, E.K. Johansson, A. Kardan, W. Reviol, D.G. Sarantites, D. Seweryniak, C.E. Svensson, and J.C. Waddington.

PAPER IV: **Comparative study of rotational bands in the A $\sim$ 60 mass region - modification of Nilsson parameters**
To be submitted to *Phys. Rev. C* .
J. Gellanki, B.G. Carlsson, I. Ragnarsson, and D. Rudolph.

PAPER V: **Single-particle structure and highly-deformed bands in ^{63}Ni**
To be submitted to *Phys. Rev. C* .
M. Albers, S. Zhu, R.V.F. Janssens, J. Gellanki,
I. Ragnarsson, M. Alcorta, T. Baugher, P.F. Bertone,
M.P. Carpenter, C.J. Chiara, P. Chowdhury, A.N. Deacon,
A. Gade, C.R. Hoffman, F.G. Kondev, T. Lauritsen,
C.J. Lister, E.A. McCutchan, D.S. Moerland, A.M. Rogers,
and D. Seweryniak.

Author's Contribution

Paper I: Carried out the data analysis, engaged in theoretical interpretation, and drafting main parts of the manuscript as first author.

Paper II and III: Carried out the data analysis, performed the calculations, and drafted the manuscript as first author.

Paper IV: Carried out the theoretical calculations and drafted the manuscript as first author.

Paper V: On the basis of the results outlined in paper IV, I contributed to the theoretical interpretation. The new Nilsson parameters have been applied for the first time to interpret recent data in the $A \sim 60$ mass region.

Contents

Chapter 1

Introduction

1.1 High-Spin Physics

The atomic nucleus is a quantum mechanical many body system. To understand such a system is the challenging task in nuclear physics. From the discoveries in 1911 and 1932 by Ernest Rutherford and James Chadwick, respectively, it was concluded that almost all of the mass in an atom is made up from nucleons, the protons and neutrons inside the atomic nucleus, and the contribution from the electrons orbiting around the nucleus is very small. The arrangement of the electrons outside the nucleus gives the chemical properties of a substance, whereas the arrangement of nucleons inside the nucleus determines the stability of the nucleus.

The proton and neutrons occupy well-defined orbitals inside the nucleus, which specify the energy, angular momentum and the different kinds of shapes of the nucleus. Since the nuclear forces are strong and of short range, a nucleon will mainly interact with neighbouring nucleons. So the nucleons inside the nucleus are tightly bound, whereas the nucleons on the surface are less bound. A nucleus with magic numbers, 2, 8, 20, 28, 50, 82 and 126 protons or neutrons, is usually more stable than neighbouring nuclei. By adding valence nucleons or valence holes relative to a shell closure, nuclei start to become deformed.

The high-spin states of atomic nuclei refer to the quantal states with high angular momentum. In case of spherical or nearly spherical nuclei, these states are formed from the alignment of spin vectors of excited particles step by step, which typically leads to an irregular level structure. The case with deformed nuclei, where a group of or all nucleons involved in nuclear rotation, is generally referred to as collective motion. Here, the entire nucleus appears to rotate about an axis perpendicular to the symmetry

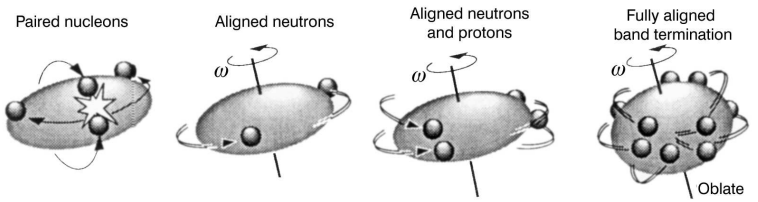

Figure 1.1: Schematic illustration of the building of angular momentum in a rotational band from the collective rotation to a non-collective terminating state. Figure taken from [1]. See text for details.

axis, leading to a regular level structure, with a rotational energy which is approximately a quadratic function of angular momentum.

Some "hot topics" in high-spin studies of nuclei are, for example, shape coexistence, superdeformation, band termination, or octupole correlations. The present work on ^{62}Zn involves some of the mentioned phenomena like band termination and superdeformation. Some details on these phenomena are presented in the following.

1.1.1 Band Termination

The interplay between collective and non-collective degrees of freedom is important in high-spin studies. According to the mean-field approximation, each nucleon occupies a well-defined orbital. For a spherical core, the total angular momentum contribution from the core is almost vanishing. Here, the addition of valence nucleons can only contribute a finite amount of angular momentum. The maximum spin will be determined by the maximal coupling of the single-particle spins for the valence particles and/or holes.

Nuclei which have a small number of valence nucleons outside the core will generate little collectivity. On the other hand, a higher number of nucleons outside the core will lead to high collectivity already at low or intermediate spin values. At rapid rotation of the nucleus, a combination of classical mechanical forces, like Coriolis and centrifugal forces, can break the pairs of valence nucleons and align the spin vectors of the individual nucleons along the rotational axis, in accordance with the Pauli exclusion principle. For high angular momentum, more valence nucleon pairs need to be broken. Once all valence nucleons are aligned along the rotational axis, they tend to polarize the nucleus towards an oblate shape, corresponding to a non-collective state. So, the nuclei evolve from collective rotation at low or medium spin to a non-collective or single-particle

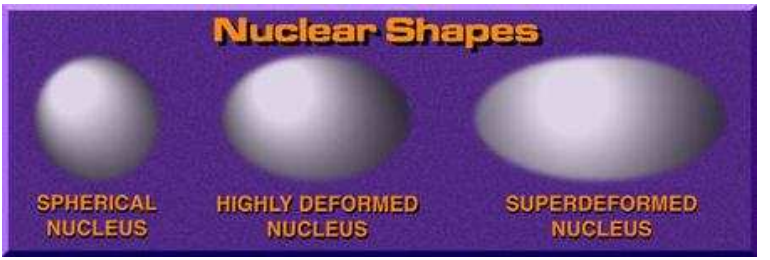

Figure 1.2: Possible nuclear shapes in the $A \sim 60$ mass region. Picture taken from [2].

mode at high-spin corresponding to a " band termination" [1]. Figure 1.1 shows the building of angular momentum in a rotational band ending up in a fully aligned terminating state. Here, the motion is collective at low-spin with paired nucleons, while at intermediate spin, nucleon pairs are broken and start to align their spin vectors along the rotational axis and finally, at high-spin, fully aligned nucleons which is called a terminating state.

Band termination is normally referred to as a specific nucleonic configuration. Different configurations can terminate at different I_{max} spin states. At large deformations, sometimes the specific band configuration may not terminate due to mixing between j-shells [3, 4].

1.1.2 Superdeformation

Figure 1.2 illustrates possible shapes experimentally found or predicted by theoretical models in the $A \sim 60$ mass region. They range from spherical nuclei to quadrupole deformed, highly and superdeformed (SD) nuclei. At fast rotation, some nuclei prefer elongated shapes having an axial deformation corresponding to a major-to-minor axis ratio $\sim$ 2:1. These are the ones called superdeformed nuclei, and have large quadrupole moments. The existence of superdeformed shapes in nuclei was for the first time observed at low-spin in actinide fission isomers [5].

The regions where superdefomed nuclei have been observed are those nuclei with proton and neutron numbers which correspond to large shell gaps at large prolate deformation. Theoretical existence of SD structures was explained by the existence of secondary energy minima in the nuclear potential energy surface at a higher quadrupole deformation than the nuclear ground state. Figure 1.3 shows the separation of the first and second minimum of the nuclear potential by an energy barrier.

The linking transitions between SD bands and normal deformed (ND)

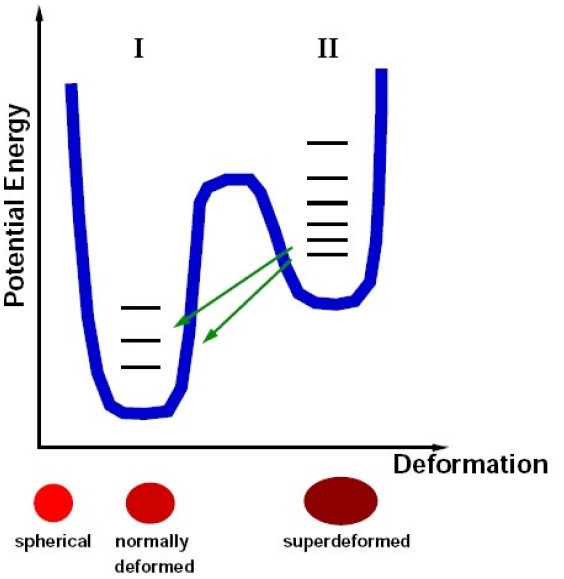

Figure 1.3: The potential energy of a nucleus versus the deformation. Picture taken from [6].

states can be used to determine the fundamental quantum numbers of the SD states, like spin, parity and excitation energy. The decays within superdeformed bands are experimentally characterised by very fast and long cascades of regularly spaced $E2$ (electric quadrupole) transitions. These decay transitions correspond to large moments of inertia, which are highly collective and have large transitional quadrupole moments. The linking transitions are usually very difficult to observe due to their low intensity. So far more than 300 superdeformed rotational bands have been observed and studied in different regions across the nuclear mass range. For instance, in each of the mass regions, $A \sim 40$ [7], $A \sim 60$ [8], $A \sim 80$ [9], $A \sim 130$ [10], $A \sim 150$ [11] and $A \sim 190$ [12] superdeformed bands have been observed.

1.1.3 Why is the $A \sim 60$ Mass Region of Interest ?

An interesting feature in the $A \sim 60$ mass region is that the same nuclei can exhibit various kinds of the nuclear high-spin phenomena, like band termination, highly deformed bands, superdeformed bands, prompt proton decays (band decays by both γ-ray transitions and by prompt proton emission towards the daughter nucleus) and shape changes (see, for example, Refs. [13, 14, 15, 16, 17]). To generate the high-spin states required for the observation of most of the collective phenomena, it is necessary to break the doubly magic $N = Z = 28$ ^{56}Ni core and to excite nucleons into the intruder $1g_{9/2}$ subshell. Starting at normal deformation (ND) with a few particles in the upper fp shell outside the core, the nuclei in this mass region become highly deformed and superdeformed (SD), when the number of holes in the $1f_{7/2}$ orbital and particles in the $1g_{9/2}$ orbital rapidly increase with spin and excitation energy. The superdeformed band in ^{60}Zn [18] built on the SD shell gaps at $N = Z = 30$, is treated as doubly-magic SD core in the $A \sim 60$ region.

For the rotational sequences of the nuclei in the $A \sim 60$ region, one can expect "smooth band termination" [19] with a smaller number of valence particles than in the heavier nuclei. The "smooth band termination" was first discovered in the $A \sim 110$ [20] region. It is characterized by a continuous transition within one configuration from large collectivity at low or intermediate values to a non-collective terminating state at the highest possible spin value. The nuclei in the $A \sim 60$ region exhibit a variety of excitations, both single-particle and collective with different shapes, namely prolate, oblate and triaxial.

In contrast to the other mass regions, almost all superdeformed bands in the second minima of the nuclear potential can be connected with the normal deformed, or spherical states in the first minimum of the nuclear potential. There are some differences between the $A \sim 60$ mass region and other heavy mass regions. For example, in the $A \sim 190$ mass region, the observed decay-out is dominated by $E1$ transitions expected in a statistical decay process, whereas in the $A \sim 60$ mass region, the observed decay-out transitions are often of stretched $E2$ character with a non-statistical mechanism [18, 21].

Superdeformed nuclei in this mass region are also of interest because they are the fastest rotating nuclei ($\hbar\omega \geq 2.0$ MeV). They are self-conjugate or nearly self-conjugate, which allows the investigation of sensitive properties such as isospin $T = 0$ pairing correlations (neutron and proton isoscalar interactions) in SD nuclei, as seen in $A \sim 100$ mass region [22].

Chapter 2

Experimental Tools

2.1 Fusion-evaporation Reactions

Nuclear high-spin and superdeformed states are populated experimentally in fusion-evaporation reactions. When a beam particle hits a target nucleus, two nuclei can fuse with a certain probability and form a compound nucleus. The fusion process will occur only if the incident kinetic energy of the beam particles is higher than the Coulomb barrier in order to overcome the Coulomb repulsion between two positively charged nuclei. The kinetic energy of the collision in the center-of-mass frame is partly converted into excitation energy of the compound system. The amount of angular momentum transferred to the compound nucleus is to first approximation $l = mvb$, where mv is the linear momentum of the beam particles and b is the impact parameter. Thus higher incident beam energies result in larger angular momentum transfer to the compound system. Figure 2.1 shows the process of the fusion-evaporation reaction.

A highly excited compound nucleus is formed with the excitation energy

$$E_{ex} = E_{CN} + Q \tag{2.1}$$

where Q is the Q value of the reaction and E_{CN} is the kinetic energy of the collision which is transferred to the compound system. It is calculated from the formula

$$E_{CN} = E_B(\frac{M_T}{M_T + M_B}) \tag{2.2}$$

where E_B is the kinetic energy of the beam, while M_B and M_T are the masses of the beam and target nucleus, respectively. The maximum angular momentum, l_{max}, that can be transferred to the compound nucleus

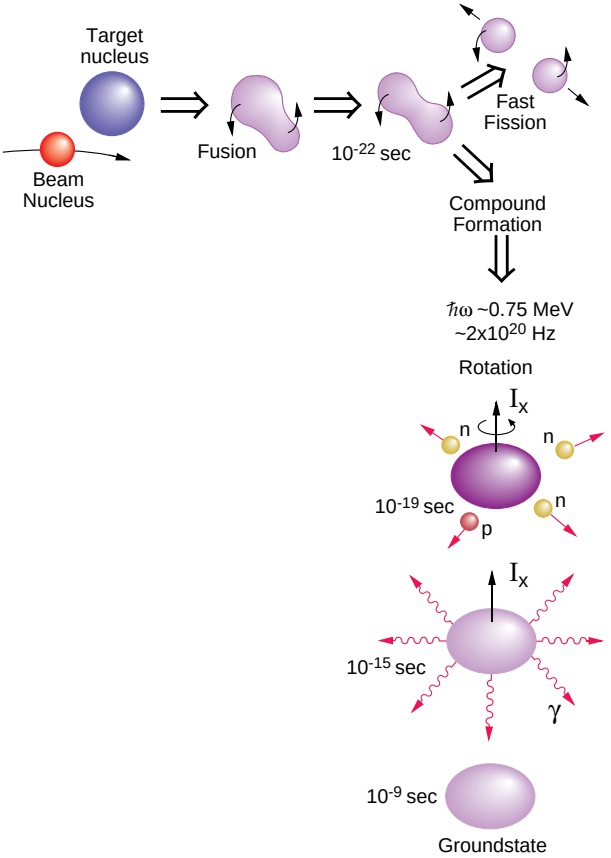

Figure 2.1: Schematic drawing of the fusion evaporation reaction process. Picture taken from [23].

is

$$l_{max} = \sqrt{2}(\frac{R}{\hbar})(\sqrt{\mu(E_{CN} - V_c)}) \tag{2.3}$$

where R is the maximum nucleus-nucleus distance for which a reaction can occur. The reduced mass of the system μ, is given by

$$\mu = \frac{M_B M_T}{M_B + M_T} \tag{2.4}$$

and V_c is Coulomb barrier energy.

The present study is mainly based on data from a fusion-evaporation reaction using a 122 MeV ^{28}Si beam on a ^{40}Ca target, which gives the compound nucleus ^{68}Se. The Q value for this reaction is -2 MeV and using Eq. 2.2 we get $E_{CN} \approx 71$ MeV. The excitation energy of the compound nucleus then becomes ≈ 69 MeV and the maximum angular momentum, l_{max}, that can be transferred to the compound nucleus is 42 $\hbar$.

The compound nucleus, which is at high excitation energy, cools down by evaporating light particles such as protons, neutrons and α-particles leading to different residual nuclei. The cooling process is an efficient way of reducing the excitation energy in the compound nucleus, since the evaporated particles take away energy from the compound system. For example, α particles take away ≈ 15 MeV, protons ≈ 6 MeV and neutrons ≈ 2 MeV. The species of the residual nuclei depends on the kind and number of evaporated particles. The overall time taken for this process is approximately 10^{-19} s. Since the evaporated light particles can only carry away a few units of angular momentum, the residual nucleus is typically left in an excited state with high angular momentum at large excitation energy.

In the neutron deficient $A \sim 60$ region, evaporation of protons and α-particles is more likely than emitting neutrons. This is due to the higher neutron separation energy of ≈ 15 MeV, compared to the proton separation energy of ≈ 5 MeV. In our study, the compound nucleus ^{68}Se evaporates one α and two proton particles leading to the nucleus of interest ^{62}Zn. The highly excited residual nucleus de-excites to the ground state by sending out first statistical and then, as the nucleus approaches the yrast line, discrete γ-rays. The yrast line is the line connecting the yrast states. The yrast state is the lowest energy state for a given value of angular momentum. The time scale for the nucleus to reach its ground state is about 10^{-9} s, as long as the decay path does not invovle any long lived, isomeric states. The discrete γ-rays are detected in the experiment making it possible to find out the nuclear structure properties of residual nuclei.

2.2 Gamma-Ray Detection

Because of their high-energy resoultion, germanium detectors are a popular choice for resolving the collection of γ-rays emitted from the residual nuclei of interest. In the mass $A \sim 60$ region, the interesting γ-ray energies range from 0.1 MeV to 6.0 MeV. Cylindrically closed ended coaxial shaped Ge detectors are most frequently used as opposed to planar and open-ended coaxial shaped detectors. The sensitive volume in the former one is larger than in the other two, resulting in smaller leakage current at the front surface of the detector [24]. Normally, for a cylindrically shaped Ge detector with diameter and length of 7-9 cm, the energy resolution is

about 2 keV at an incident γ-ray energy of 1 MeV.

The three major interaction mechanisms of γ-rays in matter are photoelectric absorption, Compton scattering and pair production. In all these interactions the incident γ-ray photon transfers its energy partially or completely to an electron and/or a positron which transfer their kinetic energy to the detector material. Photoelectric absorption is favoured for low-energy γ-rays, whereas pair production is favoured for high-energy γ-rays, and Compton scattering lies in between these energy extremes [24].

In the photoelectric absorption the incident γ-ray photon is completely absorbed in the germanium crystal and disappears. In a Compton scattering process the incident γ-ray photon transfers a portion of its energy to the germanium crystal electrons. The remaining part can escape the detector volume. This escaped photon energy results in a potentially large amount of Compton continuum background events. A BGO ($Bi_4Ge_3O_{12}$) shield around the Ge detector can be used to suppress this background. This shield acts as a veto for Compton events which scatter out of the germanium detector. If the γ-ray energy exceeds 1.02 MeV, i.e twice the rest mass energy of an electron, then the pair production process is energetically possible. In this interaction, the γ-ray photon disappears and the excess energy carried by the photon appears as kinetic energy shared by the electron-positron pair.

Practically, it is impossible to measure all of the individual γ-rays in a cascade with 100% efficiency. Over the last two decades this problem has been minimized by using modern germanium detector arrays such as GAMMASPHERE [25], EUROBALL [26] and GASP [27]. The present data analysis concerning the ^{62}Zn nucleus has been done with data from GAMMASPHERE array.

2.3 GAMMASPHERE

The Ge-detector array, GAMMASPHERE, is presently located at Argonne National Laboratory in the U.S.A. At the time of the experiment the array contained 103 high purity germanium detectors shielded by Compton-suppressing BGO detectors. The Ge detectors are arranged in a 4π geometry. Figure 2.2 shows the structure of the array. If the γ-ray multiplicity is high, it is possible that two, or more, emitted γ-rays hit the Ge detector and its surrounding BGO shield at the same time. The BGO detector will then veto a good event. To minimise this possibility Heavimet absorbers can be placed in front of the BGO detectors. The Gammasphere array has a full-energy peak efficiency of $\sim 9\%$ at a γ-ray energy of 1.33 MeV. In practice, the overall energy resolution is typically about 2.6 keV at the same γ-ray energy.

Figure 2.2: Ge detectors in the Gammasphere array [25]. Picture taken from [23].

2.4 Charged Particle Balls

For a very neutron deficient compound nuclear system, it is easier for protons and α-particles to tunnel through the Coulomb barrier due to their small separation energies compared to the compound nuclei closer to stability. This means that the emission of charged particles will dominate over neutron emission. This leads to the population of a large number of different nuclei with different cross sections for the selected beam - target combination. In order to detect the particular nuclei of interest, reaction channel selection methods are used. One method of channel selection is the selection of a specific reaction channel by gating on the appropriate kind and number of evaporated particles. For this purpose, charged particle balls are used to detect and discriminate evaporated charged particles

from the compound nucleus.

2.5 Microball

Scintillation detectors are often used for charged-particle detection due to their large light output with high efficiency. Microball is a scintillator detector array consisting of 95 CsI(Tl) elements which are situated in 9 rings in a 4π geometry (see Fig. 2.3). The array is located in the center of GAMMASPHERE. The 9 rings of detectors cover the angles between 4.0° and 171° with respect to the beam axis. The reaction kinematics produces particles which are strongly focused at forward angles. Therefore, the two most forward rings of detectors are positioned at large distances from the target resulting in a higher granularity. The Microball detector measures the energies and the directions of the emitted charged particles. The charged particles are discriminated by pulse shape techniques [28]. CsI(Tl) detectors

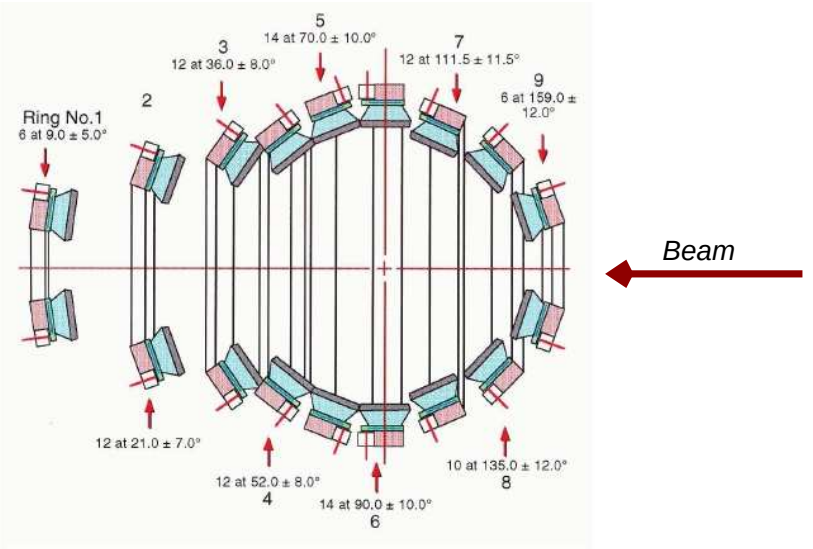

Figure 2.3: Schematic drawing of the CsI Microball detector array. Picture taken from [29].

provide different decay times for evaporated charged particles. The decay time from the CsI(Tl) detector has a slow and fast component, where the latter but not the former depends on the detected particle type. A charge

ratio is measured between these components which is thus used to separate the charged particles [6]. The average total efficiency of Microball in the present experiments is about 80% for protons and 70% for α- particles. Thick Pb or Ta absorber foils were placed in front of the CsI(Tl) detectors to stop heavy high-energy particles, like scattered beam and target particles.

2.6 Overview of the Experiments

The γ-ray transitions of the ^{62}Zn nucleus under study were resolved by using the combined statistics of four different experiments performed at Argonne and Lawerence Berkele National Laboratories. These transitions were used to construct the level scheme of the nucleus. A brief overview of the experiments is given in Table 2.1. More detailed explanations about these experiments are given in [14, 16, 30, 31, 32, 33, 34].

Table 2.1: Details of the fusion-evaporation reaction experiments which the present work is based on. CN: refers to compound nucleus and GS: short form of Gammasphere.

GSFMA66	GS54	GSFMA42	GSFMA138
^{28}Si+ ^{40}Ca	^{36}Ar+ ^{28}Si	^{36}Ar+ ^{28}Si	^{36}Ar+ ^{28}Si
E_B = 122 MeV	E_B = 143 MeV	E_B = 148 MeV	E_B = 134 MeV
CN: ^{68}Se	CN: ^{64}Ge	CN: ^{64}Ge	CN: ^{64}Ge
channel: 1α 2p	channel: 2p	channel: 2p	channel: 2p
GS: (103 Ge)	GS: (82 Ge)	GS: (86 Ge)	GS: (77 Ge)
Microball	Microball	Microball	Microball
	neutron detectors	neutron detectors	neutron detectors
		Si- strip detectors	Si- strip detectors
$\sigma_{rel} \approx 30$ %	$\sigma_{rel} \leq 1\%$	$\sigma_{rel} \leq 1\%$	$\sigma_{rel} \leq 1\%$

2.6.1 GSFMA66 Experiment

The 0.5 mg/cm^2 thin ^{40}Ca target was enriched to 99.975 %. It was sandwiched between two thin layers of Au to prevent oxidation. The beam consisted of ^{28}Si and was accelerated to an energy of 122 MeV. In this reaction the compound nucleus was ^{68}Se, and ^{62}Zn was populated in the 1α2p channel. The experimental setup consisted of the Gammasphere array in conjunction with the Microball array. The Heavimet collimators were removed from the Ge detectors to enable γ-ray multiplicity and sum-energy

measurements [35] and additional channel selectivity based on total energy conservation requirements [36]. No neutron detectors were used in this experiment.

The population cross section for the ^{62}Zn nucleus is $\approx 30\%$ of the total cross section. The statistics from this experiment is called data set 1. This experimental data is the primary source used to construct the level scheme of ^{62}Zn, i.e it is used to identify the different structures and rotational bands, including the superdeformed bands and their decay-out transitions.

2.6.2 GS54, GSFMA42, GSFMA138 Experiments

All three experiments utilize fusion-evaporation reactions with the same beam, ^{36}Ar, and target nuclei, ^{28}Si, and similar beam energies, ~ 140 MeV. Evaporated charged particles were detected in different combinations of charged-particle detectors. The relative yield of ^{62}Zn in the 2p channel is very small in these three experiments. The combined statistics of these data sets is called data set 2, and was used to add the highest-spin states of the superdeformed bands.

Chapter 3

Data Analysis Tools

3.1 Energy Calibration Sources

Energy calibration of a detector is the process of determining the energies of the unknown with known energy sources. Different types of calibration sources were used in the experiments mentioned in Sec. 2.6 in Table 2.1. The energy and efficiency calibrations of the GAMMASPHERE detectors were done using γ-ray energies from ^{56}Co, ^{133}Ba, ^{152}Eu and ^{228}Th γ-ray sources. The Microball detector calibration has been made by using the peaks produced from the elastic scattering of a beam of protons and α-particles with energies 12 and 48 MeV on ^{197}Au and inelastic scattering at the same beam energies of a ^{12}C target.

3.2 $\gamma\gamma$ and $\gamma\gamma\gamma$ Coincidence Analysis

The events in all the specified experiments in Table 2.1, were sorted offline into various E_γ projections, $E_\gamma - E_\gamma$ correlation matrices and $E_\gamma - E_\gamma - E_\gamma$ cubes subject to appropriate evaporated-particle conditions. Gating $E_\gamma - E_\gamma$ matrices creates a spectrum containing the γ-rays which are in coincidence with the transition chosen to be gate. These matrices contain a large amount of statistics but they generally comprise a high background level due to doublets or some remaining contamination from other reaction channels. In the case of the $E_\gamma - E_\gamma - E_\gamma$ cube, the gated spectrum contains the coincidence events with two γ-ray transitions which are also in coincidence with each other. The triple coincidences naturally result in a cleaner analysis but require a larger amount of events. The present analysis was restricted to events in which all of the evaporated charged particles, that is,

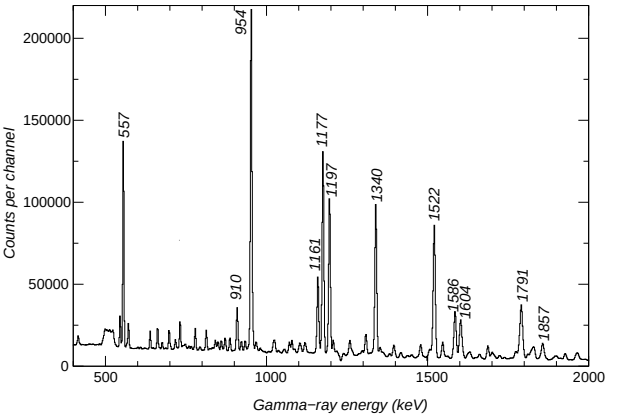

Figure 3.1: Coincidence γ-ray spectrum with a transition at 1232 keV, which depopulates the state at an excitation energy of 2186 keV in ^{62}Zn. See text for details.

two protons in the case of data set 2 and an additional α particle for data set 1, were detected. For data set 1, in total 2.3×10^9 coincidence events were collected, with a $\gamma\gamma\gamma\gamma$ trigger condition.

Figure 3.1 shows the coincidence γ-ray spectrum resulting from the γ-ray gate on the 1232 keV transition, which depopulates the state at an excitation energy 2186 keV in ^{62}Zn. The spectrum is created via the $E_\gamma - E_\gamma$ matrix. The ground state γ-ray transition at 954 keV has the highest coincidence rate with the 1232 keV transition. Other intense transitions at 557, 910, 1161, 1177, 1197, 1340, 1522, 1586, 1604, 1791 and 1857 keV are marked. Several low intensity coincidences are also clearly visible in the figure.

The study of ^{62}Zn relies on a $\gamma\gamma\gamma$ cube created with data set 1 and analyzed with the RADWARE analysis package [37]. To confirm low-intensity or ambiguous transitions, certain parts of the decay scheme are focused on during the analysis by specific $\gamma\gamma$ matrices, which are preselected by γ-rays originating from a certain rotational band or decay sequence within the complex ^{62}Zn excitation scheme. For data set 2, a $\gamma\gamma$ matrix was created, which focuses on the high-lying entry states in ^{62}Zn by requiring at least 14 detected γ rays with at least an energy of 16.5 MeV total energy and less than 19 MeV particle energy [32]. For the γ-ray spectrum analysis, the code TV developed at the University of Cologne [38], was used in the current analysis.

3.3 Doppler Shifts and Doppler Broadening

When the recoiling nuclei emit γ-rays, the energies will be Doppler shifted. The shifted energy, $E_\gamma(\theta)$, is related to the unshifted energy, E_0, by the relation

$$E_\gamma(\theta) = E_0(1 + (\frac{v}{c})\cos\theta) \tag{3.1}$$

Here, v is the recoil velocity of the nucleus of interest, and θ is the angle at which the γ ray is emitted to first approximation, i.e. the detector position relative to the beam direction. The shift is largest for the most forward and backward angles, while there is no shift at $\theta = 90°$. The recoil velocity of the nucleus, v, in the laboratory frame is typically a few percent of the velocity of light, c.
The finite opening of the γ-ray detector leads to a Doppler broadening. If the opening angle of the detector is $\Delta\theta$, then the partial derivative of Eq. 3.1 gives

$$\Delta E_\gamma = E_0(v/c)\sin\theta\Delta\theta \tag{3.2}$$

The Doppler broadening is maximum for θ = 90°. The Doppler broadening can be minimized by using segmented Ge detectors, where the effective solid angle $\Delta\theta$, is reduced at the front face of the detector.

Another considerable contribution to the Doppler shift arises from the velocity variation of the recoiling nuclei due to energy-loss straggling of the projectiles in the target, as well as the emission of evaporated particles (see Sec. 3.4). It means that the recoiling nuclei have velocity vectors different from the beam axis. Since the corresponding Doppler shift depends on the detector angle as $\cos\theta$, this is most important for detector angles close to 0° and 180°.

The feeding of low-spin yrast nuclear states is generally slow ($\approx 10^{-10}$s), and their decays take place outside the target where a proper velocity distribution is defined for the recoiling nuclei. In this case the Doppler shift can be corrected by using the average velocity or more refined methods (see Sec. 3.4.). On the other hand the superdeformed states or highest spin states may decay while still in the target material due to their feeding times and very short lifetimes. This causes larger and variable Doppler shifts which requires additional Doppler corrections compared with the γ-rays emitted by low-spin yrast states.

3.4 Kinematic Corrections for Doppler Effects

The velocities and directions of the evaporated charged particles from the compound nucleus change the velocity and direction of the recoil nucleus. This may result in worsened energy resolution of the γ-ray detected mainly

in the thin target experiments, in which the target material does not have any backing foils to stop the recoils. This problem is more prononuced for neutron-deficient nuclei which are formed by emission of α-particles.

This problem has been tackled by measuring charged particle energies and angles with the Microball detector array, and thereby defining the momenta of the recoiling residual nuclei for each event. Thus the change in direction and velocity of the recoil due to the charged particle emission can be calculated, and used to improve the γ-ray energy resolution. More details are given in for example, [6, 35, 39].

In addition, the γ-rays originating from the SD bands and highly deformed rotational bands are likely to be emitted while the residual ^{62}Zn nuclei are still slowing down inside the thin target foil. Assuming an average deformation of the rotational bands in ^{62}Zn and simulating the slowing-down process in the thin target layer, so called additional fractional Doppler shifts can be derived as a function of γ-ray energy [40]. Taking this into account, a more accurate Doppler-shift correction of the γ-rays originating from highly deformed structures can be obtained.

3.5 Channel Selection Methods

Because of the existence of several exit channels with significant population cross sections of residual nuclei in the mass $A \sim 60$ region, one should use specific channel selection methods in order to eliminate the competing reaction channels and to improve the total peak-to-background ratio of the γ-ray spectra belonging to the specific isotope of interest. The most basic employed channel selection method is the gating on the number of evaporated particles in the specific reaction channels. More details on this method are already discussed in Sec. 2.4.

The charged-particle gating method is not good enough to use, where the higher particle multiplicity channels with larger cross-sections dominate over the low particle multiplicity channel with less population cross section. In order to overcome these difficulties in a study of weakly populated channels, a method called Total Energy Gating (TE- Gating) was introduced in [36]. This method is based on the γ-ray multiplicity and sum-energy measurements [35].

The main concept of the TE-gating method is that the total energy of the γ rays and emitted particles should essentially be constant for all events, as the compound nucleus always obtains approximately the same excitation energy. The total energy for a given reaction channel, E^*, is given by $E^* = H_\gamma + T_{part}$, where H_γ is the total γ-ray energy and T_{part} is the total kinetic energy of the emitted particles. Because E^* is approximately constant for a given reaction channel, a plot of the total particle kinetic energy

vs the total γ-ray energy gives information about the events corresponding to this channel. In this plot a non-identified particle will lead to a too low value of parameter T_{part}. The TE-gating can hence discard such an event.

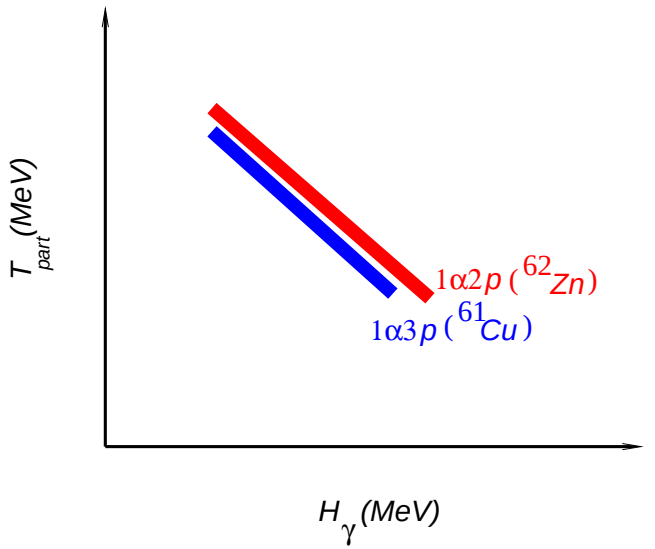

Figure 3.2: Schematic Total Energy Plane (TEP) for events in coincidence with one α and two protons detected in Microball. Here the red line indicates the events corresponding to the $1\alpha 2p$ channel (where ^{62}Zn is populated), while the blue line shows events in the $1\alpha 3p$ channel (where ^{61}Cu is populated) and one proton escaped detection.

Figure 3.2 shows a schematic Total Energy Plane (TEP). Only events with one α- particle and two protons detected in Microball are considered. The events corresponding to $1\alpha 2p$ channel ^{62}Zn are lying on the red line, whereas the events belong to the $1\alpha 3p$ channel ^{61}Cu are expected on the blue line. Now, consider a $1\alpha 3p$ event that appears in the $1\alpha 2p$-gated data because one of the protons was missed. First, as seen from the position of the two lines, the total energy for the $1\alpha 3p$ channel is smaller than that for the $1\alpha 2p$ channel by the binding energy of the third proton. Secondly, the kinetic energy of the missed proton is absent from the T_{part}. Therefore, if only events along the red line in Fig. 3.2 corresponding to ^{62}Zn are accepted, the contamination from ^{61}Cu can essentially be eliminated.

3.6 DCO Ratios

Assignments of spin and parity of the excited levels were based on the analysis of 1α2p- gated directional $\gamma\gamma$ correlations of oriented states (DCO ratios). The Ge-detectors of Gammasphere were grouped into three "pseudo" rings called "30", "53", and "83", which correspond to an average angle for the respective sets of detectors while accounting for γ-ray emission symmetry with respect to the $90°$- plane perpendicular to the beam. Three combinations of angles were chosen and sorted into matrices, namely (30 - 83), (30 - 53), and (53 - 83); for instance, for the (30 - 53) matrix, γ rays detected at $30°$ were sorted on one axis and those detected at $53°$ placed on the other axis of the correlation matrix.

The DCO ratios for almost all experimentally observed γ-rays in ^{62}Zn could be determined with the (30- 83) $E_\gamma - E_\gamma$ matrix. In this matrix, the experimental DCO ratios were extracted [41] according to the formula

$$R_{DCO} = \frac{Y(\gamma_1 \text{ at } 30°;\ \text{gated with } \gamma_2 \text{ at } 83°)}{Y(\gamma_1 \text{ at } 83°;\ \text{gated with } \gamma_2 \text{ at } 30°)}.$$

The intensities Y were extracted from a 1α2p- and TE-gated γ-γ matrix with γ-rays detected at 30° sorted on one axis and 83° on the other axis of the matrix. The list of DCO ratios for the γ-ray transitions observed in ^{62}Zn is given in paper III, Table 1 [17]. The DCO ratios of some of the γ-rays could not be measured, mainly because of their low intensities. The DCO ratios for the (30- 53) and (53- 83) matrices are defined accordingly.

Typical values for R_{DCO}, when gating on a stretched $E2$ transition, are

$$R_{DCO} = 1.0 \text{ for } E2 \text{ transitions;}$$
$$R_{DCO} \sim 0.9 \text{ for } \Delta I = 0 \text{ transitions;}$$
$$R_{DCO} \sim 0.6 \text{ for stretched } \Delta I = 1 \text{ transitions.}$$

However, ΔI = 1 transitions can show deviations from the expected value due to quadrupole admixtures, i.e., nonzero $\delta(E2/M1)$ mixing ratios. $M2$ and higher order than quadrupole transitions are neglected due to their low transition probabilities.

An analysis of the mixing ratios, $\delta(E2/M1)$, was performed for several $\Delta I = 1$ transitions based on DCO-ratios arising from the three different angle combinations. The phase convention of Rose and Brink [42] is used for the mixing ratios. The alignment coefficients, α_2 were estimated through the relation [43].

$$\alpha_2 = 0.55 + 0.02 \cdot E_x \text{ [MeV]}, \Delta\alpha_2 = \pm 0.05 \tag{3.3}$$

Figure 3.3 shows two spectra in coincidence with the gating transition at 1586 keV, corresponding to the $16^+ \rightarrow 14^+$ ($E2$ transition) of structure ND6b (see Fig. 4.2 The spectrum in panel (a) is obtained by gating on the y-axis (83°) and projecting the coincident events onto the x-axis (30°). The spectrum in panel (b) is produced in the opposite way. The transitions at, for example, 954, 1232, 1340, 1522 and 1791 keV have stretched $\Delta I = 2$ character, which can already be seen by observing that these transitions have basically same intensity in the spectra of both panel (a) and (b) ($R_{DCO} \approx 1.0$). The R_{DCO} value of a γ-ray transition is obtained by determining the yield of the peaks present in each spectrum, dividing their intensities and then correcting the result with the γ-ray efficiency. The peaks at 557 and 1161 keV, which are marked in blue, have known pure electric dipole character. For these peaks the intensities are higher in panel (b) than in panel (a). The peak at 1821 keV corresponds to a mixed $E2/M1$ character, R_{DCO}(1821) = 0.35(3).

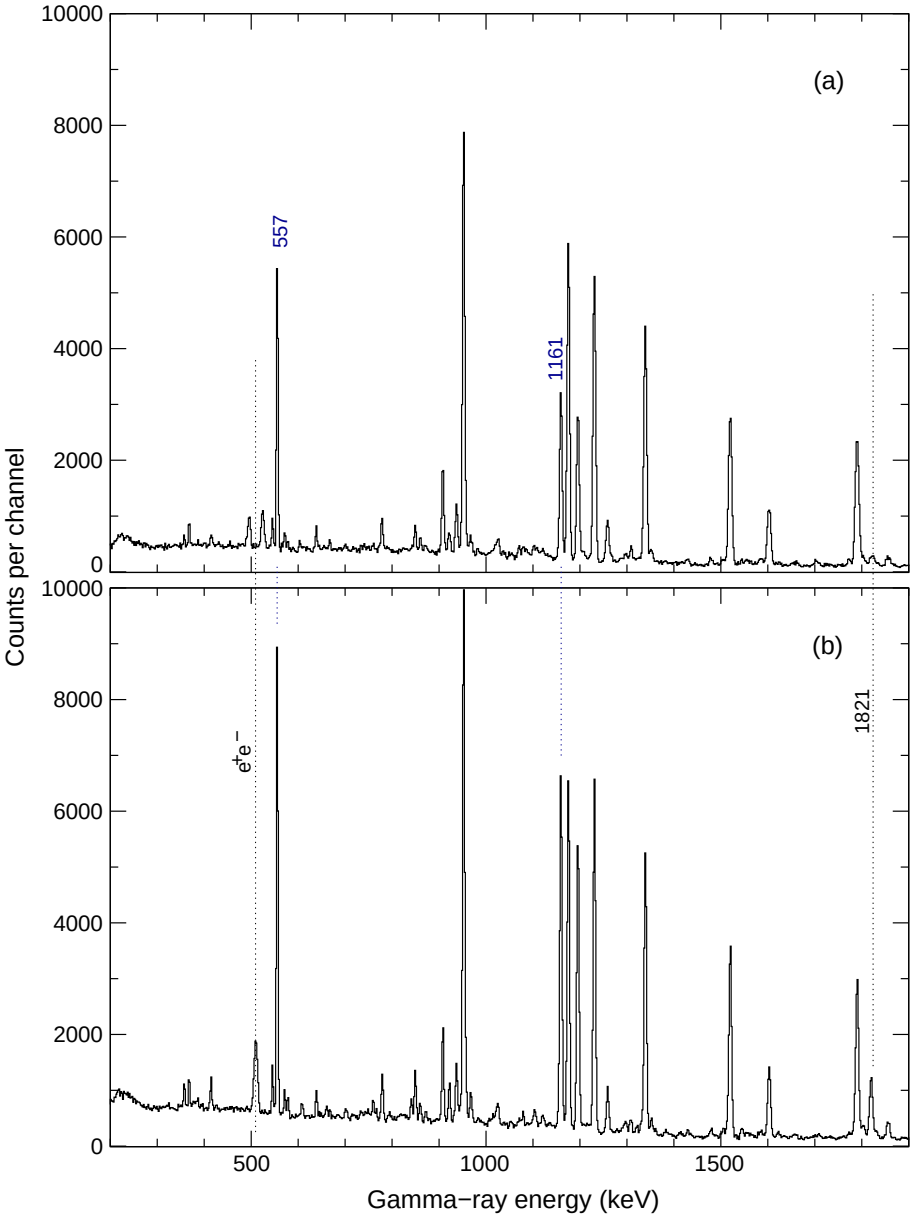

Figure 3.3: γ-ray spectra in coincidence with the $16^+ \rightarrow 14^+$ yrast transition at 1586 keV. (a) Gating on the y-axis (83°) and projecting the events onto the x-axis (30°). (b) Gating on the x-axis (30°) and projecting the events onto the y-axis (83°). See text for details.

Chapter 4

Results on ^{62}Zn

Previously, high spin states in ^{62}Zn have been reported in Refs. [8, 19, 44, 45, 46, 47]. The present level scheme of ^{62}Zn was established by using the combined statistics of four different experiments. It is shown in Fig. 4.1. It was constructed on the basis of coincidence relations, intensity balance and summed energy relations. Due to the complexity of the level scheme of ^{62}Zn, each structure or rotational band labelled in Fig. 4.1 is going to be presented separately (cf. paper III). The low-spin normal deformed part is shown in Fig. 4.2, with the labels ND1-ND9. The two previously known terminating bands are labelled as TB1 and TB2 [19]. The ' well-deformed ' bands are labelled WD1-WD11. The superdeformed bands are labelled SD1-SD5. In addition, the signature partner structures are noted with extra labels, 'a' for $\alpha = 1$ signature band and 'b' for $\alpha = 0$ signature band. The spin and parity assignments of the γ-ray transitions are obtained from the analysis of the DCO ratios. The DCO ratios of some of the γ-rays could not be measured, mainly because of their low intensities. The level energies, the corresponding depopulating γ-rays, their relative intensities, their angular correlation ratios, and resulting spin-parity assignments are given in [17]. The ground-state transition is normalised to 10,000 units of intensity.

The spins and parities of the few normal deformed structures and for TB1 and TB2 were already known from earlier studies [8, 19]. The DCO ratios of the transitions from these levels obtained in this experiment are in agreement with these assignments. The observed highest spin deduced from these results for states with known spin values is 24^- at $E_x = 23179$ keV [8, 19]. Our studies [17, 48] revealed more information about five superdeformed bands, SD1-SD5, eleven well-deformed bands, WD1-WD11, and low-spin normally deformed (ND) part of the level scheme. The observed highest spin from this study is 35^- at $E_x = 42.5$ MeV [48].

In the following, the different sections of the extensive new decay scheme are introduced and discussed by means of a few selected γ-ray spectra and R_{DCO}-values. The normally deformed region is described in Sec. 4.1. This region reaches up to the 15705 keV $I^{\pi} = 19^{-}$ energy level and comprises the states not included in any of the more collective structures. The two previously known terminating structures are described in Sec. 4.2 and the well-deformed and superdeformed structures are briefly described in Sec. 4.3. Furthermore, the high quality of data set 1, is demonstrated in Sec. 4.3. The intensities of most of the γ transitions were deduced from the $\gamma\gamma$ matrices. All excited rotational bands were connected to the low-spin normal deformed states via one or more linking transitions. In most cases, this allowed for firm, but sometimes only tentative spin and parity assignments to the lowest states in the bands. The tentative spin and parity assignments to the states near the top of the bands are based on their regular rotational behaviour.

4.1 The Low-spin Normally Deformed Region

Figure 4.2 shows the low-spin normal deformed part of the present decay scheme, which adds the five new structures ND4, ND5, ND7, ND8 and ND9 in addition to the previously known structures ND1, ND2, ND3 and ND6 [19]. All the near yrast energy level assignments made in the previous works are in agreement with the present results.

4.1.1 Structures ND1 and ND2

The previously known structures were extended from the level energies at 3708 keV to 5911 keV (ND1), 5144 keV to 6965 keV (ND2a) and 4348 keV to 6445 keV (ND2b) by adding the 2203, 1821 and 2097 keV γ-ray transitions on top of the structures ND1, ND2a and ND2b, respectively. For the structure ND1, the 0^{+}, 2^{+}, 4^{+} and 6^{+} states were observed previously. The previously placed topmost two transitions, at 1774 keV ($8^{+} \rightarrow 6^{+}$) and 2018 keV ($10^{+} \rightarrow 8^{+}$), were now rearranged as side feeding transitions. The newly added transition at 2203 keV has an $E2$ behaviour. The ND1 structure is fed by strong transitions, at 557, 641 and 851 keV from the ND2b structure. The DCO values for these γ-rays are consistent with ΔI=0 character. Here, the 557 keV transition is a doublet with the same energy as the $E1$ transition which depopulates the level at 4905 keV. Interestingly, these two transitions are also in coincidence with each other. However, by putting gates on different $E2$ transitions, it is possible to distinguish their multipolarities (see paper III Table 1 [17]).

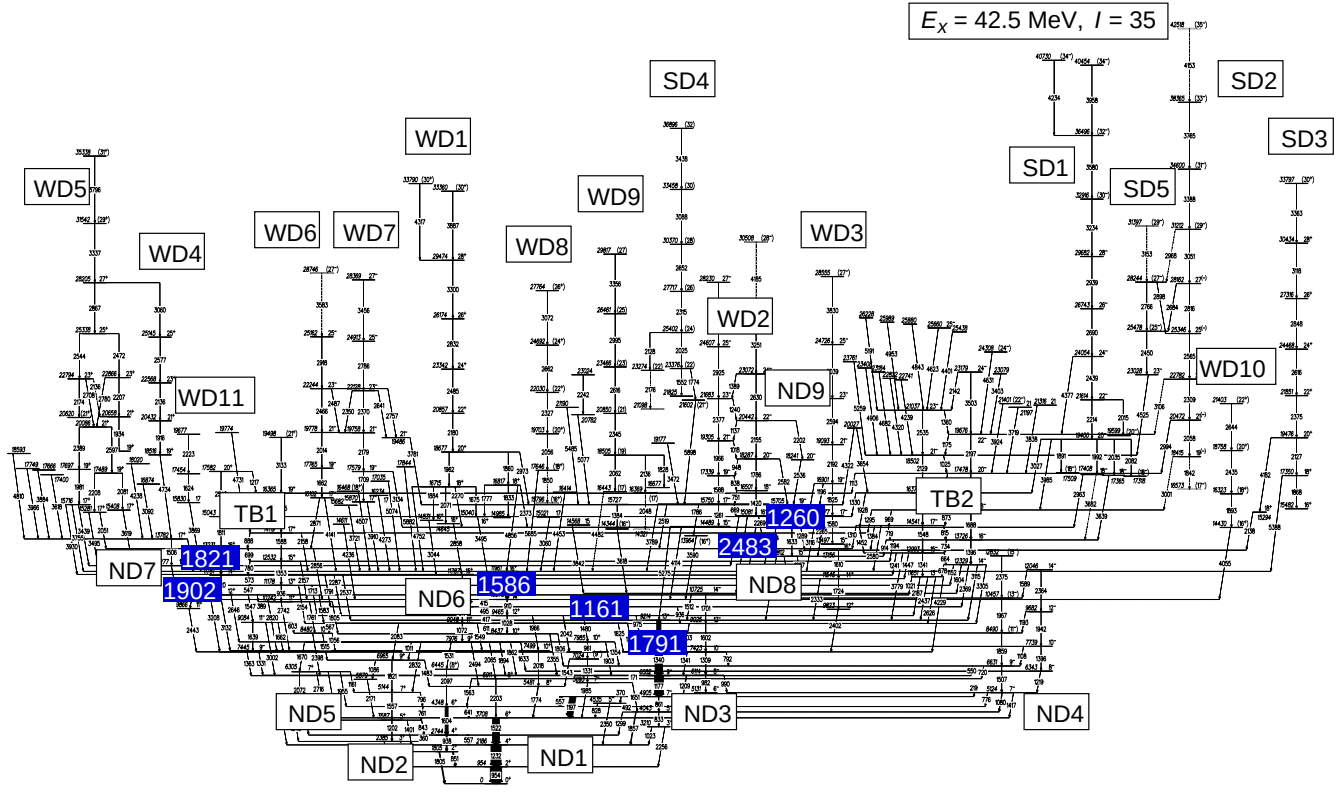

Figure 4.1: Proposed high-spin level scheme of ^{62}Zn. Energy labels are in keV and the intensities of the transitions are here indicated by the relative thicknesses of the arrows. Tentative levels and transitions are dashed. The transitions marked in blue are significant for the linking of well-deformed and superdeformed bands. See Ref. [17] for a detailed version of the complete excitation scheme of ^{62}Zn.

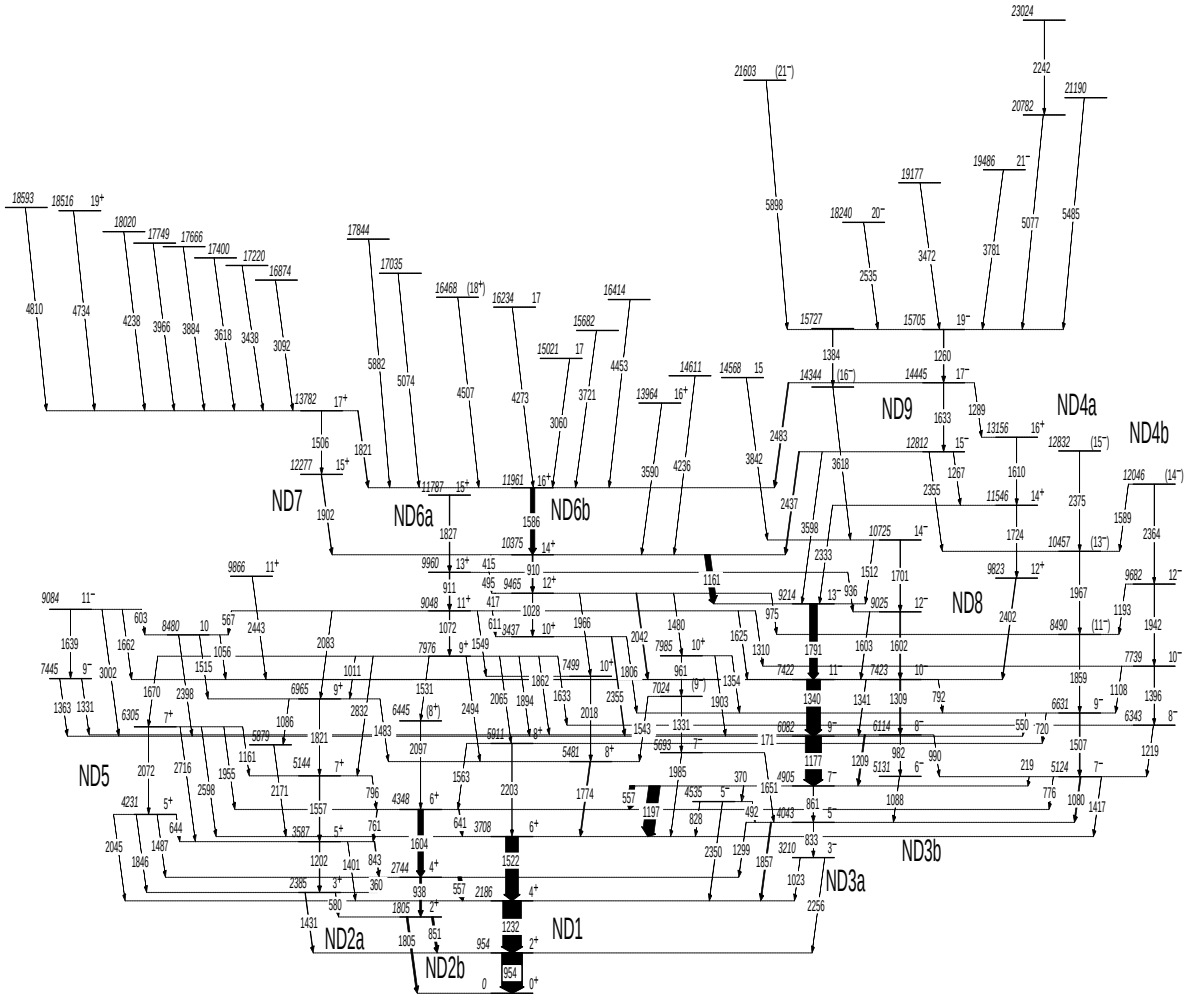

Figure 4.2: Normally deformed region of the proposed level scheme of ^{62}Zn. Energy labels are in keV. See text for details.

The structure ND2 consists of two signature partner bands, ND2a ($\alpha = 1$) and ND2b ($\alpha = 0$). These are connected to each other via $E2/M1$ transitions at 360, 761, 796 and 843 keV. ND2a and ND2b both feed into the ND1 structure through highly intense γ-ray transitions at 851, 1805 keV (ND2b) and 1431 keV (ND2a) accordingly. The spin and parity assignment for the lowest state of the ND2a structure was determined by the rather intense transition at 1431 keV with a R_{DCO} value indicating an $E2/M1$ character. This assignment is further supported by the 580 keV transition, which is also of $E2/M1$ character. The spin and parity assignment of the lowest state of the ND2b structure was defined by the R_{DCO} values of the 851 and 1805 keV transitions, R_{DCO}(851)= 0.93(6) with ΔI = 0 behavior, and R_{DCO}(1805)= 1.12(9) with $E2$ behavior, respectively. The large uncertainties in the R_{DCO} value for the 2097 keV γ-ray transition, which depopulates the state at 6445 keV, makes the state spin and parity assignments tentative (8^+). The multipolarity assignments of all known states in ND1, ND2a, and ND2b have been verified.

4.1.2 Structure ND3

The earlier known structure ND3a ($\alpha = 1$) and the new structure ND3b ($\alpha = 0$) are considered signature partners. They are connected via relatively intense 1088, 1209, 1341, 1512 and 1603 keV γ-ray transitions. The DCO ratios for all these transitions are consistent with mixed $E2/M1$ character, which indicates that these structures must have the same parity. The maximum spin is $I = 13^-$ at E_x = 9214 keV for structure ND3a and $I = 14^-$ at E_x = 10725 keV for structure ND3b. Structure ND3a has seven connecting transitions to the low spin levels. Four of these, at 1023 ($3^- \rightarrow 4^+$) , 1197 ($7^- \rightarrow 6^+$) , 1857 ($5^- \rightarrow 4^+$) and 2256 ($3^- \rightarrow 2^+$) keV, decay into structure ND1, and the transitions at 557 ($7^- \rightarrow 6^+$) and 1299 ($5^- \rightarrow 4^+$) keV instead decay into ND2b.

The 370 keV γ-ray depopulates the 7^- state at E_x = 4905 keV, and decays into the 5^- state at E_x = 4535 keV. The R_{DCO} value of the 370 keV γ-ray, R_{DCO}(370) = 0.92(7), indicates an $E2$ character. This defines the spin and parity assignment, $I = 5^-$, for the state at 4535 keV. Among all these transitions, the intense 557 and 1197 keV transitions carry out ~ 90 % of the intensity from structure ND3a.

As already mentioned, the 557 keV $E1$ transition which depopulates the state at 4905 keV, is a doublet with the same energy as the mixed $\Delta I = 0$ transition, depopulating the level at 2744 keV. The lowest states of ND3a and ND3b were determined by the R_{DCO} values of the 1023 and 1088 keV γ-rays, respectively. The two weak transitions, at 792 and 990 keV, from ND3b are connecting to the other part of the low-spin region. The in-band

transitions of ND3a and ND3b are consistent with $E2$ character. They define the spin and parity assignments within the structure.

The two doublet transitions, at 1602 keV and 1603 keV, and 1340 keV and 1341 keV were placed in parallel according to $\gamma\gamma\gamma$ coincidences and R_{DCO} values. The measured DCO ratios for the 1602 and 1340 keV transitions indicate their quadrupole nature. Due to the doublet structure of these transitions with almost the same energies, it is then difficult to confirm the multipolarites of 1603 and 1341 keV transitions with their R_{DCO} values, which suggest as $E2$ transitions. However, these two transitions are connecting between the same parity bands and thus confirmed them as mixed $E2/M1$ character.

A γ-ray spectrum in coincidence with the gated transition at 1209 keV, which depopulates the 8^- state at E_x = 6114 keV, is presented in Fig. 4.3, panel (a). The strong coincidences at 954, 1232 and 1522 from ND1 and the transition at 938 from ND2b, 861 keV from ND3a and the in-band transitions at 1309, 1602 and 1701 keV of ND3b are clearly visible. The weak transition at 2350 keV, from the 5^- state at 4535 keV to the yrast 4^+ state at 2186 keV is also seen. From the 11^+ state at 9048 keV of ND6a, there is a transition of 1625 keV connecting to ND3b. The in-band transitions at 911 and 1827 keV of ND6a, including the 1625 keV transition are also labelled in the spectrum. The intense decay-out transitions at 851 and 1805 keV from ND2b and decay-out transition at 1857 keV from ND3a are also marked. Many other low intensity coincidences are also visible in the figure. The inset shows the high-energy portion of this spectrum including the low-intensity 4355 and 4734 keV transitions, which are the main linking transitions to two high-spin band structures (WD2b and WD4).

4.1.3 Structure ND4

The ND4 structure comprises two new structures, which are signature partners labelled as ND4a ($\alpha = 1$) and ND4b ($\alpha = 0$). ND4a ranges from the 5124 keV 7^- state to the 12832 keV (15^-) state, whereas ND4b corresponds to a set of states from 8^- at 6343 keV to 14^- at 12046 keV. The $I^\pi = 7^-$ assignment to the band head of structure ND4a at 5124 keV was fixed by the stretched $E2$ character of the 1080 keV transition connecting to the 5^- state at E_x = 4043 keV. The spin and parity assignment to the 9^- state at E_x = 6631 keV is based on the $E2$ character of the 1507 keV transition, with an R_{DCO} (1507) = 1.05(6). The assignments of the (11^-), (13^-) and (15^-) states at 8490, 10457 and 12832 keV, respectively, are based on the apparent regular increase of their excitation energies.

The two lowest states at 6343 and 7739 keV of ND4b decay into the

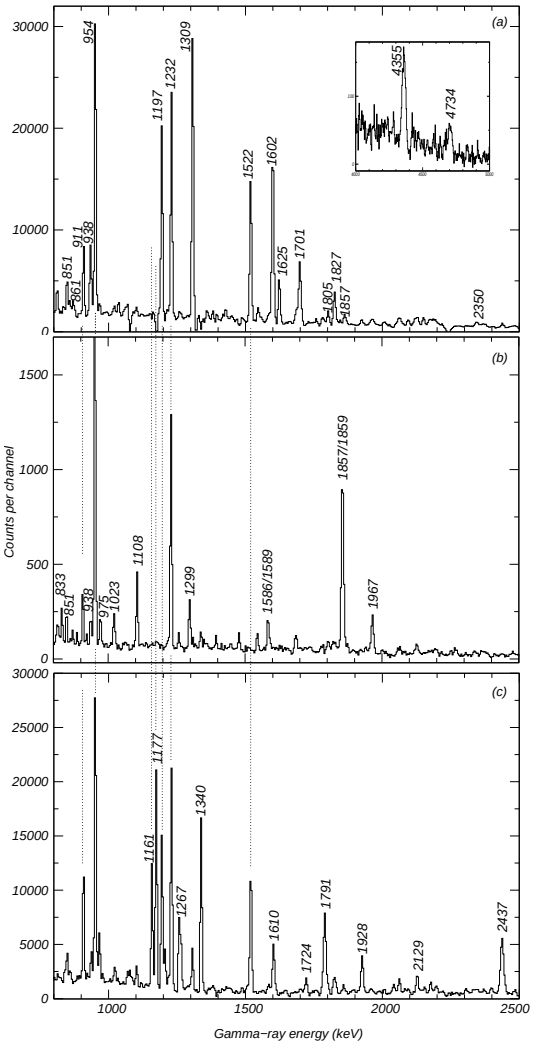

Figure 4.3: Spectra taken in coincidence with (a) the 1209 keV γ-ray transition, (b) both the 1080 and 1507 keV γ-ray transitions, and (c) both the 1260 and 1633 keV γ-ray transitions. See text for details.

states at 5124 and 6631 keV of ND4a via intense $E2/M1$ transitions at 1108 and 1219 keV, respectively. The other two states at 9683 and 12046 keV of ND4b decay into states at 8490 and 10457 keV of ND4a via weak $E2/M1$ transitions at 1193 and 1589 keV. The lowest level at 6343 keV in ND4b is established as $I^{\pi} = 8^{-}$ state based on the mixed $E2/M1$ nature of the 1219 keV line.
The in-band structure transitions at 1396 and 1942 keV have $E2$ character. The topmost state, I^{π} = 14^{-} at 12046 keV, is added based on regular rotational character.

Figure 4.3 panel (b) shows the γ-ray spectrum in coincidence with transitions at 1080 or 1507 keV. The in-band transitions at 1859 and 1967 keV of ND4a and the intense connecting transition at 1108 keV between ND4a and ND4b, are clearly seen. The relevant peaks belonging to normal deformed structures are identified with dashed lines. The normal deformed region transitions at 833, 851, 938, 975, 1023, 1299 and 1586 keV from the other part of the level scheme are also visible.

4.1.4 Structure ND5

Structure ND5 is an irregular structure with a lot of positive-parity states in the range $E_x \sim 4 - 9$ MeV. Except for the transition at 1774 keV ($8^{+} \rightarrow 6^{+}$), the intensities of all such γ-rays are on the level of a percent or less. The 9^{+} state at 7976 keV of ND6a decays to the level at 6305 keV by a 1670 keV γ-ray transition. R_{DCO} (1670)= 1.32(22) is consistent with an $E2$ character, and defines the state at 6305 keV to be 7^{+}. The state at 6305 keV decays to both a 5^{+} state (through E_{γ} = 2072 keV) and a state with 5^{+} (via E_{γ} = 2716), and the 2716 keV line has a DCO ratio, which indicates an $E2$ transition. The quadrupole nature of the 1639 keV ($11^{-} \rightarrow 9^{-}$) γ-ray transition defines the states 11^{-} at 9084 keV and 9^{-} at 7445 keV.

Here, the 4231 keV, $I^{\pi} = 5^{+}$ state is a good example for a definite assignment of spin and parity despite the lack of angular correlation data of both feeding or depopulating transitions. The decay chain from the state 9^{+} at 7976 keV of ND6a to the state 3^{+} at 2385 keV of ND2a is as follows: $9^{+} \rightarrow 7^{+} \rightarrow$ 4231 keV state $\rightarrow 3^{+}$. The states 9^{+} at 7976 keV of ND6a, 7^{+} at 6305 keV and 3^{+} at 2385 keV of ND2a are fixed. The possible spin and parity options for state at 4231 keV are 6^{+}, 5^{+}, 5^{-} and 4^{+}. Assignments of 6^{+}, 5^{-} and 4^{+} are ruled out based on the less transition probabilities of $M2$ or higher order multipolarities. Consequently the spin and parity assignment of the state at 4231 keV is fixed to be 5^{+}.

4.1.5 Structure ND6

Structures ND6a ($\alpha = 1$) and ND6b ($\alpha = 0$) are two earlier known signature partner structures with $E2$ transitions inside each structure, connected via $E2/M1$ transitions at 415, 417, 495 and 611 keV. The ND6 structure is decaying into ND1, ND2, ND3 and ND5.

The structure ND6a is formed by a set of states from the 7976 keV 9^+ state to the 11787 keV 15^+ state. It has a sequence of $E2$ transitions at 1072, 911 and 1827 keV. The previously placed transition at 1268 keV, on the top of the 9048 keV level, is now replaced with the 911 keV transition. The doublet transitions at 910 and 911 keV of ND6a and ND6b were placed next to each other according to their respective coincidences. Several γ-ray transitions, namely at 567, 936, 1011, 1531, 1549, 1625, 1633, 1862, 1894, 2065, 2083, 2494 and 2832 keV connect the ND6a structure to the low-spin normal deformed region. The R_{DCO} value of the intense transition at 2832 keV ($9^+ \rightarrow 7^+$) indicates that it is an $E2$ transition. Hence, the 7976 keV level has a spin and parity of 9^+. The spin and parity assignment of the 11^+ state at 9048 keV was defined by the R_{DCO} value of the 1625 keV γ-ray transition. The R_{DCO} value of this transition, R_{DCO} (1625) = 0.59(4) is consistent with $E1$ character.

The structure ND6b corresponds to a set of states from the 8437 keV 10^+ state to the 11961 keV 16^+ state. The band members are the 1028, 910, and 1586 keV transitions, which are consistent with $E2$ nature. There are several decay-out transitions from the structure ND6b, like 975, 1161, 1480, 1806, 2042, and 2355 keV. Among all these, the transitions at 1161, 2043 and 2355 keV are intense enough to define the band's spin and parity assignment. The DCO ratios, R_{DCO}(1161) [$14^+ \rightarrow 13^-$] = 0.54(3), R_{DCO}(2042) [$12^+ \rightarrow 11^-$] = 0.51(5) and R_{DCO}(2355) [$10^+ \rightarrow 9^-$] = 0.67(5) are consistent with pure $E1$ character. The structure ND6b decays to the 13^- state of ND3a via the 1586-1161- keV, $E2 - E1$ cascade. These two γ rays mark the end of transitions with relative intensities in excess of 10%. Thus, the 1586 keV transition is very important to find out the DCO-ratios of many of the weak connections, which are towards the rotational bands.

States without any Structures

There are several states which do not seem to belong to any apparent band-like structures, namely at 13964, 14611, 15021, 15682, 16234, 16414, 16468, 17035, and 17844 keV. The corresponding weak intensity γ-ray transitions from these states, for example, at 3060, 3721, 4273, 4453, 4507, 5074 and 5882 keV are decaying into the state 16^+ at E_x = 11961 keV. The two transitions at 3590 and 4236 keV instead decay into the state 14^+ at E_x = 10375

keV of ND6b. It is possible to determine DCO ratios for some of these weak transitions. For instance, a R_{DCO} value of the 4507 keV transition, R_{DCO} (4507) = 0.86(18), which in combination with yrast arguments tentatively suggests the state at 16468 keV to have $I^{\pi} = (18^{+})$. The same procedure has been used to assign a spin of I= 17 to the states at 15021 and 16234 keV, while the parity of the levels remains undetermined. The spin and parity assignment of the state 16^{+} at E_x = 13964 keV is confirmed by the DCO ratio of the decay-out transition at 3590 keV, which is consistent with an $E2$ character. The multipolarity assignments of the other states could not be established due to low intensity decay-out transitions.

Figure 4.4 (a) illustrates the high-energy part of the γ-ray coincidences

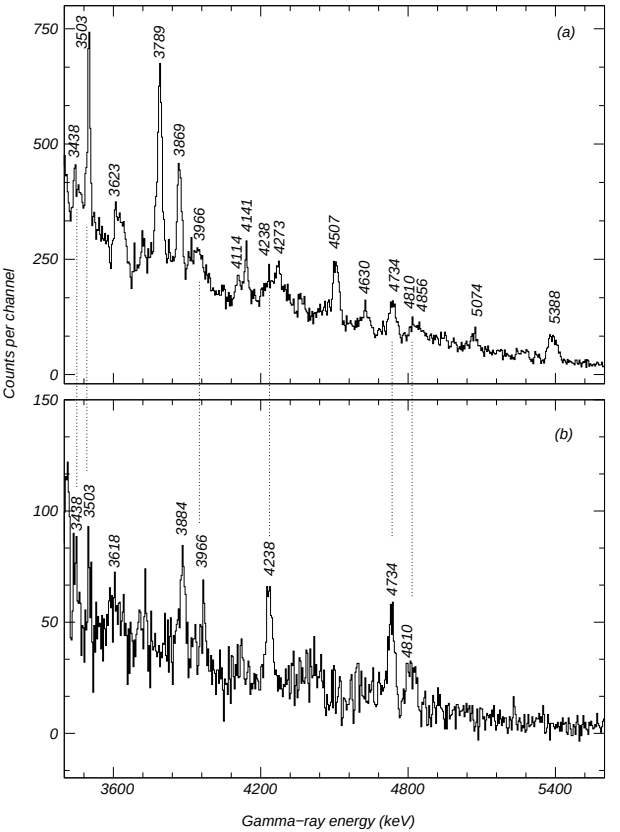

Figure 4.4: (a) High-energy part of the γ-ray spectrum in coincidence with the gating transition at 1586 keV. (b) High-energy part of the γ-ray spectrum in coincidence with the gating transition at 1821 keV.

with the 1586 keV transition in ND6b. The transitions depopulating several high-spin band structures decay into the state 16^+ (not shown in Fig. 4.2 but see Fig. 4.1) at 11961 keV, like at 3789 (WD2a), 3869 (WD10), 4141 (WD5), 4734 (WD4), 4856 (WD1), or 5388 (SD3) keV are clearly visible. Even though the decay-out γ-transition at 4114 (WD2a) keV does not feed into the 11961 keV level, it is clearly seen in the spectrum, due to the contamination from an in-band transition at 1588 keV in WD2a. The in-band transitions at 3503 keV from TB2 and 3623 keV from WD2a are also seen in the spectrum. A large number of weak high-energy γ rays at 4273, 4507, 5074, 4238 and 4810 keV, depopulating the corresponding states at 16234, 16468, 17035, 18020 and 18593 keV, are feeding into the 16^+ state at 11961 keV, are also identified.

4.1.6 Structure ND7

The new structure ND7 is built with two states, 15^+ and 17^+ at 12277 keV and 13782 keV, respectively. The one and only in-band transition at 1506 and the two other transitions at 1821 and 1902 keV lead to the yrast 17^+ state at 13782 keV. The DCO-ratios of both the 1821 and 1902 keV lines clearly point at mixed $E2/M1$ character, while the number available for the 1506 keV transition is consistent with a stretched $E2$ assignment. Interestingly, the mixing ratios $\delta(E2/M1)$ for the 1821 and 1902 keV transitions are nearly same; either moderate ($\delta \approx 0.3$) or significant ($\delta \approx 2.0$) quadrupole mixture is observed. Similar to the 11961 keV, 16^+ state, the 13782 keV level is also fed by several 3-5 MeV high-energy γ-ray transitions. Among all these transitions, there is only one transition at 4734 keV, which depopulates the state at 18516 keV, associated with $E2$ character. The spin and parity assignments of that state were defined to be 19^+. The multipolarities of the remaining states could not be established due to weak intensity decay-out transitions at 3092, 3438, 3618, 3884, 3996, 4238, and 4810 keV. Figure 4.4 (b) shows the high-energy part of the γ-ray spectrum in coincidence with the 1821 keV γ-ray, which depopulates the state at 13782 keV. The highly energetic γ-ray transitions at 3438, 3503, 3618, 3884, 3966, 4238, 4734 and 4810 keV are clearly visible. All marked γ-ray transitions in Fig. 4.4 (b) are also seen in Fig. 4.4 (a) and are identified with dashed lines.

4.1.7 Structures ND8 and ND9

The ND8 structure is built up by a set of states from 12^+ at E_x = 9823 keV to the state 16^+ at E_x = 13156 keV. The one and only strong decay out transition is at 2402 keV (12^+ at 9823 keV $\rightarrow$ 11^- at 7422 keV) resolves the spin and parity of 9823 keV level. The R_{DCO} (2402) = 0.63(6) indicates its dipole

character. The parity of ND8 is confirmed by the decay of the fixed state 20^+ at 19476 keV [48] into the state 16^+ at 13156 keV of ND8 via the 4128-2138-keV, $E2$ cascade (see Fig. 4.1). The R_{DCO} value of 2402 keV, which in combination with the $E2$ 1724 keV in-band transition of ND8, define the spin and parity assignment of the 9823 state to be I^{π}= 12^+. The 11546 keV state decays into the 9214 keV (ND3a) state via a 2333 keV γ-ray transition. The R_{DCO} value of 2333 keV transition is 0.53(9), is consistent with a dipole nature. Since the parity of the ND8 and ND3a is fixed, so the transition at 2333 keV is assigned to be electric dipole nature, which further define the level at 11546 keV to be 14^+. The in-band transitions at 1724 and 1610 keV have $E2$ character.

The structure ND9 consists of the 12812, 14445 and 15705 keV levels with two deexciting γ-ray transitions at 1633 ($17^- \rightarrow 15^-$) and 1260 ($19^- \rightarrow 17^-$) keV in cascade. These two in-band transitions are quadrupole in nature since their DCO ratios are close to unity. The fixed state 19^- at 16373 keV [19] decays into the level at 14445 keV of ND9 via an $E2$ 1928 keV transition (see Fig. 4.1), which fixes the ND9 structure with negative parity. The structure ND9 decays into the structure ND8 through the 1267 and 1289 keV γ-ray transitions. The spin and parity of the state at 12812 keV was confirmed by a rather intense decay-out transition at 2437 keV. The 2437 keV γ-ray has R_{DCO} = 0.68(4), which is consistent with dipole character. Since this transition proceeds from the negative parity level at 12812 keV and decays into the fixed positive parity state 14^+ at 10375 keV, which thus confirmed the 2437 keV transition as an $E1$ character. The level at 14445 keV decays by emission of three γ-rays at 1289, 1633 and 2483 keV. The DCO ratio measurement of the intense decay-out transition at 2483 keV retrieve spin and parity assignments for 14445 keV state. The R_{DCO} (2483) = 0.52(3) is consistent with an $E1$ character and indicates that the spin and parity of the state at 14445 keV to be 17^-.

Similar to the 11961 keV, 16^+ state, the 15705 keV level is fed by six high-energy γ-ray transitions at 2535, 3472, 3781, 5077, 5485 and 5898 keV. The DCO values of the 2535 and 3781 keV transitions confirm the spin and parity of the states at 18240 and 19486 keV to be 20^- and 21^-, respectively. The DCO-ratios of the other γ-ray transitions could not be measured due to their weak intensities. The decay out transition at 5898 keV, which depopulates the 21603 keV state, is also too weak to determine a DCO ratio. The state spin and parities are instead preliminarily assigned to tentative (21^-) using yrast arguments.

Figure 4.3 (c) illustrates coincidences with both transitions at 1260 and 1633 keV. The relevant transitions from the low-spin normal deformed part of the level scheme are identified with dashed lines. In addition to the in-band transitions of ND8 at 1610 and 1724 keV, the decay-out transitions at

1267 and 2437 keV from the 15^- state at 12812 keV are marked. To structure TB2 (see Sec. 4.2.2), there is the 1928 keV linking transition visible, and from the structure TB2 itself the 2129 keV transition is also shown. This indicates that the TB2 structure decays into ND9. Several low-intensity transitions are also visible in the spectrum.

4.1.8 Other States

The spin and parity assignment of 10^+ to the state at 7499 keV is determined by the 2018 keV transition. The 7499 keV state decays to the 8^+ state at 5481 keV through a 2018 keV transition. The R_{DCO} (2018) = 1.03(8) indicates that the transition is of $E2$ character. The spin and parity of the 7499 keV and 5481 keV levels is then 10^+ and 8^+, respectively. This assignment is further supported by the 1774 keV transition, which is also an $E2$ character.

In a similar way, spin and parity assignments for the 10^+ state at 7985 keV and 7^- state at 5693 keV were defined. The large uncertainty in the R_{DCO} value of the 1331 keV transition, depopulating the 7024 keV state, makes the state spin and parity assignments tentative (9^-).

The state at 13964 keV was fixed to 16^+ via the 3590 ($16^+ \rightarrow 14^+$) $E2$ decay out transition.

4.2 Known Terminating Bands TB1 and TB2

Deformed bands that are observed to high rotational frequency with decreasing moments of inertia are called smoothly terminating bands [49]. TB1 and TB2 are previously known smoothly terminating bands [19].

4.2.1 Structure TB1

Figure 4.5 shows the structure of TB1. It consists of two signature partners, TB1a ($\alpha = 1$) and TB1b ($\alpha = 0$), which are built from quadrupole transitions and connected via intense $E2/M1$ transitions between them. The previous publication [19] determined a tentative parity for TB1. Current results confirm the parity of TB1a and TB1b by several linking transitions, which are connected to the established low-spin region. For example, the level at 10631 keV of TB1b decays to the fixed state 10^+ via a 3132 keV transition. The DCO ratio of 3132 keV transition, R_{DCO} (3132) = 1.11(23) is consistent with an $E2$ character, and fixed the spin and parity assignments of the level at 10631 keV to be 12^+. The maximum spin is $I^\pi = (21^+)$ at E_x = 19498 keV for TB1a and $I^\pi = 20^+$ at E_x = 17582 keV for structure TB1b. In addition to the previously suggested transitions at 2742, 3002

and 3208 keV, now the band is connected to the rest of the level scheme with many more γ-ray transitions, for example, at 1312, 1547, 1583, 1662, 1713, 1761, 1791, 1805, 2129, 2154, 2157, 2158, 2287, 2537, 2646, 2820, 2856 and 3132 keV. Among all these decay-out transitions, several R_{DCO} values were determined and used to define spin and parity assignments of TB1a and TB1b.

For example, the spin and parity assignments of the lowest states, 11^+ at 10242 keV (TB1a) and 12^+ at 10631 keV (TB1b) were defined by DCO ratios of the 2742 and 1547 keV transitions, respectively. The R_{DCO} value of the former transition, R_{DCO} (2742)= 1.10(16) is suggests $E2$ character, it is also consistent with mixed $E2/M1$ character. This assignment is mainly

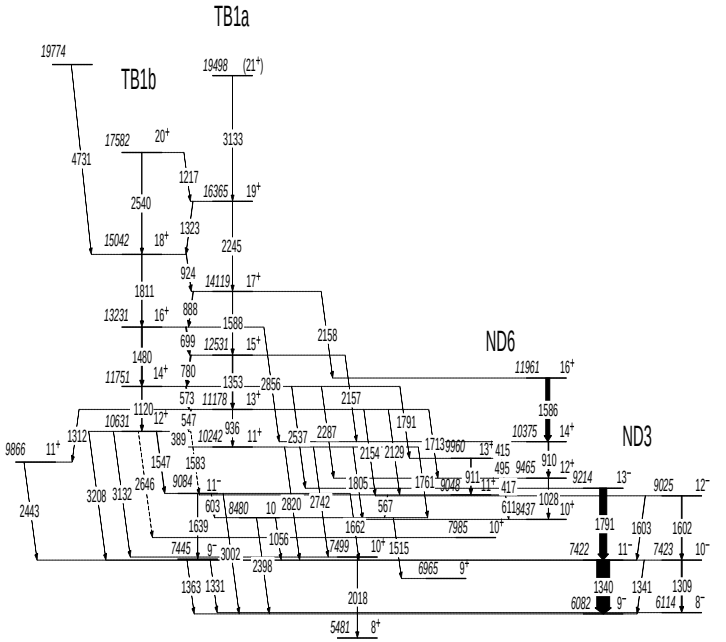

Figure 4.5: Structure of TB1 of the present level scheme. Energy labels are in keV and the intensities of the transitions are here indicated by the relative thicknesses of the arrows. Tentative levels and transitions are dashed.

based on the decay pattern: the 12^+ state at 10631 keV decays into the 11^+ state at 10242 via a mixed $E2/M1$ 389 keV transition, the 11^+ state further decays into the 10^+ state at 7499 keV via 2742 keV transition. Since the spin and parity assignments of 12^+ state at 10631 keV and 10^+ state at 7499 keV

are fixed, thus the 2742 keV transition is assigned to have $E2/M1$ character. The DCO ratio of 1547 keV transition, R_{DCO} (1547) = 0.59(5) is consistent with an $E1$ character.

There is one high-energy transition at 4731 keV decaying into the structure TB1. Since the intensity of this transition is low, it is difficult to measure a DCO ratio on it. The in-band transitions of TB1a and TB1b have $E2$ nature, and connecting transitions between them have $E2/M1$ character. All these R_{DCO} values are listed in paper III (Table 1).

Figure 4.6 (a) shows the γ-ray spectrum in coincidence with any combination of the 547, 573, 780, 699, 888 keV and the 547, 573, 780, 699, 888 and 924 keV $E2/M1$ transitions of structure TB1. In conjunction with the band members of TB1a and TB1b, all $E2/M1$ transitions in between them are also clearly seen. The intense decay out transitions at 1547, 1662, 2129, 3002, 3132 and 3208 keV are marked with star (*) symbols in black colour, while all transitions belonging to the normal deformed region are marked with star (*) symbols in blue color. The presence of a peak at 2018 keV arises from the decay pattern of the 12^+ state at 10631 keV. The 12^+ state at 10631 keV decays to the 10^+ state at 7499 keV via 3132 keV γ transition, and the 10^+ state at 7499 keV further decays to the state 8^+ at 5481 keV via 2018 keV γ transition.

4.2.2 Structure TB2

Figure 4.7 shows the structure of TB2. The previously published TB2 consists of two bands TB2a ($\alpha = 1$) and TB2b ($\alpha = 0$), which are signature partners. These two bands are built from $E2$ transitions and connected via strong $E2/M1$ transitions between them. In addition to the previously suggested transitions at 1931, 3115 and 4229 keV, now the band is connected to the rest of the level scheme with many more γ-ray transitions, namely at 914, 969, 1021, 1113, 1152, 1241, 1295, 1310, 1330, 1384, 1447, 1604, 2187, 2369, 2437, 2580, 2626, 3305 and 3779 keV. Among all these decay-out transitions, several R_{DCO} values were determined and used to define spin and parity assignments of TB2a and TB2b.

For example, the lowest states, 13^- at 11651 keV (TB2a) and 14^- at 12329 keV (TB2b), were defined by DCO ratios of 4229 and 3115 keV transitions, respectively. The R_{DCO}(4229 keV) = 1.30 (21) has an $E2$ nature and the R_{DCO}(3115 keV) = 0.93(10) has a mixed $E2/M1$ determine the corresponding levels spin and parity assignments. Even though the value of DCO-ratio for 3115 keV transition is close to the expectation for an $E2$ transition, the 3115 keV transition has been assigned an $E2/M1$ character. The fact is that the fixed 15^- state at 12993 keV decays into the 14^- state at 12329 keV via a mixed $E2/M1$ 664 keV transition, and further the 14^-

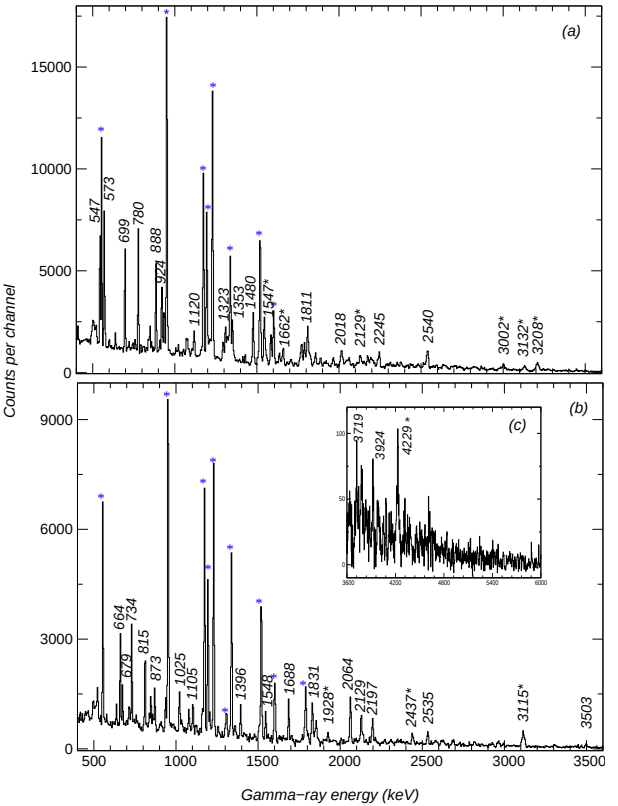

Figure 4.6: (a) Coincidence spectrum with any combination of the 547, 573, 780, 699, 888 keV and the 547, 573, 780, 699, 888 and 924 keV transitions of TB1. The strong decay out transitions at 1547, 1662, 2129, 3002, 3132 and 3208 keV are marked with star (*) symbols in black colour, while all relevant normal deformed region transitions are marked with star (*) symbols in blue color. (b) Coincidence spectrum with any combination of the 664, 678, 734, 815 keV and the 664, 678, 734, 815 and 873 keV transitions of TB2. The strong linking transitions at 1928, 2437 and 3115 keV are indicated with a star (*) in black color. The relevant transitions belong to the normal deformed region of the level scheme are marked with star (*) in blue color. (c) Same coincidence γ-ray spectrum as (b), but illustrates for the high-energy γ-ray transitions ranging from 3.5 - 6.0 MeV of TB2 structure. See more details in text.

state decays into the fixed 13^- state at 9214 keV via 3115 keV transition. The in-band transitions of TB2a and TB2b have $E2$ nature, and connecting

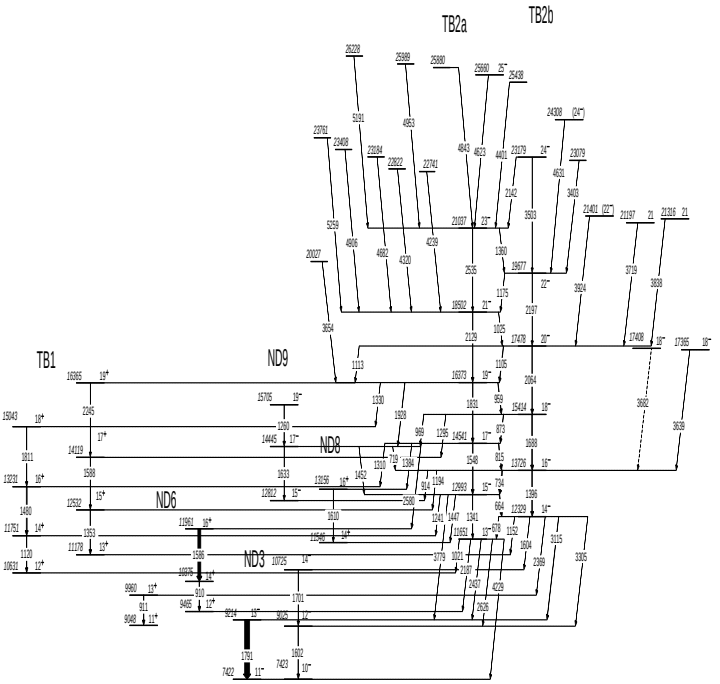

Figure 4.7: Structure of TB2 of the present level scheme. Energy labels are in keV and the intensities of the transitions are here indicated by the relative thicknesses of the arrows. Tentative levels and transitions are dashed.

transitions between them have $E2/M1$ character. All these R_{DCO} values are listed in paper III (Table 1) [17].

In addition, the TB2 structure is fed by eighteen 3 - 5.5 MeV high-energy γ-ray transitions, namely at 3403, 3654, 3719, 3838, 3924, 4239, 4320, 4323, 4401, 4623, 4631, 4682, 4843, 4906, 4953, 5191 and 5259 keV. The γ-ray transitions at 3719, 3838, 3924, 4623 and 4631 keV are sufficiently intense to support the corresponding level spin and parity assignments. The remaining transitions are too weak to measure the DCO ratios, thus the corresponding state spin and parity assignments could not be established.

Figure 4.6 (b) shows the γ-ray spectrum in coincidence with any combination of the 664, 679, 734, 815 keV and the 664, 679, 734, 815 and 873 keV $E2/M1$ transitions of structure TB2. In conjunction with the band mem-

bers of TB2a and TB2b, all $E2/M1$ transitions in between them are also clearly seen. The rather intense decay-out transitions at 1928, 2437 and 3115 are marked with star (*) symbols in black colour, while all transitions belong to the normal deformed region are marked with star (*) symbols in blue color. Several low-intensity transitions are also visible in the spectrum. Figure 4.6 (c) illustrates the highest energy γ-ray transitions ranging from 3.5 - 6.0 MeV belonging to TB2. The intense decay-out transition at 4229 keV is clearly visible, as well as other weak transitions at 3719 and 3924 keV.

4.3 Well-deformed and Superdeformed Band Structures

The high quality of data set 1, together with data set 2, allowed the current analysis to establish eleven well-deformed high-spin band structures, with I_{max} ranging from 22$\hbar$ to 30$\hbar$, and five superdeformed bands with I_{max} ranging from 29$\hbar$ to 35$\hbar$. All these bands are shown in Fig. 4.1. For a thorough description see [17, 48]. A short summary is given in the following.

In the decay scheme Fig. 4.1, the labelling given to the eleven well-deformed bands is WD1 to WD11. The lowest states of all these bands are connected to the low-spin normal deformed region via linking transitions. WD1 is the most intense high-spin band in the present analysis, with an intensity of about 2% relative to the 954 keV ground state transition. Only one transition at 3887 keV was observed from data set 2 which was placed at the top of the band. The band WD2 consists of two bands, which are signature partners (WD2a with $\alpha = 1$ and WD2b with $\alpha = 0$) and are connected to each other via $E2/M1$ transitions. In-band transitions of all ten bands are consistent with $E2$ character.

The spin and parity assignment for the lowest states of all these bands have been determined by R_{DCO} values of their linking transitions. For example, the lowest state of WD4 at 18516 keV decays into the state 17^+ at 13782 keV via a 4734 keV γ-ray transition. The R_{DCO}(4734) = 1.20(25) is consistent with a stretched $E2$ character, suggesting a 19^+ assignment to the 18516 keV state.

Figure 4.8 shows the coincidence spectrum gated on the decay-out transition at 4734 keV and any one of the band members of WD4 at 1916, 2136 and 2577 keV. The band members of WD4 at 1916, 2136 and 2577 keV are clearly visible. The relevant transitions in the normal deformed region of the level scheme, for an example at 954, 1197, 1232, 1310, 1340, 1522, 1586, 1604, 1791 and 1821 keV, are identified with star (*) symbols in blue.

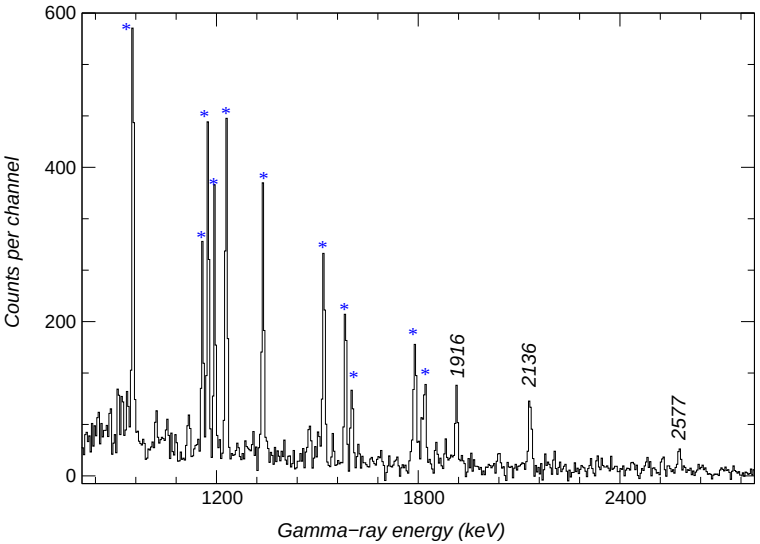

Figure 4.8: Coincidences with the 4734 keV decay-out transition of WD4 and one of the band members of WD4 (1916, 2136 and 2577 keV). Relevant, low-spin transitions are marked with star (*) in blue, while the band members at 1916, 2136 and 2577 keV are labelled with their energies.

Superdeformed bands are labelled with SD1, SD2, SD3, SD4 and SD5 in Fig. 4.1. All five bands are connected to the low-spin states by several linking transitions. This provides spin and parity assignments to the lowest states in the bands, because the transitions at the bottom of the bands are either sufficiently intense or sufficiently clean to distinguish between stretched quadrupole and dipole characters of some of the more intense linking transitions.

The previously observed band SD1 was extended [48] by adding transitions at 3580, 3958, and 4234 keV on the top of the state at 32917 keV. SD1 and SD2 are signature partner bands. The maximum spin in the current analysis is 35^- for the 42517 keV state belonging to SD2. The topmost three transitions of SD1 and SD2 are observed only in data set 2. The SD3 band is built up by a set of states from 16^+ at E_x = 15482 keV to the state 30^+ at E_x = 33797 keV. The spin and parity of SD3 was confirmed with a strong enough decay-out transition at 5388 keV, which has $E2$ nature. The spin assignment of the SD4 band is tentative and the parity of band is uncertain. The band is built up by a set of levels from 21825 keV to the 36896 keV, and is connected to the low-spin part of the level scheme via the 1774-5898 keV weak intensity γ-ray cascade. The SD5 is built up by a set

of states from 23^- at E_x = 23028 keV to the state (29^-) at E_x = 31397 keV. The assignments of the (25^-), (27^-) and (29^-) states at 25478, 28244 and 31397 keV, respectively, are based on the apparent regular increase of their excitation energies.

Assuming an $E2$ character of the in-band transitions, the tentative spin and parity assignments to the states near the top of the all bands are based on their regular rotational behaviour. All bands spin and parity assignments are given in Fig. 4.1 and are listed in paper III (Table 1) [17].

Figure 4.9 explains the exceptionally high quality of data set 1. The

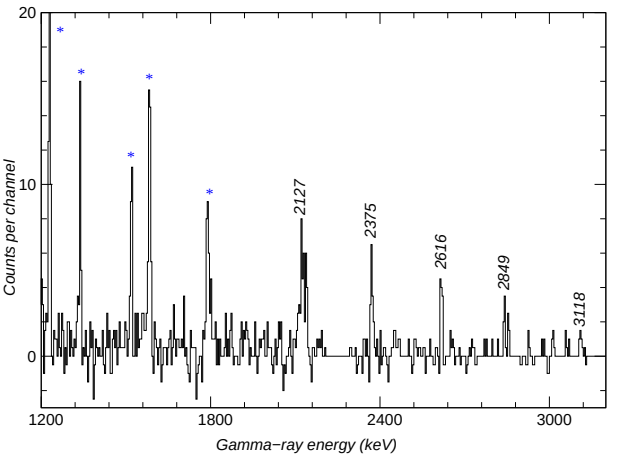

Figure 4.9: Coincidences with the 5388 keV decay-out transition of SD3 and any one of the band members (2127, 2375, 2616 and 2849 keV) of SD3. The relevant low-spin transitions are marked with star (*) in blue. The band members at 2127, 2375, 2616, 2849 and 3118 keV are marked with their energies. See text for more details.

figure shows a spectrum in coincidence with the 5388 keV decay-out transition of SD3 and one of the band members of SD3 (2375, 2616, 2849 and 3118 keV). The intensity of 5388 keV is as low as 0.02% relative to the 954 keV ground state transition, whereas the SD3 band intensity is less than 2%. The triple coincidences both with members of SD3 (2127, 2375, 2616, 2848 and 3118 keV) and with the relevant transitions in the low-spin regime like 1232, 1340, 1522, 1586 and 1791 keV, which are marked with a star (*) in blue, are clearly visible. This proves the good and high quality of data set 1.

Chapter 5

Theoretical Discussion

5.1 Nilsson Model

The nuclear shell model [50, 51] is generally thought to describe spherical nuclei, while it fails to explain the properties of deformed nuclei (nuclei with N and Z far from the closed shells) and rapidly rotating nuclei at least in the early implementations. To understand the basic properties of nucleons moving in a deformed nucleus, a deformed shell model was introduced by S.G. Nilsson in 1955 [52], named as the Nilsson model. More details on this model are given in [53]. A brief summary is given below.

In the Nilsson model the modified oscillator potential [53, 54] is used to describe the motion of the nucleons. For an axial symmetric deformation, the Nilsson Hamiltonian takes the form

$$H = \frac{-\hbar^2}{2M}\Delta + \frac{1}{2}M(\omega_z^2 z^2 + \omega_\perp^2(x^2+y^2) - 2\kappa\hbar\omega_0 \vec{l}\cdot\vec{s} - \kappa\mu\hbar\omega_0(l^2 - \langle l^2\rangle_N). \quad (5.1)$$

Here ω_0 is the harmonic oscillator frequency in the spherical limit while ω_z and $\omega_\perp$ are the frequencies of the anisotropic oscillator in the z-direction and the directions perpendicular to the z-direction, respectively. The first term provides the kinetic energy of the nucleons and the second term defines a harmonic oscillator potential with quadrupole deformation describing spheroidal shapes. The third term is the spin-orbit coupling, which was introduced to reproduce the empirical shell gaps for different N and Z values already for the spherical shell model [50, 51]. The last term, $(l^2 - \langle l^2\rangle_N)$, is introduced to simulate the surface diffuseness depth, which leads to a proper single-particle ordering by lowering the energies of the large l orbitals within an N-shell. Here the $\langle l^2\rangle_N)$ term is included [55] to keep the average energy of an N-shell unaltered by the l^2 term. The strength of the

$\vec{l} \cdot \vec{s}$ and l^2- terms is determined by the Nilsson parameters, κ and μ.

For small deformations, the single-particle states are defined by the approximate quantum numbers $nlj\Omega$. The parameter Ω is the projection of the total angular momentum (j) on the z-axis, n is the radial quantum number and l is the orbital angular momentum. For large deformations, the single particle states are described by the approximate 'asymptotic quantum numbers', $[N, n_z, \Lambda]\Omega$. Here $N = n_z + n_\perp$ is the principal quantum number, n_z and $n_\perp$ are the number of oscillator quanta in the z-direction and in the perpendicular direction, respectively, while Λ is the projection of the orbital angular momentum on the symmetry axis, i.e., the z- axis.

5.2 Cranking Model

To describe the single-particle motion in a rotating nucleus, the cranking model approximation is frequently used, which was suggested by Inglis in 1954 [56, 57]. The basic idea of the cranking model is the following classical assumption: The nucleus with an angular momentum $I \neq 0$ is rotating with a fixed frequency, ω, around a principle axis.

The cranking Hamiltonian is then given by

$$h^\omega = h - \omega j_x, \tag{5.2}$$

where h^ω is the Hamiltonian in the body-fixed rotating system and h is the single-particle Hamiltonian in the laboratory system, e.g. Eq. 5.1. The x-component of the single-particle angular momentum is denoted by j_x, j_x = $l_x + s_x$. The term $-\omega j_x$ is analogous to the Coriolis and centrifugal forces in classical mechanics. The eigenvalues of h^ω are the single-particle energies in the rotating system, which are generally referred to as Routhians, e_i^ω. The total single-particle energy is calculated as the sum of the expectation values of the "single-particle energies" in the laboratory system,

$$E_{tot} = \sum_{occ} \langle h_i \rangle = \sum_{occ} e_i^\omega + \omega \sum_{occ} \langle j_x \rangle_i \tag{5.3}$$

The total angular momentum, I, is approximated by the sum of the expectation values of the $\langle j_x \rangle$ operator.

$$I \approx I_x = \sum_{occ} \langle j_x \rangle_i \tag{5.4}$$

In Eqs.5.3 and 5.4, $\sum_{occ}$ refers to the sum over the occupied proton and neutron orbitals. For the nuclear shapes considered here, the cranking

Hamiltonian is invariant under a rotation of 180° around the x-axis,

$$R_x = R_x(\pi) = \exp(-i\pi j_x) \tag{5.5}$$

The eigenvalue of the R_x operator is r = exp (-i$\pi\alpha$), where the signature quantum number α is used to classifiy the single-particle orbitals. The total signature of a system is defined as the sum of the signature for the occupied orbitals,

$$\alpha_{tot} = \alpha = (\sum_{occ} \alpha_i) \bmod 2 \tag{5.6}$$

The value of α determines the possible spin values through the relation

$$\alpha = I \bmod 2, \tag{5.7}$$

Thus for an even number of nucleons we have α = 0 for I = 0, 2, 4 and α = 1 for I = 1, 3, 5, while for systems with an odd particle number, $\alpha = +1/2$ for I = 1/2, 5/2, 9/2 and $\alpha = -1/2$ for I = 3/2, 7/2, 11/2. Furthermore, we will only consider shapes that are invariant under reflection, $\vec{r} \rightarrow -\vec{r}$. This gives that parity is also a good quantum number.

5.3 Cranked Nilsson-Strutinsky (CNS) Calculations

To understand the experimentally observed bands in ^{62}Zn, configuration-dependent cranked Nilsson-Strutinsky (CNS) calculations [1, 58, 59] were carried out. In this formalism, the cranked Nilsson (modified oscillator) Hamiltonian is used to describe a nucleon in the rotating nucleus.

$$h^\omega = h_{osc}(\varepsilon_2, \gamma) - V^{'} - \omega j_x + 2\hbar\omega_0\rho^2\varepsilon_4 V_4(\gamma), \tag{5.8}$$

The deformed harmonic-oscillator Hamiltonian h_{osc}, with different oscillator frequencies ω_x, ω_y and ω_z is expressed as (cf. Eq. 5.1)

$$h_{osc} = \frac{p^2}{2m} + \frac{1}{2}m(\omega_x^2 x^2 + \omega_y^2 y^2 + \omega_z^2 z^2). \tag{5.9}$$

Generally these three frequencies are expressed in terms of quadrupole deformation coordinates ε_2 and γ [60], corresponding to the different ellipsoidal shapes.

$$\omega_i = \omega_0(\varepsilon_2, \gamma)[1 - \frac{2}{3}\varepsilon_2 \cos(\gamma + i\frac{2\pi}{3})],\ i = x, y, z. \tag{5.10}$$

The parameter ε_2 gives the degree of the deformation of the nucleus, while γ gives its degree of axial asymmetry. Figure 5.1 shows the values

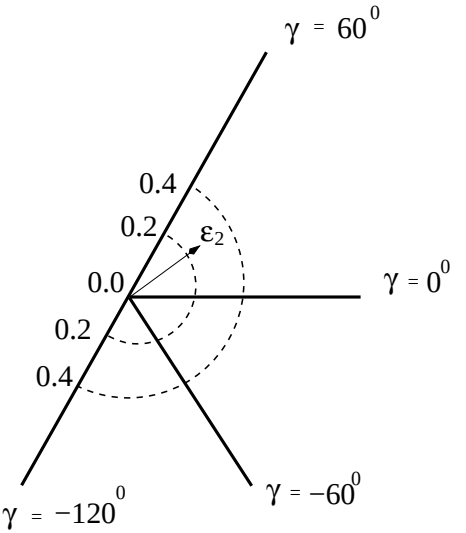

Figure 5.1: The (ε_2, γ) half plane, describing the shape and rotation axis of the nuclear potential.

of ε_2 and γ, which are used to describe all possible ellipsoidal shapes with rotation around the three principal axes. $\varepsilon_2 = 0$ corresponds to a spherical nucleus. The $\gamma = 0°$ axis refers to prolate shape, whereas the $\gamma = -60°$ axis refers to oblate shape. These two shapes are axially symmetric with collective rotation around the perpendicular axis. At the border line, the nucleus rotates around the oblate ($\gamma = 60°$) or prolate ($\gamma = -120°$) symmetry axis corresponding to the non-collective limit. Away from the axes, ($0° < \gamma < 60°$), ($0° < \gamma < -60°$) and ($-60° < \gamma < -120°$), the nuclear shape is triaxial, with rotation around the shorter, the intermediate and the longer principal axis, respectively.

The second term in Eq.5.8,

$$V^{'} = \hbar\omega_0^0 \kappa_N 2\vec{l_t} \cdot \vec{s} + \mu_N (l_t^2 - \langle l_t^2 \rangle_N), \tag{5.11}$$

was already discussed in connection with the Nilsson model. The index t in the orbital angular momentum operator $\vec{l_t}$ indicates that it is defined in stretched coordinates [60]. The strengths of the $\vec{l_t} \cdot \vec{s}$ and l_t^2 terms are dependent on N, by introducing N-dependent κ and μ parameters. A higher order hexadecapole deformation, $2\hbar\omega_0\rho^2\varepsilon_4 V_4(\gamma)$, is also included, where ρ is the radius in the stretched coordinate system.

In these calculations, the Hamiltonian is diagonalized using the eigenfunctions of the rotating oscillator [61], $|n_x n_2 n_3 \Sigma\rangle$, as basis states. The main

advantage of the rotating basis is that N_{rot} can be treated as a good quantum number, where $N_{rot} = n_x + n_2 + n_3$. One advantage of these calculations over the shell-model calculations is that the model space is practically unlimited.

Generally the CNS model is referred to as configuration dependent, because it becomes possible to make a rather detailed specification of configurations. In this approach they are specified by the number of particles with signature $\alpha = 1/2$ and $\alpha = -1/2$, respectively, in each N_{rot} shell. Furthermore, within each N_{rot}-shell, it is generally possible to distinguish between orbitals which have their main amplitudes in the high-j intruder shell and the low-j orbitals which have their main amplitudes in the other j-shells. In the $A \sim 60$ mass region, the involved shells are $N_{rot} = 3$ and $N_{rot} = 4$. For the $N_{rot} = 3$ shell, the $1f_{7/2}$ and for the $N_{rot} = 4$ shell, the $1g_{9/2}$ orbitals are considered as high-j. The remaining orbitals in the respective shells are treated as low-j.

Table 5.1: Occupation of different high- and low-j N_{rot} orbitals of different signature α for a ^{62}Zn proton configuration with one hole in $1f_{7/2}$ and one particle in $1g_{9/2}$.

	N_{rot} =	0	1	2	3	4	5
$\alpha = -1/2$	low-j	0	1	3	1	0	0
	high-j	1	2	3	3	0	0
$\alpha = +1/2$	low-j	0	1	3	1	0	0
	high-j	1	2	3	4	1	0

A typical configuration for $Z = 30$ has one proton hole in $1f_{7/2}$ and one proton particle in the $1g_{9/2}$ subshell. One way of filling the different high-j and low-j orbitals with different signatures $\alpha = \pm 1/2$ is shown in Table 5.4. Note, in an even N_{rot}-shell with few particles, for the intruder orbitals at the bottom of the shell, $\alpha = 1/2$ orbital occupation is favored, whereas in an odd N_{rot}-shell, the $\alpha = -1/2$ orbital occupation is favoured (see Figs. 5.3 and 5.8). In these calculations, the configurations are fixed, and the total energy for each configuration is then minimized in terms of deformation using the parameters specified above ($\varepsilon_2, \gamma, \varepsilon_4$). The calculations do not include pairing. Therefore, they are realistic at high spins, but they can give at least a qualitative description of the lower-spin states as well.

5.3.1 Computer Calculations

In the practical calculations, the programs, which are illustrated in the flowchart of Fig. 5.2, need to be run. At the beginning the calculations

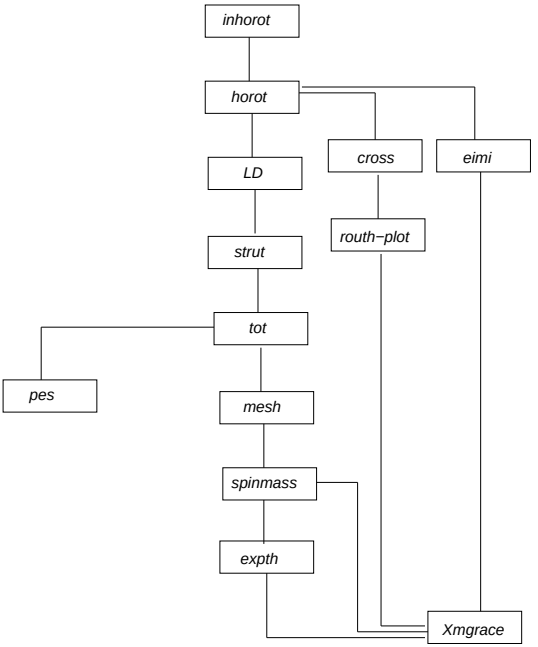

Figure 5.2: Illustration of the standard flow through the computer programs used in the CNS calculations. All these names refers to the corresponding programs in FORTRAN code.

were performed with the standard values of the Nilsson parameters, κ and μ. In Table 5.2, the κ and μ' values of protons and neutrons for $N_{rot} = 0, 1, 2, 3, 4, 5$ are reported. Here $\mu' = \kappa \cdot \mu$. These are of empirical origin and taken from [58]. These values are slightly different for protons and neutrons and vary for the different N_{rot}-shells.

In the $inhorot$ program, one can define a mesh in the (ε_2, γ) deformation plane by introducing a Cartesian (x, y) coordinate system with the y-axis along the $\gamma = -120°/60°$ axis. The number of points in x- and y-directions, and the spacing between the points is selected. Each point in the mesh represents a specific value of ε_2 and γ. In addition, the number of points in ε_4 and their values are specified. The total number of points in a mesh are $N_x \cdot N_y \cdot N_{\varepsilon_4} \cdot N_\omega$. Here N_x and N_y are the number of points along x and y directions, of the (ε_2, γ) plane. N_{ε_4} and N_ω are the number

Table 5.2: Nilsson parameters of different N_{rot} shells

N_{rot} =	protons	neutrons
	$\kappa, \mu^{'}$	$\kappa, \mu^{'}$
0	0.12, 0.0	0.12, 0.0
1	0.12, 0.0	0.12, 0.0
2	0.105, 0.0	0.105, 0.0
3	0.090, 0.0270	0.090, 0.0225
4	0.065, 0.0370	0.070, 0.0273
5	0.060, 0.0390	0.062, 0.0266

of ε_4 and ω values, where ω is the rotational frequency.

The $inhorot$ program creates an input file for $horot$. The $horot$ program is used to calculate the single-particle energies in the mesh points. For every deformation point in the mesh, the LD program will calculate the rotating liquid drop energies using the rigid body moments of inertia. Here the static liquid drop parameters are taken from the Lublin-Strasbourg drop (LSD) [59, 62]. The rigid body moments of inertia are calculated for a nucleus with a diffuse surface having a radius parameter r_0 = 1.16 fm and a diffuseness parameter, $a = 0.6$ fm [59, 62]. Renormalization of the static energy and moments of inertia is necessary in the Nilsson potential, so the total energies are Strutinsky renormalized [63, 64] to the rotating liquid-drop behaviour. A brief description is given here. Liquid-drop models succeed to explain the bulk properties/macroscopic effects of the nucleus, but they fail to explain shell effects, which on the contrary are understood from a quantum mechanical approach. To combine the two models the Strutinsky shell correction/ renormalization method is introduced [63, 64]. The resulting shell correction energy, E_{shell}, is then calculated as, $E_{shell} = E_{s.p} - \tilde{E}_{shell}$, where $E_{s.p}$ is the sum of the single particle energies and $\tilde{E}_{shell}$ is the Strutinsky smoothed sum. The Strutinsky renormalization is carried out in the $strut$ program.

The program tot is used for two purposes. One purpose is to perform the $scan$ calculations and another is to run for fixed configurations, like the example given in Table 5.1. The yrast states of the different combinations of parity and signature are searched in a $scan$ calculation. As already mentioned, in this approach it is possible to identify the orbitals having their main amplitudes in the j-shell with the largest j-value within each N_{rot}-shell. As a result, a large number of different configurations in the yrast

region can be determined. The total spin is calculated as the sum of the expectation values of j_x for the occupied orbitals. The total energy E_{tot} at a specific deformation $(\varepsilon_2, \gamma, \varepsilon_4)$ and specific spin I is calculated as the sum of rotating liquid drop energy and the shell energy using the tot program.

The energy can be illustrated as potential energy surfaces in the (ε_2, γ)-plane and the plots are made in the pes program. The $mesh$ program is used to make interpolations to find out the energy minima at each spin with respect to deformation. The $spinmass$ program is used to create input files to the plotting program like, energies vs. spin, $J^{(1)}$ and $J^{(2)}$ moments of inertia and nuclear shape trajectories in the deformation space as a function of I for different configurations. The plotting program $Xmgrace$ is used to create the different plots. To compare the calculated and experimental energies on an absolute scale, the $expth$ program is used.

Finally, to plot the single-particle energies as function of rotational frequency at a fixed deformation, and to plot single-particle energies e_i at a rotational symmetric deformation vs. spin projection m_i, the programs called $cross$, $routh\text{-}plot$ and $eimi$ need to be performed.

The results from these programs, which were applied to ^{62}Zn and other nuclei in the $A = 60$ region, are reported in the following sections.

5.3.2 Theoretical Interpretations on ^{62}Zn

The ground state of ^{62}Zn can be viewed as a ^{56}Ni core plus six valence nucleons outside the core. The orbitals which are involved in a theoretical description of ^{62}Zn include the $N = 3$ high-j $1f_{7/2}$ shell, the upper low-j (fp) shells $1f_{5/2}$, $2p_{3/2}$, and $2p_{1/2}$, and finally the $N = 4$ shell $1g_{9/2}$. The j-shells are pure only if the shape is spherical. In the deformed rotating potential, these j-shells will mix. i.e., in the present approximation the wave functions of the single-particle orbitals will have amplitudes in all the j-shells of a specific N_{rot}-shell. However, it turns out that if the deformation is not too large, these orbitals can be classified as having their main amplitudes in either the high-j intruder shell or in the other shells with smaller j-values [1, 20].

Figure 5.3 shows the calculated single-particle orbitals (routhians) for neutrons as a function of the rotational frequency for a typical deformation for low-spin states, $\varepsilon_2 = 0.226$, $\gamma = 15°$ and $\varepsilon_4 = 0.01$. Due to the low Coulomb effects, the single-particle orbitals for protons and neutrons are almost identical. The main difference is the Fermi energy, which is higher for neutrons than for protons. Dashed lines are used for negative parity and dots for signature $\alpha = -1/2$, i.e. solid lines for $(\pi, \alpha) = (+, +1/2)$, dotted lines for $(+, -1/2)$, dashed lines for $(-, +1/2)$ and dot-dashed lines for $(-, -1/2)$. The orbitals are labelled according to which j-shell or group of

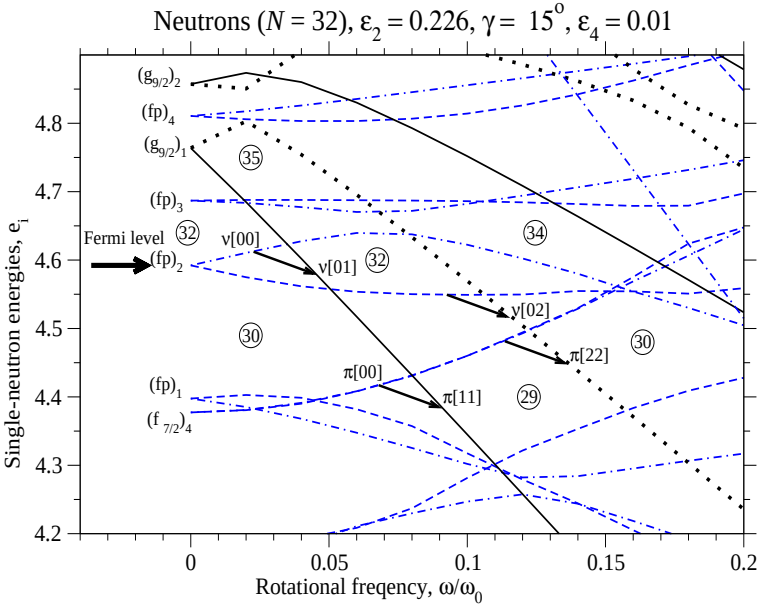

Figure 5.3: Single neutron orbitals, routhians, plotted as a function of rotational frequency, $\frac{\omega}{\omega_0}$. The energies are calculated at a constant deformation of $\varepsilon_2 = 0.226$, $\gamma = 15°$ and $\varepsilon_4 = 0.01$. The arrow on the left hand side indicates the Fermi level for $N = 32$ at $\omega = 0$. Particle numbers at some energy gaps are encircled. The orbitals are labelled by the group to which they belong and the ordering in the group at rotational frequency, $\omega = 0$. See text for details.

j-shells they belong and the ordering in the group at rotational frequency $\omega = 0$. The (fp) group indicates the mixing of the $1f_{5/2}$ and $2p_{3/2}$ subshells. It is not really possible to make a distinction between the $1f_{5/2}$ and $2p_{3/2}$ shells. The mixing probability of the $2p_{1/2}$ subshell is low for these orbitals, i.e. the $2p_{1/2}$ subshell does not contribute significantly to the wave-functions of the upper fp shell orbits which are active in ^{62}Zn. The large signature splitting of the lowest high-j $1g_{9/2}$ intruder orbital means that for configurations with one $1g_{9/2}$ neutron (or proton), one expects to observe only the favoured $\alpha = +1/2$ signature.

The short-hand notation of each rotational band is based on the number of particles in different j-shells for each configuration, see Table 5.1. In general the labelling refers to the dominating shell only, while the wave functions also contain components from other j-shells. A configuration

can be written as:

$$\pi[(1f_{7/2})^{-p_1}(1g_{9/2})^{p_2}(fp)^{p_3}] \otimes \nu[(1f_{7/2})^{-n_1}(1g_{9/2})^{n_2}\nu(fp)^{n_3}] \qquad (5.12)$$

which provides a possibility of giving the short-hand notation [p_1p_2,n_1n_2]. Here p_1 (n_1) denotes the number of $1f_{7/2}$ proton (neutron) holes and p_2 (n_2) number of $1g_{9/2}$ protons (neutrons). The parameter p_3 (n_3) denotes the number of particles in the low-j fp-subshells ($1f_{5/2}$, $2p_{3/2}$, and $2p_{1/2}$). They are fixed to get the correct number of particles, i.e., $p_3 = 2+p_1-p_2$ and $n_3 = 4 + n_1 - n_2$ for ^{62}Zn. The signature of an odd number of fp- particles is sometimes specified as [$p_1(+/-)p_2, n_1(+/-)n_2$] for signature $\alpha = +1/2$ and $\alpha = -1/2$, respectively.

In the ground state of ^{62}Zn only the low-j $N_{rot} = 3$ shells are active. More deformed, higher-spin configurations are formed by making particle excitations into the deformation-driving $1g_{9/2}$ orbitals and/or generating holes in the $1f_{7/2}$ orbitals. For example, as shown in Fig. 5.3, the lowest possible neutron configuration $\nu[(fp)^4]$ is labelled as ν[00]. At $\frac{\omega}{\omega_0} \approx 0.03$, the $\alpha = -1/2$ $(fp)_2$ and the favoured $(g_{9/2})_1$ orbitals cross, which means that the occupation of the $\alpha = 1/2$ $(1g_{9/2})_1$ neutron orbital is favoured in energy at frequencies $\frac{\omega}{\omega_0} \gtrsim 0.03$. The corresponding configuration $\nu[(fp)^3(1g_{9/2})^1]$ is labelled ν[01]. At $\frac{\omega}{\omega_0} \approx 0.11$, the $\alpha = 1/2$ $(fp)_2$ and the $\alpha = -1/2$ $(g_{9/2})_1$ orbitals cross, so that the occupation of the $\alpha = -1/2$ $(g_{9/2})_1$ orbital is favoured at $\frac{\omega}{\omega_0} \gtrsim 0.11$. The corresponding configuration $\nu[(fp)^2(1g_{9/2})^2]$ is labelled as ν[02].

For the protons the signature degenerate $(1f_{7/2})_4$ orbitals cross the $(1g_{9/2})_1$ orbital at $\frac{\omega}{\omega_0} \approx 0.08$. At higher frequencies the occupation of the $\alpha = 1/2$ $(1g_{9/2})_1$ orbital together with one of the $(1f_{7/2})_4$ orbitals is favoured. The corresponding configuration $\pi[(1f_{7/2})^{-1}(1g_{9/2})^1]$ is labelled π[11]. At $\frac{\omega}{\omega_0} \approx 0.12$ the $(1f_{7/2})_4$ orbitals cross the $\alpha = -1/2$ $(1g_{9/2})_1$ orbital, so that the occupation of two $(1g_{9/2})_1$, and no $(1f_{7/2})_4$ orbitals, is favoured at higher frequencies. The corresponding configuration $\pi[(1f_{7/2})^{-2}(1g_{9/2})^2]$ is labelled as π[22]. Returning to the neutrons, at $\frac{\omega}{\omega_0} \approx 0.15$ the orbitals $(1f_{7/2})_4$ and $(fp)_2$ cross, so that at higher frequencies it is favourable to make also two neutron holes in the $(1f_{7/2})_4$ orbitals. All these orbital crossings occur at a constant deformation of $\varepsilon_2 = 0.226$ and $\gamma = 15°$, $\varepsilon_4 = 0.01$, but they give a basic idea of which configurations are favoured in general.

5.3.3 Predictions on Low and Medium-spin Structures

Figure 5.4 shows the calculated energies for a selection of fixed configurations in the yrast region of ^{62}Zn, drawn relative to the liquid drop energy. The solid (dashed) lines correspond to positive (negative) parity states and

filled (open) symbols correspond to a signature of $\alpha = 0(1)$. The aligned states at, or very close to, $\gamma = 60^\circ$ are encircled. The band configurations shown in panel (a) have no particle excitations from $1f_{7/2}$, whereas the bands displayed in panel (b) have one proton hole in $1f_{7/2}$. Thus the maximum spin for the configurations in panel (a) is 10 to 19$\hbar$ and in panel (b) 14 to 26$\hbar$ (see below). All configurations are labelled with the shorthand notation [$p_1(+/-)p_2$,$n_1(+/-)n_2$].

With 2 protons and 4 neutrons outside the $Z = N = 28$ shell gap, the lowest spin configuration is labelled as [00,00] with $I_{max} = 10^+$, corresponding to the ground-state band ND1 (see in the level scheme in Fig. 4.1 and [17]). By exciting one (fp) neutron into the intruder $1g_{9/2}$ shell, the configuration $\pi[(fp)^2_4] \otimes \nu[(fp)^3_{4.5}(1g_{9/2})^1_{4.5}]$ is formed. It is labelled as $[00, 0(+)1]$ and terminating at $I_{max} = 13^-$. The other signature configuration $\pi[(fp)^2_4] \otimes \nu[(fp)^3_{5.5}(1g_{9/2})^1_{4.5}]$ labelled as $[00, 0(-)1]$ is terminating at $I_{max} = 14^-$. The subscripts indicate the maximum spin contribution from each j-shell or group of j-shells. These two calculated signature partner configurations are in good agreement with the experimentally observed ND3 structure with two signatures ND3a and ND3b (see in the level scheme in Fig. 4.1 and [17]).

In the configuration labelled [00,01$_-$], the minus sign indicates that the $g_{9/2}$ neutron occupies the unfavoured signature, orbital $\alpha = -1/2$. Because of the large signature splitting for this intruder orbital, the [00,01$_-$] configurations with signatures $\alpha = \pm 1/2$ for the (fp) neutrons are at higher energy than other similar configurations discussed above. The configuration with two neutrons in $1g_{9/2}$, which is labelled as [00,02] can be assigned to observed ND8 (see in the level scheme in Fig. 4.1 and [17]).

The configuration with one proton in the $1g_{9/2}$ subshell, $\pi(1g_{9/2})^1$ combined with the neutron configuration $\nu(1g_{9/2})^1$, results in two pairs of signature partners which are marked with case 1 and case 2 inside the figure. The case 1 configuration [0(+)1,0(+)1] terminates in the state, $\pi[(fp)^1_{2.5}(1g_{9/2})^1_{4.5}]$ $\otimes\nu[(fp)^3_{4.5}(1g_{9/2})^1_{4.5}]$ i.e at $I_{max} = 16^+$. In the other signature partner configuration, $[0(+)1, 0(-)1]$, the spin of the (fp) proton is 1.5 instead in the terminating $I_{max} = 15^+$ state. In a similar way, the case 2 signature partner configurations $[0(-)1, 0(+)1]$ and $[0(-)1, 0(-)1]$ are terminating at $I_{max} = 17^+$ and $I_{max} = 16^+$ respectively. It is clearly seen in the figure, that the case 2 configurations are at higher energy than the case 1 configurations at their terminating spin states.

This can be understood from Fig. 5.5, which illustrates the single-particle energies at an axial symmetric deformation drawn vs. their projection of the single-particle angular momentum m_i on the symmetry axis. The orbitals are connected and labelled by the respective j-shells where they have

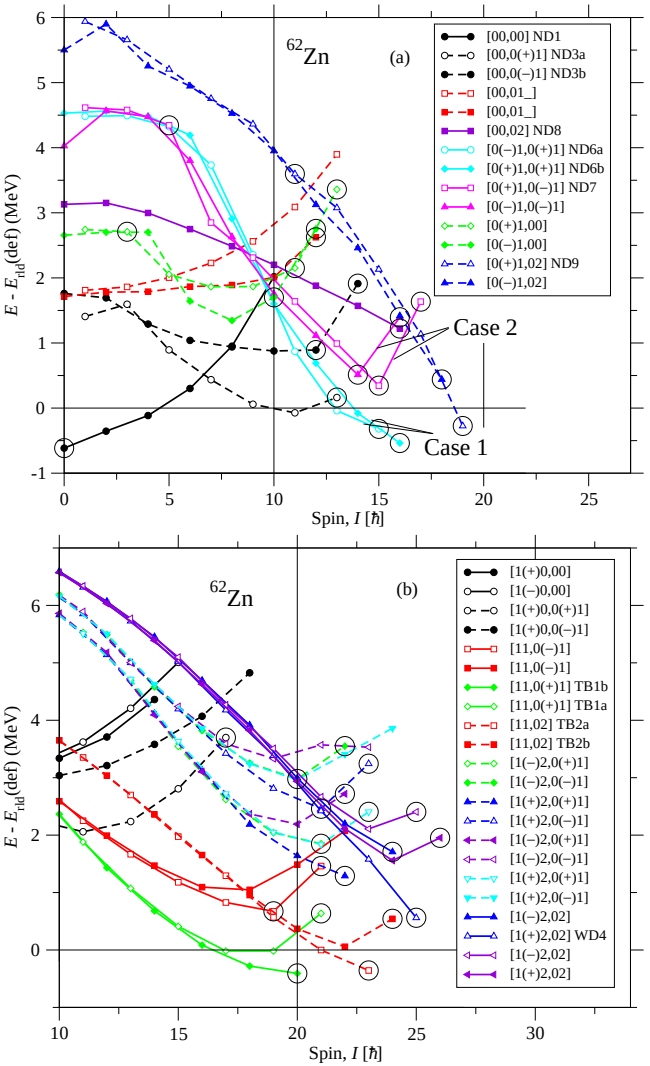

Figure 5.4: Calculated energies for a selection of fixed configurations in the yrast region of ^{62}Zn, drawn relative to the rotating liquid drop energy. The positive (negative) parity states are represented with solid (dashed) lines and filled (open) symbols belong to a signature of $\alpha = 0(1)$. Non-collective aligned states are encircled. The configurations in panel (a) are illustrated for no particle excitations, whereas those in panel (b) are for one proton particle excitation across the $Z = N = 28$ shell gap. See text for details.

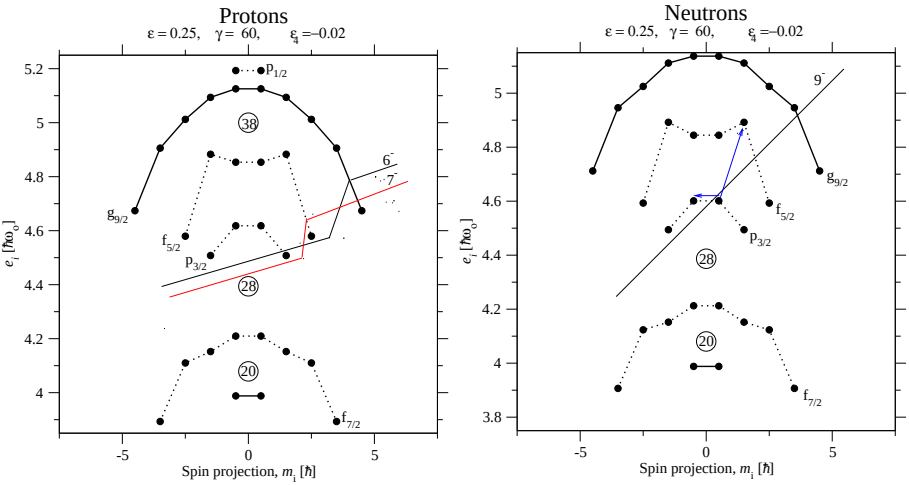

Figure 5.5: The sequence of the proton and neutron single-particle states drawn as energy vs. spin projection and the position of the respective sloping Fermi surfaces relative to the single particle levels. See text for more details.

their main amplitudes. In this kind of sloping Fermi surface diagrams [53, 64], favoured aligned states are formed in configurations defined by straight-line, or close-to-straight-line Fermi surfaces, where all orbitals below the Fermi surface are occupied and those above are empty.

Figure 5.5 is drawn at the deformation found for the $I_{max} = 15^+$ terminating state. With approximately the same deformation for the other aligned [01,01] states, it is now possible to draw the Fermi surfaces in the figure. The two signature partner proton configurations have a similar energy cost per spin unit in the terminating state as seen from the corresponding Fermi surfaces drawn with a solid red and black lines in a panel (a). For the neutron configurations on the other hand, the energy cost per spin unit is different in case 1 and case 2 as can be understood from panel (b).

Thus in case 1, the third (fp) neutron is in the $2p_{3/2,m=1/2}$ orbital corresponding to a straight-line Fermi surface, see panel (b), and thus favoured in energy. In case 2 with opposite signature, the third (fp) neutron can be moved to the $2p_{3/2,m=-1/2}$ orbital resulting in aligned states at $I = 14, 15$ with rather low energies. Then, however, the maximum spin in these configurations are obtained with the third (fp) neutron in the $f_{5/2,m=3/2}$ orbital instead. As seen in panel (b), this orbital is very high in energy relative to the straight line Fermi surface corresponding to a kink for case 2 in Fig. 5.4 with high-lying $I = 16, 17$ states.

The high energy of the 14^- state in the [00,0(−)1] configuration is explained by the same mechanism.

The [01,01] signature partner of the case 1 configurations are in nice agreement with experimentally observed ND6 structure with signature partners ND6a and ND6b (see the level scheme in Fig. 4.1 and [17]). The highest spin state of $[0(+)1, 0(-)1]$ configuration can be assigned to the observed band ND7 (see the level scheme in Fig. 4.1 and [17]). With two neutrons in $1g_{9/2}$, the signature partner configurations $[0(+)1, 02]$, $[0(-)1, 02]$ are terminating at maximum spin 19^- and 18^-. The former configuration fits well with the experimentally observed ND9 structure. The other signature partner configuration is not observed experimentally.

The configurations shown in Fig. 5.4 (b) have one proton hole in $1f_{7/2}$. The $[11, 0(+)1]$ configuration with one proton and one neutron in $1g_{9/2}$ terminates at $I_{max} = 20^+, 21^+$ in the states

$$\pi[(1f_{7/2})^{-1}_{2.5,3.5}(fp)^2_4(1g_{9/2})^1_{4.5}]_{11,12} \otimes \nu[(fp)^3_{4.5}(1g_{9/2})^1_{4.5}]_9. \qquad (5.13)$$

These two configurations are in good agreement with the observed terminating band TB1 with signature partners TB1a and TB1b (see the level scheme in Fig. 4.1 and [17]), respectively. The other combination of signature partner bands [11,0(−)1] are higher in energy with one neutron in the unfavoured signature $\alpha = -1/2$ branch of the $(fp)_2$ orbital (see Fig. 5.3).

With one more neutron in $1g_{9/2}$, signature partner configurations [11,02] are formed. They terminate at $I_{max} = 23^-, 24^-$ in the states

$$\pi[(1f_{7/2})^{-1}_{2.5,3.5}(fp)^2_4(1g_{9/2})^1_{4.5}]_{11,12} \otimes \nu[(fp)^2_4(1g_{9/2})^2_8]_{12}. \qquad (5.14)$$

These two calculated signature partner bands are in good agreement with the observed terminating signature partner bands TB2a and TB2b (see the level scheme in Fig. 4.1 and [17]). The calculated bands with the configuration [12,02] have the highest terminating spins in Fig. 5.4, $I_{max} = 22 - 26^+$. The [1(+)2,02] band with $I_{max} = 25^+$ can be assigned to the observed band WD4.

In addition to the bands discussed here, additional bands of the type [10,00], [10,01] and [12,01] are shown in Fig. 5.4 (b). They are formed with different combinations of the signatures for the $1f_{7/2}$ proton hole and for the (fp) proton and neutron. They are all calculated at a rather high energy and appear not to have experimental correspondences.

Figure 5.6 shows the calculated total potential energy surfaces for the [11,02] configuration with negative parity and signature $\alpha = 1$. The calculated maximum spin for this configuration is $I_{max} = 23^-$. In these figures, the contour line separation is 0.2 MeV. The lowest energy minima are indicated with filled black circles. For the lowest spin values $I = 11^-, 13^-$

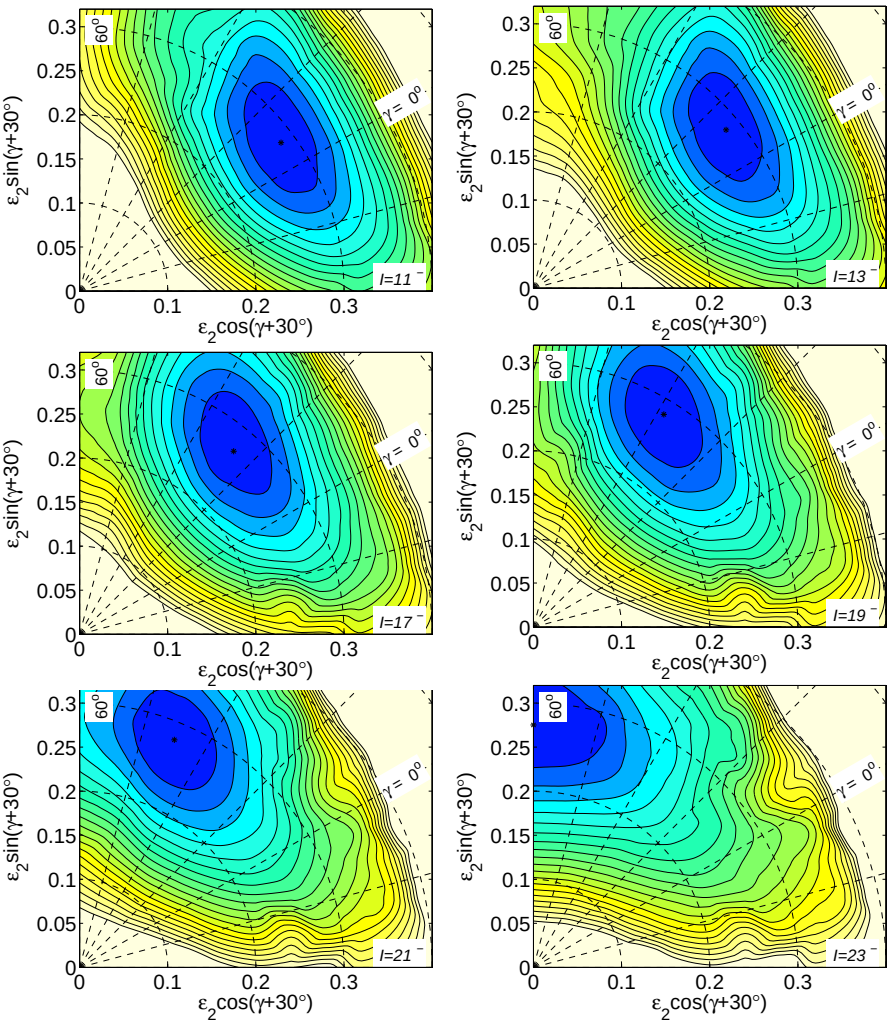

Figure 5.6: Calculated potential energy surfaces for the [11,02] configuration with negative parity and $\alpha = 1$ signature. The contour line separation is 0.2 MeV. See text for details.

shown in the figure, the lowest energy is found at γ = 0° - 20°, indicating a large collectivity at these spin values. For medium spin values $I = 17^-, 19^-, 21^-$, the minimum is located at γ = 20° - 40°, indicating reduced collectivity. For the maximum spin value of [11,02] at $I = 23^-$, the lowest minimum is at $\gamma = 60°$ corresponding to a non-collective state. This type

of non-collective yrast states at $\gamma = 60^\circ$ are encircled in the $E - E_{rld}$ plots.

5.3.4 Predictions on Well-deformed Structures

Figure 5.7 is analogous to Fig. 5.4, but the configurations in panel (a) have one proton hole and one neutron hole in the $1f_{7/2}$ shell, while those in panel (b) have two proton holes in the $1f_{7/2}$ shell. The highest spin for the configurations in both panels is 24 to 30$\hbar$. All configurations in Fig. 5.7 are labelled with the shorthand notation [p_1p_2,n_1n_2].

The [11,11] configuration with one proton and one neutron in the $1g_{9/2}$ subshell, results in two pairs of signature partners. These calculated bands are at a rather high energy with no observed bands assigned to them.

With one more neutron in $1g_{9/2}$, four pairs of signature partner configurations with negative parity $[11, 1(+/-)2]$ are formed. With the same convention as in Fig. 5.4, the $(+/-)$ sign indicates signature of the (fp) particle. The lowest calculated signature partner bands terminate at $I_{max} = 26^-, 27^-, 27^-, 28^-$ in the states

$$\pi[(1f_{7/2})^{-1}_{2.5,3.5}(fp)^2_4(1g_{9/2})^1_{4.5}]_{11,12} \otimes \nu[(1f_{7/2})^{-1}_{2.5,3.5}(fp)^3_{4.5}(1g_{9/2})^2_8]_{15,16}. \tag{5.15}$$

Two of these calculated signature bands can be assigned to the observed WD2a and WD2b bands. The other negative signature configuration may be associated with the observed bands WD6 or WD7.

With three neutrons in $1g_{9/2}$, two pairs of signature partner configurations [11,13] are formed. The lowest positive signature band of this type 'terminates' at $I_{max} = 28^+$, and can be assigned to the observed band WD8. No observed bands are assigned to the other [11,13] bands.

The $[2(+/-)1, 0(+/-)1]$ configuration in Fig. 5.7 (b) with one proton and one neutron in $1g_{9/2}$, results in four bands with a rather large signature splitting. All these calculated bands are at a rather high energy. The lowest energy configuration $[2(+)1, 0(+)1]$ terminates at $I_{max} = 24^+$ in the state

$$\pi[(1f_{7/2})^{-2}_6(fp)^3_{4.5}(1g_{9/2})^1_{4.5}]_{15} \otimes \nu[(fp)^3_{4.5}(1g_{9/2})^1_{4.5}]_9 \tag{5.16}$$

This configuration can be assigned to the observed band WD10.

With one proton and two neutrons in $1g_{9/2}$, one pair of signature partner configurations $[2 \pm 1, 02]$ is formed. The odd spin partner ($\alpha = 1$) is lower in energy than even spin band ($\alpha = 0$) . The maximum spin for these two bands are at $I_{max} = 27^-, 28^-$ in the state

$$\pi[(1f_{7/2})^{-2}_6(fp)^3_{4.5,5.5}(1g_{9/2})^1_{4.5}]_{15,16} \otimes \nu[(fp)^2_4(1g_{9/2})^2_8]_{12} \tag{5.17}$$

The odd spin band $[2(+)1, 02]$ appears to be associated with the observed WD6 and WD7 bands. Both of these bands are at a comparatively low energy. More details on these assignments for WD6 and WD7 are explained

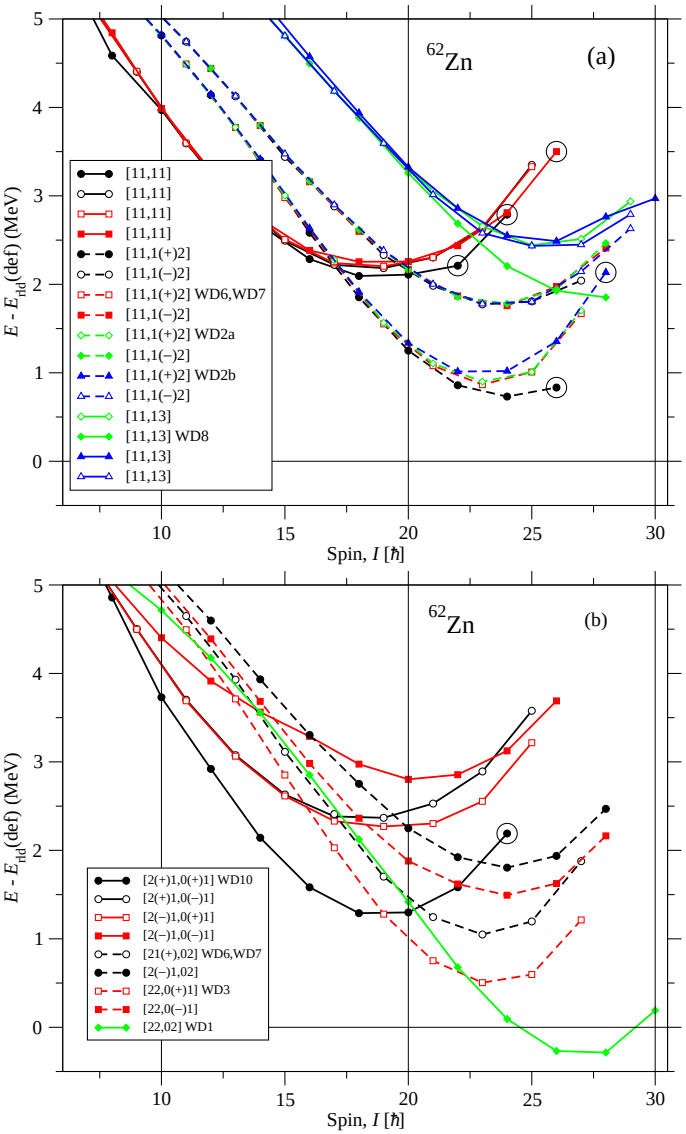

Figure 5.7: Same as Fig. 5.4 but here illustrated for configurations (a) with one proton and neutron hole in the $1f_{7/2}$ shell, and (b) with two proton holes in the $1f_{7/2}$ shell. See text for details.

in Sec. 5.4.1.

The configuration [22,0(+)1] has an $I_{max} = 27^{-}$ state,

$$\pi[(1f_{7/2})_6^{-2}(fp)_4^2(1g_{9/2})_8^2]_{18} \otimes \nu[(fp)_{4.5}^3(1g_{9/2})_{4.5}^1]_9 \tag{5.18}$$

This configuration is in good agreement with the observed WD3 band. The other calculated signature partner band $[22, 0(-)1]$ is at a rather high energy, with no experimental correspondence. The [22,02] configuration has $I_{max} = 30^{+}$ corresponding to the state

$$\pi[(1f_{7/2})_6^{-2}(fp)_4^2(1g_{9/2})_8^2]_{18} \otimes \nu[(fp)_4^2(1g_{9/2})_8^2]_{12} \tag{5.19}$$

This configuration is in good agreement with the observed WD1 band [48].

5.3.5 Predictions on Superdeformed Structures

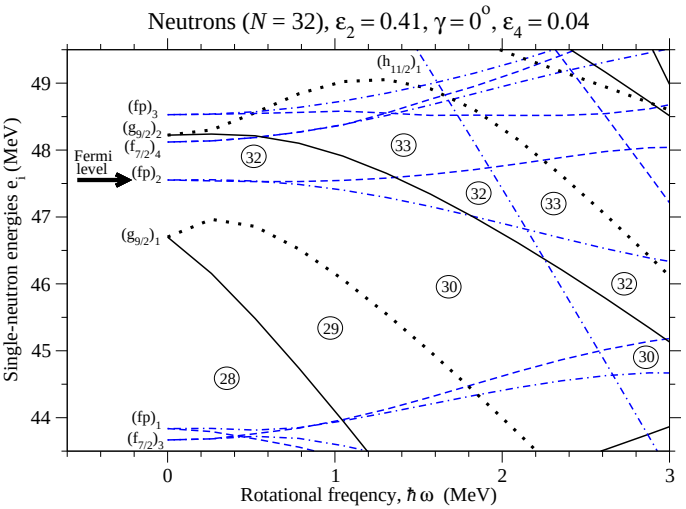

Figure 5.8: Single neutron orbitals, routhians, plotted as a function of rotational frequency, $\hbar\omega$. The energies are calculated for ${}^{62}_{30}Zn_{32}$ at a constant deformation of $\varepsilon_2 = 0.41$, $\gamma = 0°$ and $\varepsilon_4 = 0.04$. The arrow indicates the Fermi level at $\omega = 0$. Particle numbers at some gaps are encircled. The orbitals are labelled by the group to which they belong and the ordering in the group at rotational frequency, $\omega = 0$. See text for details.

Figure 5.8 illustrates the single-neutron orbitals plotted as a function of rotational frequency, $\hbar\omega$, at a typical deformation for the SD bands, $\varepsilon_2 = 0.41$, $\gamma = 0°$ and $\varepsilon_4 = 0.04$. As already mentioned, the single-particle

orbitals for protons and neutrons are almost identical. For $Z = 30$, the $\pi[22]$ configuration is favoured in a large frequency range up to $\hbar\omega \sim 2.3$ MeV. At $\hbar\omega \lesssim 1.5$ MeV for $N = 32$, the $\alpha = \pm 1/2\ (fp)_2$ are the favoured orbitals to fill for the two neutrons above the 30 gap. Therefore, the $\nu[22]$ configuration is favoured for $\hbar\omega \lesssim 1.5$ MeV. At $\hbar\omega \approx 1.5$ MeV the $\alpha = 1/2\ (fp)_2$ and the favoured $(1g_{9/2})_2$ orbitals cross, which means that the occupation of the $\alpha = 1/2\ (fp)_2$ and the favoured $(1g_{9/2})_2$ neutron orbitals are lowest in energy at frequencies $\hbar\omega \gtrsim 1.5$ MeV. At $\hbar\omega \approx 2.3$ MeV the $\alpha = -1/2$ $h_{11/2}$ orbital crosses the lowest $(fp)_2$ orbital. Thus, at higher frequencies, the occupation of the $\alpha = -1/2\ 1h_{11/2}$ orbital together with the $\alpha = 1/2$ $(1g_{9/2})_2$ orbital is favoured for $N = 32$. At $\hbar\omega \approx 2.6$ MeV for $Z = 30$ the $\alpha = -1/2\ 1h_{11/2}$ orbital crosses the $(1f_{7/2})_3$ orbitals, so at higher frequencies at this deformation, it is favourable to fill one $1h_{11/2}$ orbital also for the protons.

Figure 5.9 illustrates selected calculated bands with the proton config-

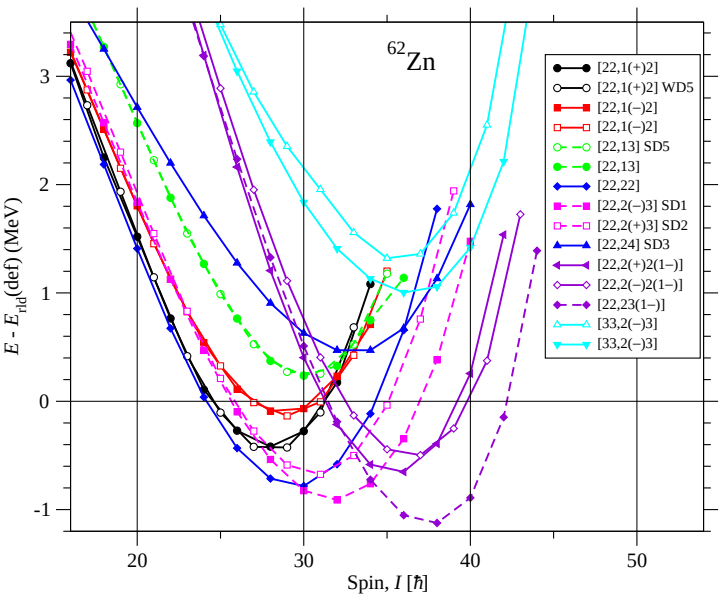

Figure 5.9: Same as Fig. 5.4 but here illustrated for the lowest possible selected calculated bands which have two or three proton holes in the $1f_{7/2}$ shell and one or two neutron holes in the $1f_{7/2}$ shell. See text for details.

uration corresponding to the large $Z = 30$ gap in Fig. 5.8 combined with neutron configurations, where two orbitals above this gap are occupied. In addition, two configurations with a third $1f_{7/2}$ proton hole are included.

The maximum spin values for these bands are in the range 33 to 44$\hbar$.

The favoured proton configuration [22] combined with the neutron configuration $[1(\pm)2]$ with one neutron hole in $1f_{7/2}$ shell and two neutrons in $1g_{9/2}$ shells, leads to two pairs of signature partner bands. The negative signature partner band [22,1(+)2] has been assigned to the observed WD5 band. There is no experimental evidence for the remaining calculated bands with a [22,12] configuration. With one more neutron excited to $1g_{9/2}$, negative parity configurations are formed, which are thus possible assignments for the SD1 and SD2 bands. With the third neutron in the favoured signature of the $(1g_{9/2})_2$ orbital, the signature partner configurations [22,13] and $[22, 2(\pm)3]$ are formed, depending on whether the neutron is excited from the (fp) or $(1f_{7/2})$ orbitals. The [22,23] bands are calculated at a lower energy than the [22,13] bands, so they are our preferred choice for the observed SD1 and SD2 bands [48]. The negative signature partner of [22,13] configuration is a possible candidate for observed SD5 band, while the other positive signature partner band is not observed experimentally.

There are two configurations, [22,22] and [22,24], which can be assigned to the observed SD3 band, but none of them is an ideal choice [48].
Considering the rather strong down-slope around $I = 30$ for the $E - E_{rld}$ curve of the SD4 band, it appears that the calculated configurations discussed so far are not possible assignments. Higher spin configurations are achieved by exciting one neutron to the favoured $h_{11/2}$ orbital or by exciting one proton from the $1f_{7/2}$ orbital. The lowest energy bands of this kind are drawn in Fig. 5.9, where the occupation of the $\alpha = -1/2$ $h_{11/2}$ orbital is shown in parentheses, $(1-)$. One band of this type might be assigned to the observed SD4 band.

5.4 Configuration Assignments for Observed Bands

An overview of the results from the matching between the experimental structures and calculated configurations is found in Table 5.4. Different proton (rows) and neutron (columns) configurations are combined and the maximum spin for each combination is given. Note however that some reassignments are suggested in Ref. [65].

Config. ν π I_{max}	00] 6	0(+)1] 9	0(-)1] 10	02] 12	1(+)2] 15, 16	13] 17	22] 20	2 ($\pm$) 3] 21, 22	24] 22	22(1-)] 24, 25	23(1-)] 26
[00 4	ND1 10	ND3a 13	ND3b 14	ND8 16	20	21	24	25, 26	26	28, 29	30
[0(+)1 7	13	ND6b 16	ND7 17	ND9 19	23	24	27	28, 29	29	31, 32	33
[0(-)1 8	14	ND6a 17	18	20	24	25	28	29, 30	30	32, 33	44
[11 11,12	17 18	TB1b TB1a 20, 21	21 22	TB2a TB2b 23, 24	WD2a WD2b 27,28 WD6, WD7 26,27	WD8 28	31 32	32, 33 33, 34	33 34	35, 36 36, 37	37 38
[1(+)2 13	19	22	23	WD4 25	29	30	33	34, 35	35	37, 38	39
[2(+)1 15	21	WD10 24	25	WD6, WD7 27	31	32	35	36, 37	37	39, 40	41
[22 18	24	WD3 27	28	WD1 30	WD5 34	SD5 35	38	SD2, SD1 39, 40	SD3 40	42, 43	44
[33 21,22	27 28	30 31	31 32	33 34	37 38	38 39	41 42	42, 44 43, 44	43 44	45, 46 46, 47	47 48

Table 5.3: Experimentally observed structures are shown to illustrate their configuration assignments. Horizontal rows illustrate the proton configurations and the vertical columns give neutron configurations with their respective I_{max} values. For each combined neutron and proton configuration the maximum spin is indicated and also the experimental bands in ^{62}Zn, which are assigned to the configurations.

5.4.1 More Details on Assignments

Figures 5.10 and 5.11 illustrate the configuration assignments for the observed bands with positive and negative parity, respectively. In both figures the observed bands have maximum spin $\leq 25\hbar$. The low-spin ND bands, the previously known two terminating bands, and one high-spin deformed band (WD4) are shown in the top panels with the configurations assigned to them in the middle panels and the difference in energy between the two in the bottom panels. In the top and middle panels, the y-axis corresponds to the energy with the rotating liquid drop (rld) energy subtracted [59]. The positive (negative) parity bands have an even (odd) number of $1g_{9/2}$ particles and it is instructive to see how the bands split up in groups with different I_{max} values depending on the number of $1g_{9/2}$ particles.

As we already discussed many details about the calculated configurations in section 5.2.2, we only specify those configurations which correspond to the best fit of the observed bands here.

The observed ground state structure ND1 is assigned to [00,00]. By lifting particles from the fp orbitals to the $g_{9/2}$ orbitals, we successively obtain the $[00, 0(\pm)1]$ configurations which are assigned to the ND3a and ND3b bands, [00,02] assigned to ND8 , $[0(\pm)1, 0(+)1]$ assigned to ND6a and ND6b, the two highest spin state of $[0(+)1, 0(-)1]$ assigned to ND7 and finally $[0(+)1, 02]$ assigned to ND9. Note especially that with more particles in the high-j $1g_{9/2}$ orbitals, the terminating sequences become more down-sloping.

If we proceed in the same way, for the configurations with one proton hole in $1f_{7/2}$, the signature partner configurations $[11, 0(+)1]$ are assigned to TB1a and TB1b, and the [11,02] configurations are in good agreement with the observed TB2a and TB2b bands. Finally the [1(+)2,02] configuration agrees well with observed WD4 structure.

Except for the ground state band ND1 and the highest spin state in the ND3 and ND7 configurations, the differences in the lower panels of Fig. 5.10 and 5.11 are fairly constant for the different structures and fall within $\pm$ 1 MeV. The highest spin states of ND3 and ND7 are both formed with the third fp neutron in the $1f_{5/2,m=3/2}$ orbital, see Fig. 5.5. The discrepancy suggests that the $1f_{5/2}$ neutron subshell is at a too high energy with present parameters (κ and μ). Because $I^{\pi} = 14^{-}$ and 17^{+} are the highest spin values with can be formed with $1f_{7/2}$ hole and one and two $1g_{9/2}$ particles, respectively, the possibility that these states should be assigned to another configuration appears excluded because more proton holes in $1f_{7/2}$ would lead to a higher energy. It appears that ND2 and ND4 might rather be described as vibrations while ND5 is not a regular structure. Therefore, the

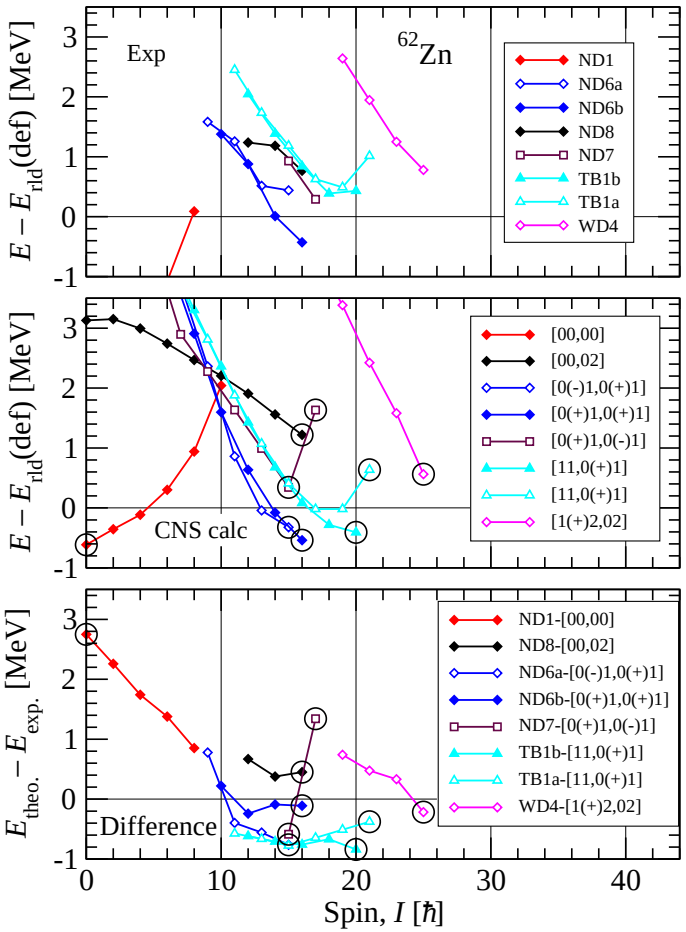

Figure 5.10: Comparison between experimentally observed structures and cranked Nilsson-Strutinsky predictions for observed positive-parity bands with $I_{max} \lesssim 25\hbar$ in ^{62}Zn. The top panel illustrates experimental energies relative to the rotating liquid drop (rld) energy, where the bands are labelled according to Fig. 4.1. The middle panel shows the selected calculated bands. The bottom panel shows the energy difference between the predictions and the observations. Signature α= 0 is represented by filled symbols, and $\alpha = 1$ by open symbols.

structures ND2, ND4, and ND5 are not assigned to any configurations.

Figure 5.12 is analogous to Fig. 5.10 but here the illustrated bands cor-

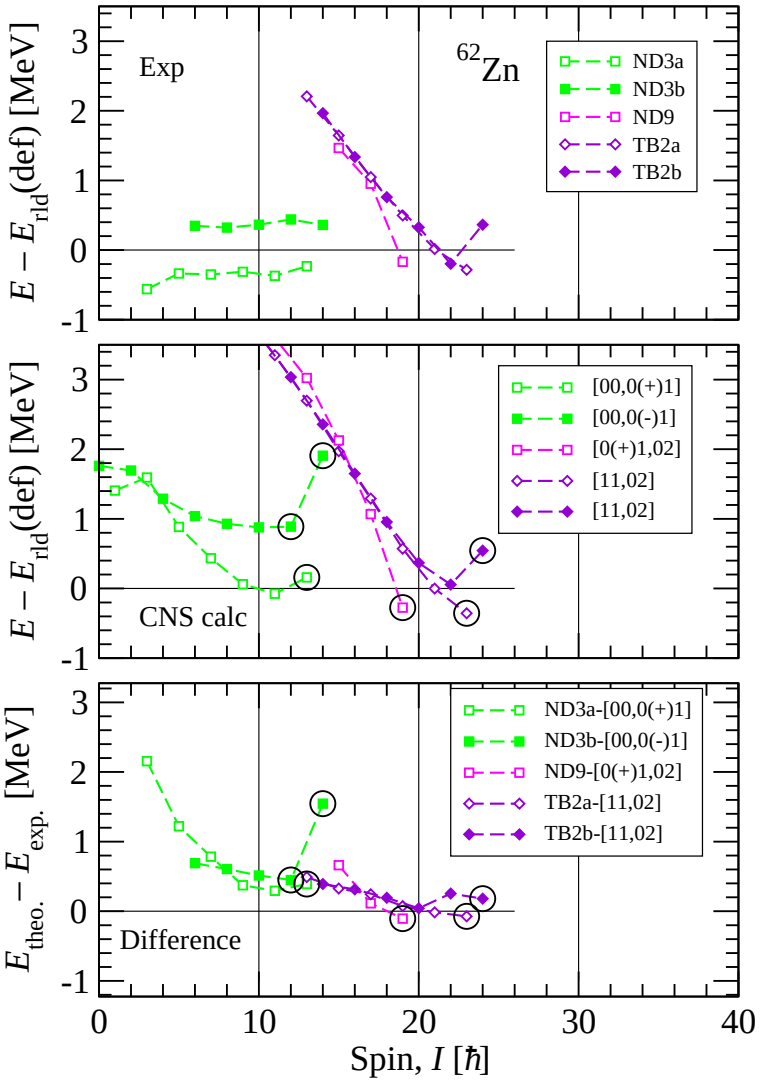

Figure 5.11: Same as Fig. 5.10 but here illustrated for observed bands with negative parity.

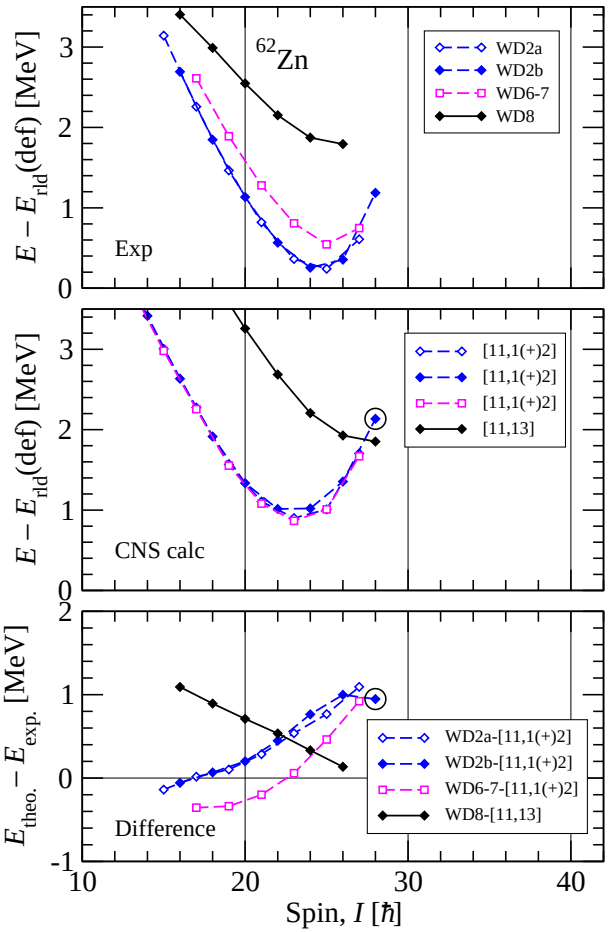

Figure 5.12: Same as Fig. 5.10 but with the assigned configurations of one proton and one neutron hole in the $1f_{7/2}$ shell for both positive and negative parity high-spin deformed structures with maximum spin $\leq 30\hbar$ with firm spin-parity assignments. Solid (dashed) lines represent positive (negative) parity.

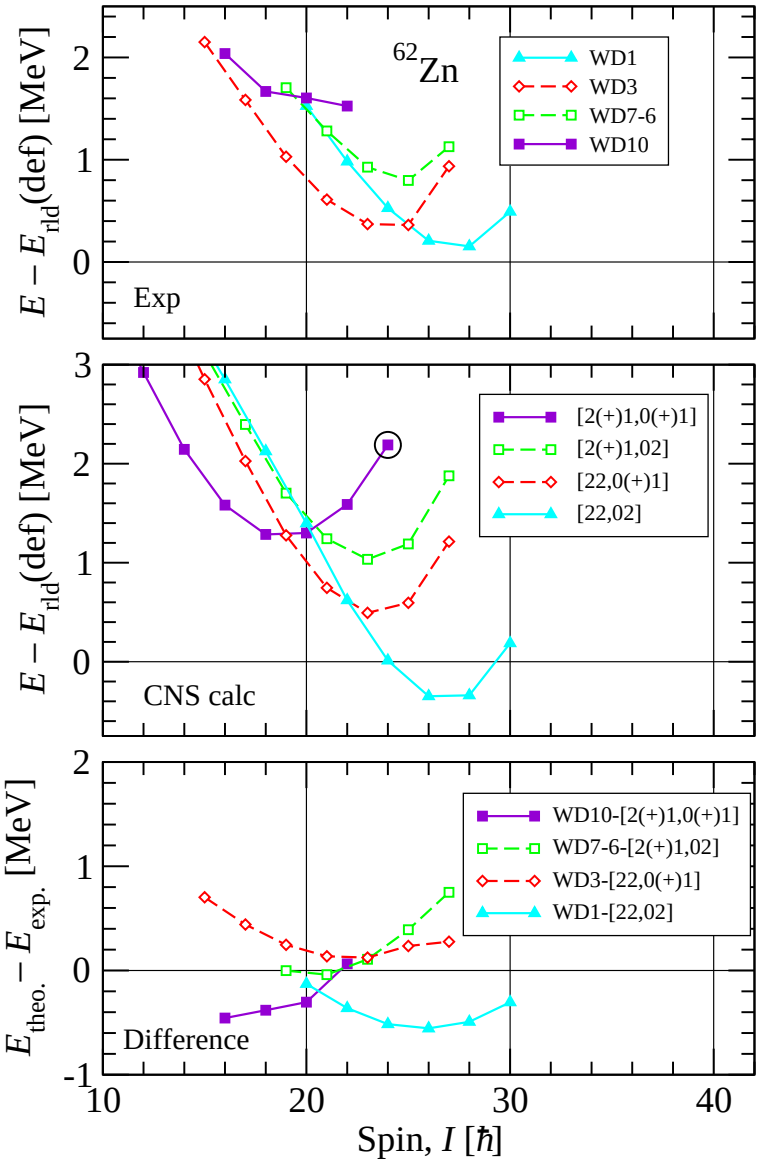

Figure 5.13: Same as Fig.5.12 but here shown for bands with two proton holes in the $1f_{7/2}$ shell.

respond to one proton and one neutron hole in $1f_{7/2}$, for both positive and negative parity high-spin structures with maximum spin $I \leq 30\hbar$. Figure 5.13 is analogous to Fig. 5.12 but with two proton holes in $1f_{7/2}$.

With two proton holes, the configuration can be described as built from a ${}^{60}_{29}\mathrm{Cu}_{31}$ core

$$\pi(f_{7/2})^{-2}(fp)^2(g_{9/2})^1\nu(fp)^2(g_{9/2})^1 \tag{5.20}$$

with one proton and one neutron outside, see Fig. 5.3. Low energy bands are obtained if the proton and neutron are placed either in the $\alpha = +1/2(fp)_2$ orbital or in the $\alpha = -1/2(g_{9/2})_1$ orbital, which thus leads to four combinations which can all be assigned to observed bands (see Fig. 5.13); WD10 with both particles in the fp orbitals, WD3 and WD7-6 with one particle lifted to $1g_{9/2}$, and WD1 with both particles in $1g_{9/2}$. The WD7-6 band is a mixture of WD6 and WD7. Experimentally these two bands come close together at spin $I^\pi = 21^-$ with an energy difference of 20 keV. To make these band energies smooth, WD6 and WD7 bands should cross at $I \approx 21^-$. In this process, two smooth undisturbed bands with new energies called WD6-7 and WD7-6 are formed. The WD6-7 band is assigned to $[11, 1(+)2]$ and the WD7-6 band is assigned to $[2(+)1, 02]$.

With one neutron hole and one proton hole in $1f_{7/2}$, two pairs of signature partner bands are obtained which are degenerate in a large spin range. The WD2a and WD2b bands (Fig. 5.12) can be assigned to the $[11, 1(+)2]$ bands with $I_{max} = 27^-, 28^-$, while the WD6-7 band can be assigned to the other odd-spin $[11, 1(+)2]$ configuration. There will be an interaction between the $[11, 1(+)2]$ configurations with the same signature which is not included in the CNS formalism. This interaction would lead to a splitting in general agreement with what is seen for the observed WD2a and WD6-7 bands. The WD8 band can be assigned to the [11,13] band, which is lowest in energy at high spin, [see Fig. 5.7, panel (a)]. The energy differences between experimental and calculated, for all these bands are within ± 1 MeV, in the lower panel of Fig. 5.12 and 5.13, but the different slopes are somewhat problematic.

The spin and parity assignments are uncertain experimentally for the structures WD9 and WD11. Therefore, it is difficult to assign configurations to them.

Figure 5.14 is analogous to Fig. 5.12 but for superdeformed band structures with firm spin-parity assignments. The bands SD1 and SD2 are in good agreement with the $[22, 2(-)3]$ and $[22, 2(+)3]$ signature partner configurations. SD3 fits with the [22,24] configuration, but it is then strange that the [22,22] band is not observed. More details on these band assignments are reported in [48]. Note that there is a small error in the moment of inertia calculation in [48] which affects both the calculated energies and the reference energies which are subtracted. This leads to differences of a few

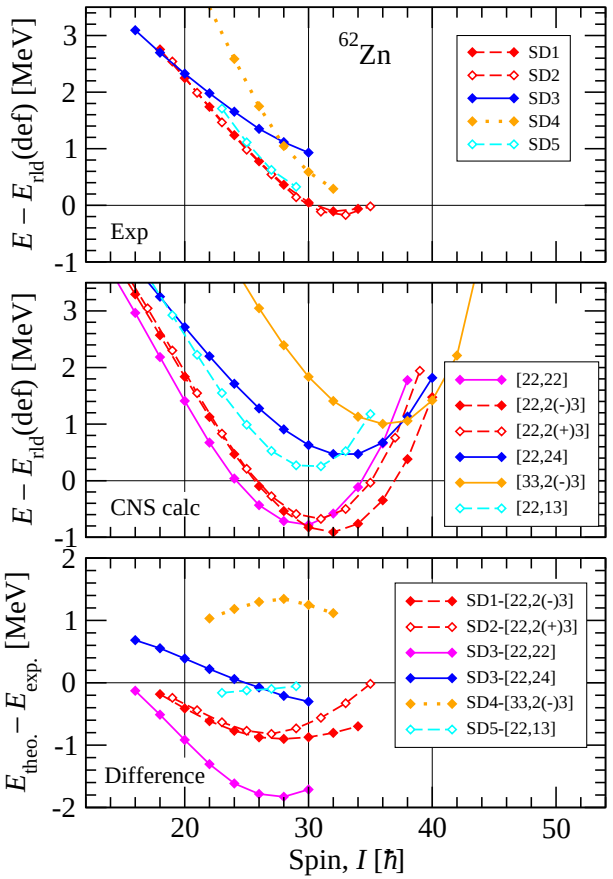

Figure 5.14: Same as Fig. 5.12 but here shown for superdeformed band structures with $I_{max} \lesssim 35\hbar$.

hundred keV in the energies of the $E - E_{rld}$ plots, but it does not change any conclusions about configuration assignments.

The new SD4 band spin is uncertain and the parity is undetermined. However, there are some possible configuration assignments. It is clearly seen from Fig. 5.9 that the calculated π[22] bands with one or two neutron holes in the $1f_{7/2}$ shell have a smaller slope, while the bands with one particle in $1h_{11/2}$ have a larger slope compared to the experimentally observed SD4 band in Fig. 5.13 top panel. The calculated bands with three proton holes in the $1f_{7/2}$ shell and three protons in the $1g_{9/2}$ shell have a better slope than these two cases discussed above. The corresponding

$[33, 2(-)3]$ band is compared with the observed SD4 band, resulting in $\sim$ 1.4 MeV energy difference in the lower panel of Fig. 5.14. In conclusion the configuration of SD4 is unclear. The new SD5 band might be assigned to the negative signature partner of [22,13] configuration.

5.4.2 Deformations

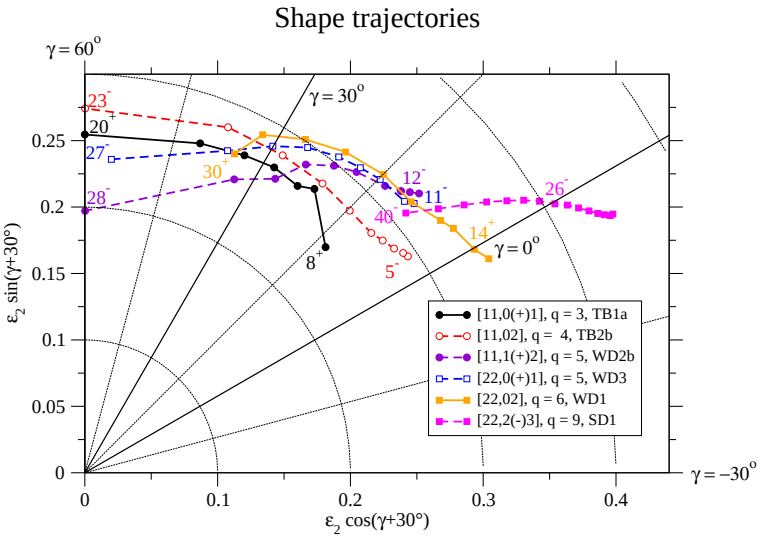

Figure 5.15: The calculated shape evolution of selected configurations assigned to the bands TB1b, TB2a, WD2b, WD3, WD1 and SD1 in the (ε_2, γ) plane. The $\gamma = 0°$ axis describes prolate shape with collective rotation and $\gamma = 60°$ oblate shape with rotation around the symmetry axis. Intermediate values of γ, i.e., $0° < \gamma < 60°$ signify triaxial shapes.

The calculated shape trajectories for the selection of bands, assigned to TB1b, TB2a, WD2b, WD3, WD1 and SD1, are illustrated in Fig. 5.15. It can be seen that the bands in general change their shapes gradually, starting close to $\gamma = 0°$ (prolate) and approaching $\gamma = 60°$ (oblate) at $I = I_{max}$.

It was shown in [14] that the number of particles excited into $1g_{9/2}$, together with the number of particle-hole excitations across the $N = Z = 28$ shell gap, is strongly correlated to the calculated deformation at a low or intermediate spin value. The trend is seen in Fig. 5.15, which includes structures ranging from two particles in $1g_{9/2}$ subshell, $[11, 0(+)1]$, to five particles, $[22, 2(-)3]$. Simultaneously the number of particle-hole excitations from the $1f_{7/2}$ subshell ranges from one to four. To see the combined

effect, the variable q was introduced [14] as the sum of particle-hole excitations and particles in the $g_{9/2}$ subshell according to $q = p_1 + p_2 + n_1 + n_2$. In the figure the illustrated structures range from $q = 3$ up to $q = 9$, and the average deformation increases with q as suggested earlier.

5.5 New Nilsson Parameters

The large number of observed rotational bands in the $A \sim 60$ mass region is investigated. To obtain a good agreement between experimental and calculated bands, using the current standard set of Nilsson parameters. A new set of Nilsson parameters is determined, which is based on the comparison between theoretical predictions from Cranked Nilsson Strutinsky calculations and existing experimental data.

5.6 Description of Selected Bands in Different Nuclei

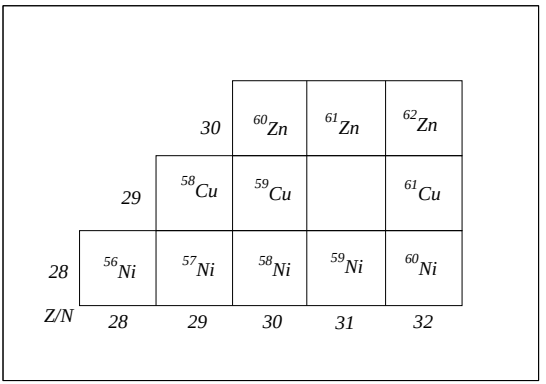

Figure 5.16: Selected isotopes for finding out the new Nilsson parameters in the $A \sim 60$ mass region.

The involved nuclei are the Ni, Cu and Zn isotopes, which are shown in Fig. 5.16. The bands selected from these isotopes have confirmed spin, parity and well established configuration assignments in the spin range $I \geq 15\hbar$. The selected bands from different nuclei in the $A \sim 60$ mass region are summarized in Table 5.4.

Table 5.4: Table of selected bands for finding out the new Nilsson parameter set, from different nuclei in the $A \sim 60$ mass region.

Nucleus	Bands	$[q_1, q_2]$	Maximum Spin, parity, signature	Configuration
^{56}Ni	SD2	[4,1]	$I^\pi = 17, \alpha = 1$	[2(+)1,20], [20,2(+)1][1]
^{57}Ni	SD1	[4,2]	$I^\pi = 47/2^-, \alpha = 1$	[2(+)1,21]
^{58}Ni	D3a, 3b	[3,1]	$I^\pi = 18^-, 15^-, \alpha = 0, 1$	[20,11]
	Q1a, 1b	[3,2]	$I^\pi = 22^+, 23^+, \alpha = 0, 1$	[2(+)1,11]
	Q2a, 2b	[3,2]	$I^\pi = 20^+, 21^+, \alpha = 0, 1$	[2(-)1,11]
	Q3	[4,2]	$I^\pi = 22^+, \alpha = 0$	[20,22], [2(+)1,2(+)1][1]
	B1, B2	[4,3]	$I^\pi = 31^-, \alpha = 1$	[2(+)1,22], [31,22]
	B3	[5,3]	$I^\pi = 32^-, \alpha = 0$	[31,22]
^{59}Ni	Band 1	[2,1]	$I^\pi = 37/2^+, \alpha = +1/2$	[20,01]
	Band 2	[2,2]	$I^\pi = 43/2^-, \alpha = -1/2$	[2(+)1,01]
^{60}Ni	M2	[1,2]	$I^\pi = 17^+, \alpha = 0, 1$	[11,0(+)1], [1(+)0,02]
	WD1a, b	[2,1]	$I^\pi = 18^-, 19^-, \alpha = 0, 1$	[20,0(∓)1]
	WD2	[3,2],[2,3]	$I^\pi = 23^+, \alpha = 1$	[31,0(+)1], [2(+)1,02][2]
	WD3	[2,2]	$I^\pi = 22^+, \alpha = 0$	[2(+)1,0(+)1], [20,02][3]
^{58}Cu	SD	[4,2]	$I^\pi = 23^+, \alpha = 1$	[21,21]
^{59}Cu	Band 5	[4,3]	$I^\pi = 57/2^+, \alpha = +1/2$	[21,22]
	6A, 6B	[4,2]	$I^\pi = 49/2^-, 47/2^-, \alpha = +1/2, -1/2$	[21,2(∓)1]
	8A, 8B	[3,2]	$I^\pi = 47/2^-, 49/2^-, \alpha = -1/2, +1/2$	[21,11]
^{61}Cu	D3a, D3b	[1,2]	$I^\pi = 37/2^-, 35/2^-, \alpha = +1/2$, -1/2	[1(+)1,0(+)1]
	Q4	[2,3]	$I^\pi = 53/2^+, \alpha = +1/2$	[21,02]
	Q5	[4,3]	$I^\pi = 53/2^+, \alpha = +1/2$	[21,22]
	Q7a, b	[3,3]	$I^\pi = 53/2^+, 55/2^+, \alpha = 1/2, -1/2$	[21,1(∓)2]
^{60}Zn	SD	[4,4]	$I^\pi = 30^+, \alpha = 0$	[22,22]
^{61}Zn	SD1	[4,5]	$I^\pi = 57/2^+, \alpha = +1/2$	[22,23]
	ND5a, b	[1,2]	$I^\pi = 37/2^-, 39/2^-, \alpha = +1/2, -1/2$	[11,01]
	SD2A, B	[3,4]	$I^\pi = 55/2^-, 57/2^-, \alpha = +1/2, -1/2$	[22,12]
	SD2C	[4,4]	$I^\pi = 55/2^-, \alpha = -1/2$	[22,2(-)2]
^{62}Zn	SD1, SD2	[3,5]	$I^\pi = 34^-, 35^-, \alpha = 0, 1$	[22,13]
	SD3	[4,6]	$I^\pi = 30^+, \alpha = 0$	[22,24]
	SD5	[4,5]	$I^\pi = (29^-), \alpha = 1$	[22,2(+)3]
	WD1	[2,4]	$I^\pi = 30^+, \alpha = 0$	[22,02]
	WD2a, b	[2,3]	$I^\pi = 27^-, 28^-, \alpha = 1, 0$	[11,1(+)2]
	WD3	[2,3]	$I^\pi = 27^-, \alpha = 1$	[22,0(+)1],[2(+)1,02][3]
	WD4	[1,4]	$I^\pi = 25^+, \alpha = 1$	[1(+)2,02]
	WD5	[3,4]	$I^\pi = 31^+, \alpha = 1$	[22,1(+)2]
	WD6-7	[2,3]	$I^\pi = 27^-, \alpha = 1$	[11,1(+)2]
	WD7-6	[2,3]	$I^\pi = 27^-, \alpha = 1$	[2(+)1,02],[22,0(+)1][3]
	TB1a, 1b	[1,2]	$I^\pi = 20^+, 21^+, \alpha = 0, 1$	[11,0(+)1]
	TB2a, 2b	[1,3]	$I^\pi = 23^-, 24^-, \alpha = 1, 0$	[11,02]
	ND9	[0,3]	$I^\pi = 19^-, \alpha = 1$	[0(+)1,02]
	ND8	[0,2]	$I^\pi = 16^+, \alpha = 0$	[00,02]
	ND7	[0,2]	$I^\pi = 17^+, \alpha = 1$	[0(+)1,0(−)1]
	ND6a, b	[0,2]	$I^\pi = 15, 16^+, \alpha = 1, 0$	[0(±)1,0(−)1]

[1]Possible alternative.
[2]Possible configuration for WD2 with negative parity.
[3]With new parameters these bands are rather assigned to these configurations.

5.6.1 Ni- Isotopes

^{56}Ni [66]

The experimental SD2 band is best described by the calculated [2(+)1,20] configuration, i.e two proton and two neutron holes in the $1f_{7/2}$ subshell, with three nucleons excited into the upper fp shell and one proton in a $1g_{9/2}$ orbital. The calculated band [20,2(+)1] has a similar behavior as [2(+)1,20]. Therefore, the experimental band can be assigned to either of these calculated bands or rather to a mixture of them [67].

^{57}Ni [68]

The two lowest calculated bands with one $1g_{9/2}$ proton and one $1g_{9/2}$ neutron but with no constraint on the number of $1f_{7/2}$ holes are shown in Fig. 5.17(a). These bands come close together at $I \simeq 21.5\hbar$ with an energy difference of only 200 keV. For spin values $I \simeq 15\hbar$, the lowest band is dominated by the [2(+)1,21] configuration and the highest band by [31,21] while the configurations are interchanged at $I \simeq 21.5\hbar$, see Fig. 5.3. In order to form two smooth non-interacting bands, the energies of the lower and higher bands have been increased and decreased, respectively, by 0.03, 0.10 and 0.03 MeV at $I = 19.5, 21.5$ and $23.5\hbar$. It is now possible to form two non-interacting bands of [2(+)1,21] and [31,21] character which cross near at $I = 21.5\hbar$, see Fig. 5.17(b). The calculated band [2(+)1,21] with

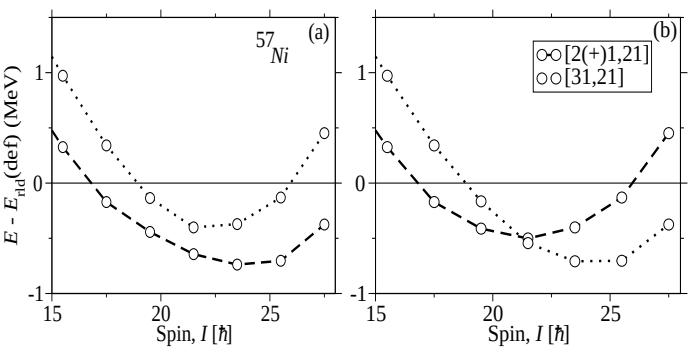

Figure 5.17: The two lowest calculated $\pi(g_{9/2})^1\nu(g_{9/2})^1$ bands for ^{57}Ni [68] as they come out from the diagonalization are shown in the left side panel. A band crossing has been inferred in the right side panel. The resulting non-interacting [2(+)1,21] band is assigned to the observed SD1 band.

undisturbed energies has been assigned to the experimentally observed band SD1, which appears to stay pure in its observed spin range. The

observed band SD2 has undetermined parity and there is no convincing interpretation of it with standard parameters.

^{58}Ni [13, 32]

The low-spin dipole structures D3a and D3b, the high-spin quadrupole dominated structures Q1a, Q1b, Q2a, Q2b and Q3 and the three superdeformed structures B1, B2 and B3 (referred to as Q4, Q5 and Q6 in [13]) have been selected. The remaining dipole structures, D1a, D1b and D2, are observed to too low-spin ($\leq 15\hbar$) values and have not been selected. Among the three superdeformed structures, the B3 structure has been assigned to a pure [31,22] configuration. More details on the assignments for the bands B1 and B2, are already discussed in [32]. A short summary is given below based on Fig. 5.18.

All three experimental bands B1, B2 and B3 are shown in the upper panel of Fig. 5.18, whereas the corresponding calculated bands are shown in the middle panel and the differences between observed and calculated bands are shown in the lower panel. As per previous results [32], the observed B1 and B2 bands approach each other around spin $I = 25\hbar$ and then diverge as a function of spin. Within the interaction region, the observed bands can be described as a mixture of two unsmooth bands. To make these observed band energies smooth, the B1 and B2 bands should cross at $I \approx 25\hbar$. In a similar way as discussed for the calculated bands of ^{57}Ni above, two smooth non-interacting bands with new energies called B1a and B2a are formed, which are shown in the upper panel of Fig. 5.18. In a similar way, the possible assigned calculated $\pi(g_{9/2})^1\nu(g_{9/2})^2$ negative signature bands have a close approach with in an energy difference of 200 keV at $I \approx 21\hbar$. In an analogous way to the crossing of the experimental bands, these two calculated bands are crossed at $I \approx 21\hbar$, forming two non-interacting bands [32]. The pure configuration assignments for the observed bands are shown in the middle panel of Fig. 5.18. For a best fit between experimental and calculated bands, the calculated bands should also cross at the same spin state $I \approx 25\hbar$. To achieve this, one should lower the position of the proton $1f_{7/2}$ subshell by $\approx$ 0.5 MeV with respect to the standard CNS parameters [32].

^{59}Ni [69]

Band 1 and Band 2 are observed to high spin with confirmed spin and parity assignments and they have been assigned to pure theoretical configurations [20,01] and [2(+)1,01], respectively. The observed bands Band 3 and Band 4 are not connected, therefore they have not been selected.

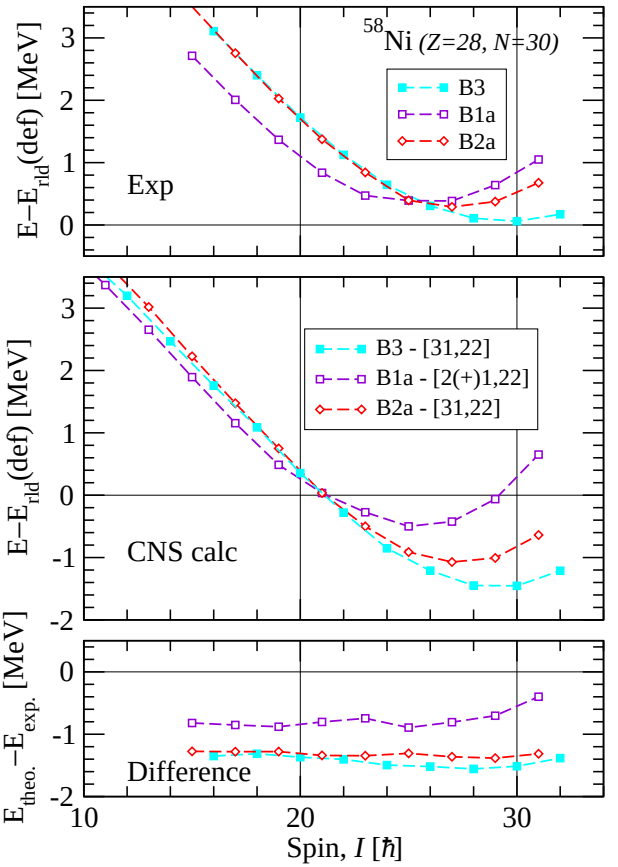

Figure 5.18: Non-interacting configuration assignment for the B1 and B2 bands in ^{58}Ni using standard parameters. In addition the B3 band is shown.

^{60}Ni [31]

The bands M1, M3 and M4 are observed only to low-spin values and have not been selected. The bands M2, WD1a, WD1b, WD2 and WD3 are well established both experimentally and theoretically. All these five bands have been selected.

5.6.2 Cu- Isotopes

^{58}Cu [70]

The experimentally observed high-spin superdeformed band SD1 is in good agreement with the calculated band [21,21] and has been selected.

^{59}Cu [14]

The well established high-spin bands 5, 6A, 6B and 8A, 8B have been selected. The high-spin bands 4a, b, 7a, b and 10 with uncertain configuration assignments have not been selected.

^{61}Cu [15]

The bands Q4, Q5, Q7 are selected because all these are in good agreement with CNS calculations. The dipole bands are observed to too low-spin values and have not been selected. The bands Q6, Q8 and Q9 are observed with tentative spins. Therefore they have not been selected.

5.6.3 Zn- Isotopes

^{60}Zn [18]

The experimental values for the SD band in ^{60}Zn are in good agreement with the calculated values for the [22,22] band. This band has been selected.

^{61}Zn [16]

The bands SD1, ND5a and ND5b are well established experimentally and in good agreement with the calculated [22,23] and signature partners of the [11,01] bands, respectively. Therefore, these bands have been selected. The bands ND7, ND10, SD3A and SD3B are observed with tentative spin and parities and have not been selected. The three superdeformed bands SD2A, SD2B and SD2C are also observed with tentative spin and parities. They have been assigned to the possible configurations with either one or two neutron $1f_{7/2}$ holes. Analogous bands but with one additional $1g_{9/2}$ neutron (SD1, SD2 and SD5) have been observed in ^{62}Zn [48] with confirmed spin and parity. By knowing the relative spins of these bands in ^{61}Zn (SD2A, SD2B and SD2C) and ^{62}Zn (SD1, SD2 and SD5), one can fix the spin values of the SD2A, SD2B, and SD2C bands in ^{61}Zn, (see section 5.7.2). Therefore, these three SD bands have been selected and are listed in table 5.4.

^{62}Zn [17, 48]

The superdeformed bands SD1, SD2, SD3 and SD5, well-deformed bands from WD1 to WD7-6 and normally deformed bands ND3, ND6, ND7, ND8 and ND9 are observed with confirmed spin and parity values and are in good agreement with the theoretical predictions. All these bands have been selected. The bands SD4 and WD9 were not selected because their parities were determined tentatively. Experimentally observed irregular bands ND2, ND4 and ND5 have not been considered.

The bands SD1, SD2 and SD5 have been assigned to the [22,13] and [22,23] configurations [48], but the specific configuration assignments of each band is uncertain, see Refs. [17, 48]. One may note that these bands are formed from the [22,12] and [22,22] configurations assigned to the SD2A, B and C bands in ^{61}Zn by adding a third $g_{9/2}$ neutron. Therefore, in a similar way as the signature degenerate bands in ^{61}Zn, SD2A and SD2B, are assigned to the configuration with one $f_{7/2}$ hole, [22,12], the signature degenerate bands in ^{62}Zn, SD1 and SD2, are now assigned to the [22,13] configuration (this choice is different from the choice in Ref. [48]). The band SD5 is then assigned to the [22,2(+)3] configuration.

5.7 Effective Alignment: Analysing the Selected Band Structures

The effective alignment method [71, 72, 73, 74] is used to analyze the relative properties of the rotational bands in neighbouring nuclei. With this method the consistency of the spin, parity and theoretical configuration assignments of the existing experimental bands can be investigated. The effective alignment, which is the difference of spin values at constant rotational frequency measures the contribution from different Nilsson orbitals. Generally it is denoted as i_{eff}. The main contribution to i_{eff} comes from the alignment of the orbital which is being occupied when going from the A to the $(A+1)$ nucleus but differences in deformation and pairing etc. between these two nuclei will also affect i_{eff}. To extract the effective alignments, one should know the relative spins. Alternatively, this approach can be used to find out experimentally unknown spins.

In case of superdeformed bands, the two compared bands maintain an almost constant difference of the equilibrium deformation between the bands over a wide range of rotational frequency. This gives an i_{eff} which is predominately defined by the alignment properties of the particle in the

single-particle orbital by which the two bands differ.

In the case of smooth terminating bands, the sudden shape change at the terminating state makes the i_{eff} value different from the alignment of the single-particle orbital. The transition depopulating the terminating state links the states having the largest difference in equilibrium deformation within the band, where the terminating state has $\gamma = 60^\circ$ and the state with $I_{max} - 2$ has typically $\gamma \sim 30^\circ$ and a larger ϵ_2 than the terminating state. Thus from the i_{eff} approach one can also measure how well theory describes the shape changes close to termination also.

The effective alignment between bands A and B, which is calculated at constant rotational frequency $\hbar\omega$, is defined [71, 72, 73, 74] as $i_{eff}^{A,B}(\omega) = I_B(\omega) - I_A(\omega)$. Band A in the lighter nucleus is taken as a reference. In a standard plot of spin I vs. transition energy E_γ (or rotational frequency $\omega \approx E_\gamma/2$) an increase of I with particle number will be seen, if the added particle has a positive spin contribution. This is illustrated in Fig. 5.19,

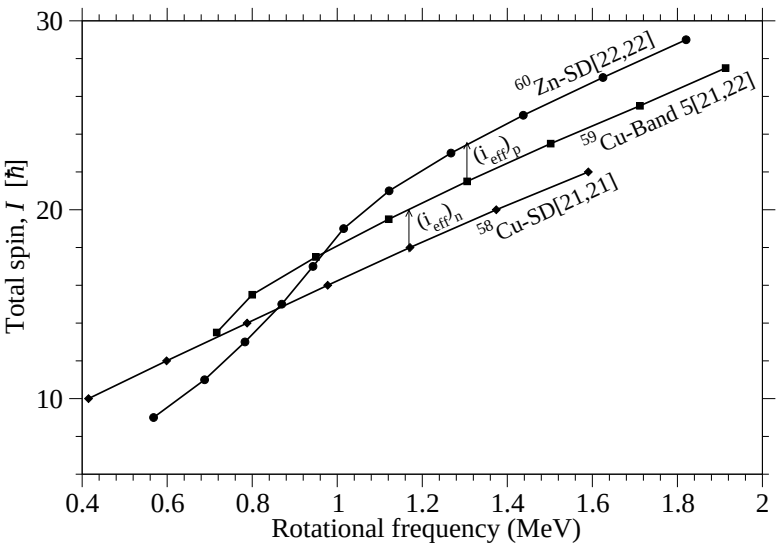

Figure 5.19: The total spin I vs. rotational frequency ω for the experimental bands SD[21,21] from ^{58}Cu, Band 5[21,22] from ^{59}Cu and SD[22,22] from ^{60}Zn. The value of i_{eff} is illustrated at specific ω-values.

which shows the total spin vs. rotational frequency for the observed bands SD [21,21] in ^{58}Cu, Band 5 [21,22] in ^{59}Cu and SD [22,22] in ^{60}Zn. From this figure, one can measure the i_{eff} of the second $g_{9/2}$ neutron and pro-

ton. For rotational frequencies below 1 MeV, the three bands in the figure align differently, indicating different pairing correlations [18, 75]. These correlations disappear at high spin values, leading to an almost constant i_{eff} for $\hbar\omega \geq 1$ MeV, see Figs. 5.20 and 5.21.

5.7.1 Theoretical Effective Alignments

In order to describe the effective alignment theoretically, we first consider the properties of the calculated orbitals close to the Fermi surface at some deformation. Besides the alignment brought in for building angular momentum, an additional particle or hole can also polarize the nuclear shape. This will lead to a change in the moment of inertia. The calculated alignments are, especially for high-j orbitals like, the $g_{9/2}$ orbital, not sensitive to parameter changes, while the single-particle energies are very sensitive.

In the computer codes, there are two methods to calculate the effective alignments: in the first method i_{eff} is calculated with equidistant ω_i-values in the range of ω where the two bands overlap, while in the second method, i_{eff} is calculated at the frequencies corresponding to the transition energies in band B with the additional requirement that also the reference band A is known in that frequency range. The calculated effective alignments of the bands, which differ in occupation of one orbital, are then compared with experiment.

5.7.2 Experimental and Calculated Effective Alignments

In the present study the main interest in is the analysis of the contribution/alignment of a proton and neutron $g_{9/2}$ particle, where the nucleus goes from mass number A to $(A+1)$ either by adding a proton or a neutron $g_{9/2}$ particle.

Configurations differing in occupation of one $g_{9/2}$ neutron

The experimental effective alignments calculated between pairs of bands of neighbouring nuclei, which differ by the occupation of only one extra $g_{9/2}$ neutron added in the $N+1$ isotope compared with the N isotope, are shown in Fig. 5.20(a). One can notice from Fig. 5.20(a), that the largest spin contribution comes as expected from the first $g_{9/2}$ neutron particle, a somewhat smaller contribution from the second $g_{9/2}$ neutron particle, etc. Except for the two cases ^{62}Zn-SD1[22,13] / ^{61}Zn-SD2A[22,12] and ^{62}Zn-SD2[22,13] / ^{61}Zn-SD2B[22,12], all other alignments are consistent with each other. The reason for these alignment inconsistencies may lie in the tentatively assigned spin values of the SD2a and SD2b bands in ^{61}Zn. We

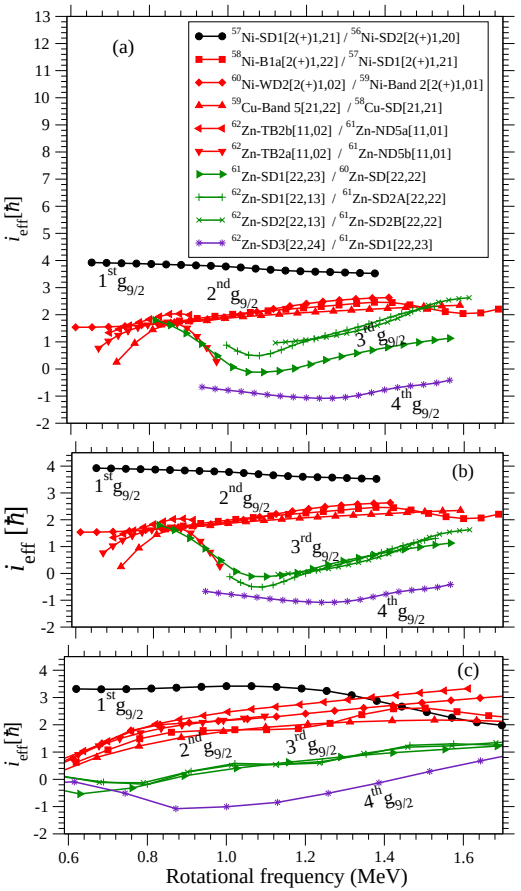

Figure 5.20: (a) Effective alignments, i_{eff}, extracted from the experimental bands of different neighbouring nuclei in the $A \sim 60$ mass region with $g_{9/2}$ neutron particle excitation. (b) Same as panel (a) but with $1\hbar$ spin increment of the SD2A and SD2B bands in ^{61}Zn. (c) Calculated effective alignments for the neutron $g_{9/2}$ particle excitation. Note that the alternative [2(+)1,02] configuration has been tested for the WD2 band in ^{60}Ni. See text for details.

may compare the alignments of these two bands with the well established ^{61}Zn-SD1[22,23] / ^{60}Zn-SD[22,22] pair alignment, which also involves the third $g_{9/2}$ neutron excitation. It is clear that the alignments of the ^{62}Zn-SD1[22,13] / ^{61}Zn-SD2A[22,12] and ^{62}Zn-SD2[22,13] / ^{61}Zn-SD2B[22,12] bands should be decreased by $1\hbar$. These alignments are lowered by $1\hbar$, if

the spin values of the SD2A and SD2B in ^{61}Zn are increased by $1\hbar$. With this spin increment, the state at the bottom of band SD2A which is fed by the 1942 keV transition is assigned as $I^{\pi} = 35/2^{-}$. To make the excitation energy consistent with those observed for the other SD bands in ^{61}Zn and in neighbouring nuclei, the tentatively assigned energy must be increased by approximately 2 MeV. Thus in the comparisons below, the excitation energy for the $35/2^{-}$ state is fixed at 15.266 MeV. Since the band SD2C is connected to the band SD2B, for consistency, the used spin and excitation energy for its lowest state are modified to $I^{\pi} = 31/2^{-}$ and $E_{exc} = 14.044$ MeV, respectively. Effective alignments with these new spin values of SD2A and SD2B bands in ^{61}Zn are shown in Fig. 5.20(b), where the alignments for the third $g_{9/2}$ neutron lie on top of each other.

Calculated effective alignments between the bands from the different neighbouring nuclei which differ by the occupation of one extra $g_{9/2}$ neutron particle are shown in Fig. 5.20(c). Because of the uncertain values of single-particle energies and spin contributions in regions where virtual crossings are removed, these contributions are typically uncertain by $\pm 0.2\hbar$. There is a general consistency between experiment and calculations although the calculated values are more spread than the experimental ones. This is partly caused by the fact that they are shown in a larger spin range with larger shape changes but it is also surprising that the experimental values are so well collected. Note that the results confirm the configuration assignment [22,24] to the SD3 band in ^{62}Zn, which was unclear in Ref. [48].

Configurations differing in occupation of one $g_{9/2}$ proton

Since the $N = 4, g_{9/2}$ orbital is rather pure, the i_{eff} values are expected to be similar for protons and neutrons. The experimental effective alignments for the proton $1g_{9/2}$ particle excitation between two bands from neigbouring nuclei are shown in Fig. 5.21(a). Calculated effective alignments are shown in Fig. 5.21(b). Since the observed bands involve only one or two $1g_{9/2}$ protons, i_{eff} values are only calculated for the first and second $1g_{9/2}$ orbitals. Except for the experimental alignment of the ^{59}Cu-Band 5[21,22] / ^{58}Ni-Q3[20,22] pair, all other alignments are in general agreement with the calculated alignments. The experimental alignment of the ^{59}Cu-Band 5[21,22] / ^{58}Ni-Q3[20,22] pair has a strange behaviour, which is mainly down-sloping contrary to the other two pairs of alignments with first $1g_{9/2}$ proton excitation. Because there is no doubt about the [21,22] assignment for band 5 in ^{59}Cu, this suggests that the [20,22] assignment for ^{58}Ni band should be investigated.

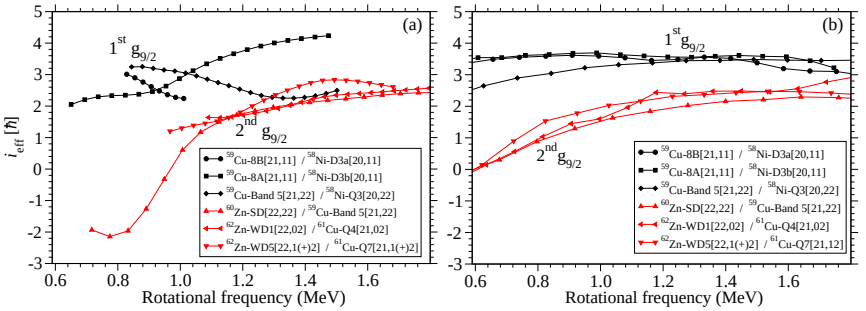

Figure 5.21: (a) Effective alignments, i_{eff}, extracted from the experimental bands of different neighbouring nuclei in the $A \sim 60$ mass region with an additional $g_{9/2}$ proton particle. (b) Calculated effective alignments for proton $g_{9/2}$ particle excitation.

5.7.3 Contribution to $\langle j_x \rangle$ Values from Individual $g_{9/2}$ Orbitals

It is instructive to compare the calculated effective alignments with the pure single-particle $\langle j_x \rangle$ contributions. Unlike in the $A \sim 150$ region [72, 76] , the effects from deformation changes (mainly bands which come close to terminating states) can be rather large in the $A \sim 60$ region. Therefore, two deformation values have been chosen: $\varepsilon_2 = 0.226$ as illustration for the bands which terminate in the I = 25 - 30$\hbar$ spin range and $\epsilon_2 = 0.410$ for superdeformed bands.

Orbitals at a smaller deformation: $\epsilon_2 = 0.226, \gamma = 15^\circ$ and $\epsilon_4 = 0.010$ **:**

The individual $\langle j_x \rangle >$ contributions of the $N = 4$ $g_{9/2}$ orbitals at the deformation $\varepsilon_2 = 0.226, \gamma = 15^\circ$ and ϵ_4 = 0.010 are shown in Fig. 5.22 (a). The single-particle energies at the same deformation are shown in Fig. 5.22 (b). At this deformation, crossings are formed in Fig. 5.22 (b), between the $1g_{9/2}$ orbitals at small frequencies and they are then numbered at a larger frequency as $1^{st}g_{9/2}$, $2^{nd}g_{9/2}$ etc. The corresponding alignments are shown in Fig. 5.22 (a). The first $g_{9/2}$ orbital is most strongly aligned coming close to its maximum value, 4.5 $\hbar$, at high frequencies, the second comes close to 3.5 $\hbar$ etc. A similar situation occurs for $N = 4$ proton $g_{9/2}$ orbitals. The $\langle j_x \rangle >$ contributions of the $N = 4$, $g_{9/2}$ neutrons and protons are consistent with the experimental and calculated $g_{9/2}$ neutron effective alignments shown in Figs. 5.20 and 5.21.

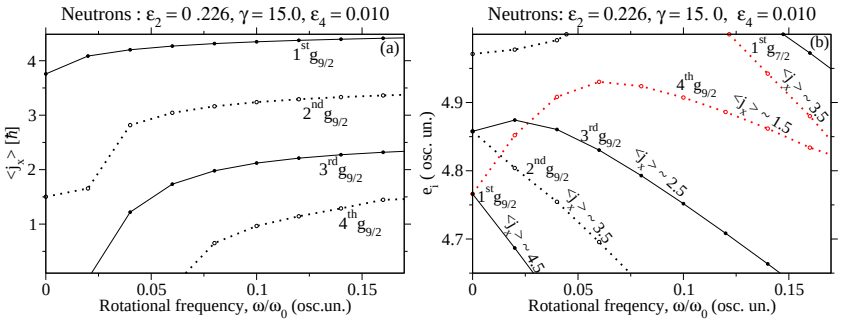

Figure 5.22: (a) Single neutron $g_{9/2} < j_x >$ contributions at the deformation ϵ_2 = 0.226, $\gamma = 15^\circ$ and $\epsilon_4 = 0.010$. (b) Single-particle $g_{9/2}$ energies at $\epsilon_2 = 0.226, \gamma = 15^\circ$ and $\epsilon_4 = 0.010$. The $N = 4, g_{9/2}$ proton orbital align in a very similar way.

Orbitals at larger deformation: $\epsilon_2 = 0.41, \gamma = 0^\circ$ and $\epsilon_4 = 0.04$**:**

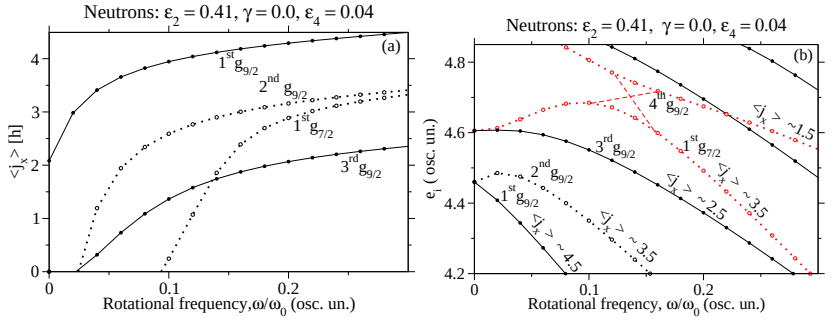

Figure 5.23: (a) Single neutron $g_{9/2}$ $\langle j_x \rangle$ contributions at the deformation ϵ_2 = 0.41, $\gamma = 0^\circ$ and $\epsilon_4 = 0.04$. (b) Single-particle energies at $\epsilon_2 = 0.41, \gamma = 0^\circ$ and $\epsilon_4 = 0.04$. The 4^{th} and 5^{th} $N = 4$ orbitals are labelled according to their main amplitudes at high frequencies.

Figures 5.23 (a) and (b) are analogous to Figs. 5.22 (a) and (b), but at a larger deformation ϵ_2 = 0.41, $\gamma = 0^\circ$ and $\epsilon_4 = 0.04$. In this case no crossings are formed at low frequencies which means that the orbitals keep their order for all frequencies. At the rotational frequency ω/ω_0 = 0.14, the 4th $N = 4, g_{9/2}$ orbital interacts with the lowest $N = 4, g_{7/2}$ orbital. At this interaction, the orbitals exchange character as, marked out by the red lines in Fig. 5.23 (b). For higher rotational frequencies, the fourth $N = 4$ orbital will be of $g_{7/2}$ character coming close to an alignment of 3.5 $\hbar$, see Fig. 5.23

(a).

5.8 Problems in the Configuration Assignments for Some Observed Bands in Ni Isotopes

5.8.1 ^{58}Ni- Q3 Band

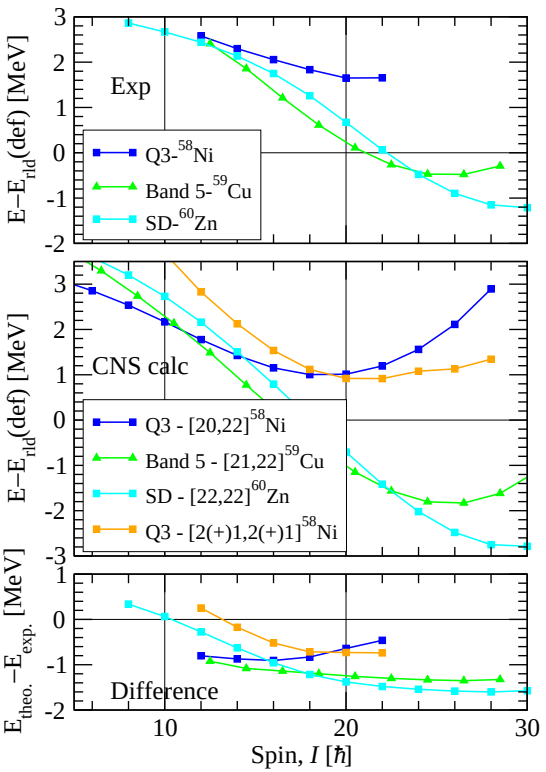

Figure 5.24: Configuration assignment for the Q3 band in ^{58}Ni using standard parameters.

As already mentioned in section 5.6.1, the previously assigned configuration [20,22] [13] for Q3 band might be wrong. Fig. 5.24 is drawn to get more clarification on this configuration assignment. The comparison of the [20,22] configuration assigned to the Q3 band with previously well established configurations, band 5 -[21,22] from ^{59}Cu and SD - [22,22] from ^{60}Zn, is shown in Fig. 5.24. The three experimental bands are drawn in the

upper panel of Fig. 5.24, while the calculated bands with identical neutron configurations but zero, one and two $g_{9/2}$ protons are drawn in the middle panel with the difference between calculations and experiment in the lower panel. With this interpretation, the difference in the lower panel of Fig. 5.24 for the Q3 -[20,22] band from ^{58}Ni has a different trend than the other two bands.

This suggests that we should look for another interpretation of the Q3 band in ^{58}Ni. Because of its positive parity, the configuration must have two $g_{9/2}$ particles. Instead of having two $g_{9/2}$ neutrons, the other best possible configuration is with one proton and one neutron $g_{9/2}$ particle. This calculated band, [2(+)1,2(+)1] (orange color), is also drawn in the middle panel and the corresponding difference in the lower panel of Fig. 5.24. The difference line of the Q3 - [2(+)1,2(+)1] band has a similar trend as the other two difference lines, band 5 - [21,22] in ^{59}Cu and SD - [22,22] in ^{60}Zn, in the lower panel of Fig. 5.24. Therefore, we may conclude that the [2(+)1,2(+)1] configuration appears to be a better interpretation of the Q3 band, while we cannot rule out a [20,22] interpretation. With the present parameters the difference lines of band 5 - [21,22] in ^{59}Cu and SD - [22,22] in ^{60}Zn in the lower panel of Fig. 5.24 are separated by 0.2 or 0.3 MeV in the high spin range. This suggests that the proton $g_{9/2}$ gap should be increased by $\approx$ 0.2 or 0.3 MeV.

5.8.2 ^{60}Ni - WD2 Band

The observed band WD2 in ^{60}Ni has been assigned to the [31,0(+)1] configuration [31] with positive parity. If we compare the energy difference between experimental and calculations for this band with the energy differences of any one of the WD1a and WD1b bands assigned to the configurations [20,0(+)1] and [20,0(-)1], there a big difference, see lower panel of Fig. 5.25. Furthermore, there are indications [15, 65] that the neutron $N = 40$ gap should be decreased and the 28 gap should be increased which will make this difference even larger, (see section 5.9). The big difference puts doubt on the assignment and we might think about some other possible interpretation of the WD2 band. The parity assignment of the observed band WD2 is based on a weak 2456 keV dipole transition [31]. There are weak arguments that this transition is $M1$ (mixed with $E2$) but it can certainly not be excluded that it is $E1$, i.e., one can argue that the parity of WD2 band might be negative. If we consider the parity of the WD2 band as negative, then the best possible configuration is [2(+)1,02] with three particles in $g_{9/2}$ orbitals.
The experimental bands WD1a, WD1b and WD2 are shown in the upper

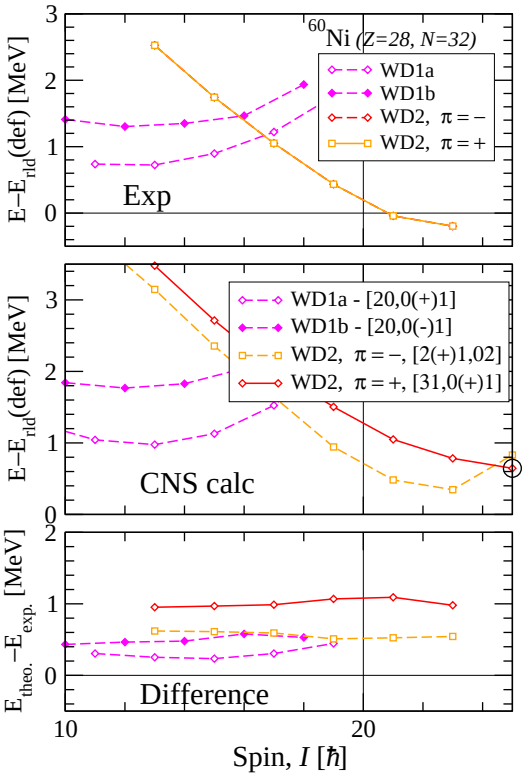

Figure 5.25: Configuration assignment for the WD2 band in ^{60}Ni using standard parameters.

panel of Fig. 5.25. The possible assigned configurations are shown in middle panel while the differences between observed and calculated are shown in the lower panel. The best possible assignment is then [2(+)1,02] assuming $\pi = -$ for WD2, where it turns out that the difference between calculations and experiment is clearly smaller than for the [31,0(+)1] assignment, assuming $\pi = +$ for WD2. With a [2(+)1,02] assignment for the WD2 band in ^{60}Ni, we can calculate the effective alignment relative to band 2 in ^{59}Ni assigned as [2(+)1,01]. The experimental and calculated effective alignments of the ^{60}Ni-WD2[2(+)1,02] / ^{59}Ni-band 2[2(+)1,01] pair are consistent with the other alignments pairs, where the 2^{nd} $g_{9/2}$ neutron particle is involved, see Fig. 5.20(a). This gives further evidence that the parity of WD2 is negative.

5.9 Quest for New Nilsson Parameters

5.9.1 Energy Shifts for the Different High-j Shells

For all selected bands, which are mentioned in Table 5.4, Cranked Nilsson Strutinsky calculations with standard parameters were performed. The *N* = *4*, $1g_{9/2}$ and *N* = *3*, $1f_{7/2}$ orbitals are more pure than the other orbitals ($1f_{5/2}$, $2p_{3/2}$ and $2p_{1/2}$), and the position of the corresponding subshells gives a direct measure of gaps at $Z, N = 28$ and 40. Therefore, we introduce four simple cases, from which one can find out revised energy gaps and thereby determine the new Nilsson parameters:
Case 1. $1g_{9/2}$ neutron particle excitation
Case 2. $1g_{9/2}$ proton particle excitation
Case 3. $1f_{7/2}$ neutron hole excitation
Case 4. $1f_{7/2}$ proton hole excitation
All these four cases are examined, considering the bands in neighbouring nuclei whose configurations are identical except for the particle in the $1g_{9/2}$ or $1f_{7/2}$ orbital. In addition bands in the same nucleus which differ by a $1f_{7/2} \rightarrow fp$ or a $fp \rightarrow 1g_{9/2}$ excitation are considered as a measure of the position of the $1f_{7/2}$ and $1g_{9/2}$ subshell, respectively. Then however these values are more uncertain because they are also sensitive to the position of the fp orbitals.
Let us exemplify with the B1a band in ^{58}Ni which is assigned to the [2(+)1,22] configuration. These observed and calculated bands are shown relative to the rotating liquid drop energy in Fig. 5.18 with the difference between experimental and calculations in the lower panel. In the $I \sim 17 - 23\hbar$ spin range, the average value of the difference is $-$ 0.8 MeV. The SD1 band in ^{57}Ni has the same configuration except for the second $g_{9/2}$ neutron, i.e., [2(+)1,21]. The difference between calculations and experiment in this case is $-$1.1 MeV in the same spin range as for the ^{58}Ni band, $I \sim$ 17 - 23$\hbar$. The spin range is chosen because the ^{57}Ni band is only observed to $I = 23.5\hbar$ while the results become more uncertain for lower spin values where pairing correlations start to become important. Comparing the differences for ^{58}Ni and ^{57}Ni, $-$ 0.8 MeV and $-$ 1.1 MeV, we can conclude that the differences would be the same if the energy cost when occupying the second $g_{9/2}$ neutron orbital is 0.3 MeV lower suggesting that the $1g_{9/2}$ subshell should be lowered by approximately 0.3 MeV. This method is used to fix the single-particle energies because absolute energies depend on a lot of factors which are not well known, e.g. the parameters of the rotating liquid drop model, while relative energies are to first order directly related to the position of the single-particle orbitals.
This is analogous to methods used for superdeformed bands where it is often advantageous to consider relative properties rather than absolute prop-

erties [74]. The same method as for the two bands in ^{57}Ni and ^{58}Ni is now applied to other bands in neighbouring nuclei. Table 5.5 includes the cases where identical configurations except for one high-j particle are observed in a common high-spin range.
In a similar way, the configurations in the same nucleus which differ by one high-j particle are listed in Table 5.6. Most values in the Tables can be read out from published $E - E_{rld}$ plots, see Refs. [13, 14, 15, 16, 17, 18, 31, 32, 48, 66, 68, 69, 70], but to be consistent, we have carried out calculations for all the bands in Table 5.4.

In general, the differences in Tables 5.5 and 5.6 are rather similar for one specific excitation. Combining Tables 5.5 and 5.6, it is found that the average energy difference for the $1g_{9/2}$ neutron particle excitation is 0.5 MeV, $1g_{9/2}$ proton particle excitation is $-$ 0.45 MeV, $1f_{7/2}$ neutron hole excitation is $-$0.4 MeV and, for $1f_{7/2}$ proton hole excitation is $-$ 0.2 MeV. These values suggest that the $1g_{9/2}$ neutron orbital should be lowered by $\approx$ 0.5 MeV, the $1g_{9/2}$ proton orbital should be lifted by $\approx$ 0.5 MeV, the $1f_{7/2}$ neutron shell should be lowered by $\approx$ 0.4 MeV and $1f_{7/2}$ proton shell should be lowered by $\approx$ 0.2 MeV. It turns out that to get the differences in Tables 5.5 and 5.6 close to zero, somewhat larger energy shifts must be performed. This is due to the effects of the $l \cdot s$ and l^2- terms which are generally stronger at spherical than at deformed shapes. Furthermore, the shells are not pure at the deformations and rotational frequencies considered here and the Strutinsky renormalization tends to counteract the shifts.

Table 5.5: Energy differences between the bands of different neighbouring nuclei are calculated for four different cases, (1) $1g_{9/2}$ neutron particle excitation (2) $1g_{9/2}$ proton particle excitation (3) $1f_{7/2}$ neutron hole excitation (4) $1f_{7/2}$ proton hole excitation. Calculations have been performed with the standard Nilsson parameters.

	Nuclei	Spin range $\hbar$	Band 1 - Band 2	Energies[1] (MeV)	Diff. (MeV)
$\nu(g_{9/2})$					
	^{57}Ni - ^{58}Ni	$\sim$ 17 - 23	SD1[2(+)1,21] - [2(+)1,22]B1a	$-1.1, -0.8$	0.3
	^{58}Cu - ^{59}Cu	$\sim$ 17 - 23	SD[21,21] - [21,22]Band 5	$-1.7, -1.3$	0.4
	^{60}Zn - ^{61}Zn	$\sim$ 22 - 30	SD[22,22] - [22,23]SD1	$-1.6, -0.8$	0.8
	^{61}Zn - ^{62}Zn	$\sim$ 14 - 20	ND5b[11,01] - [11,02]TB2	-0.3, 0.2	0.5
		$\sim$ 22 - 28	SD1[22,23] - [22,24]SD3	$-0.8, -0.3$	0.5
			Avg.diff		0.5
$\pi(g_{9/2})$					
	^{58}Ni - ^{59}Cu	$\sim$ 14 - 18	D3a[20,11] - [21,11]8B	0.3, -0.8	-1.1
	^{59}Cu - ^{60}Zn	$\sim$ 22 - 28	Band 5[21,22] - [22,22]SD	$-1.3, -1.6$	-0.3
	^{61}Cu - ^{62}Zn	$\sim$ 20 - 26	Q4[21,02] - [22,02]WD1	0.0, -0.5	-0.5
		$\sim$ 20 - 27	Q7b[21,1(+)2] - [22,1(+)2]WD5	0.0, -1.0	-1.0
			Avg.diff		-0.7
$\nu(f_{7/2})$					
	^{59}Ni - ^{58}Ni	$\sim$ 15 - 19	Band 1[20,01] - [20,11]D3a	0.5, 0.3	-0.2
		$\sim$ 14 - 22	Band 2[2(+)1,01] - [2(+)1,11]Q1b	0.1, -0.2	-0.3
	^{59}Cu - ^{58}Cu	$\sim$ 16 - 24	8A[21,11] - [21,21]SD	$-1.0, -1.4$	-0.4
			Avg.diff		-0.3
$\pi(f_{7/2})$					
	^{62}Zn - ^{61}Cu	$\sim$ 18 - 24	TB2[11,02] - [21,02]Q4	0.2, -0.2	0.0
	^{59}Cu - ^{58}Ni	$\sim$ 22 - 28	Band 5[21,22] - [31,22]B3	$-1.3, -1.5$	-0.2
			Avg.diff		-0.1

[1]The comparable values between the two bands are taken from the differences between the experimental and calculated band energies which are drawn from $E - E_{rld}$ plots.

Table 5.6: Energy differences between the bands within the same nucleus are calculated for four different cases, (a) $1g_{9/2}$ neutron particle excitation (b) $1g_{9/2}$ proton particle excitation (c) $1f_{7/2}$ neutron hole excitation (d) $1f_{7/2}$ proton hole excitation. Calculations have been performed with standard parameters. The extra particle in $1g_{9/2}$ ($1f_{7/2}$) is excited from (to) the (fp) orbitals.

	Nucleus	Spin range $\hbar$	Band 1 - Band 2	Energies (MeV)	Diff. (MeV)
$\nu(g_{9/2})$					
	^{59}Cu	$\sim$ 18 - 24	6A[21,21] - [21,22]Band 5	$-1.3, -1.3$	0.0
	^{62}Zn	$\sim$ 12 - 18	TB1a[11,01] - [11,02]TB2b	-0.7, 0.2	0.9
			Avg.diff		0.45
$\pi(g_{9/2})$					
	^{58}Ni	$\sim$ 16 - 18	D3a,b[20,11] - [21,11]Q1,2	0.3, -0.1	-0.4
	^{59}Ni	$\sim$ 14 - 18	Band 1[20,01] - [21,01]Band 2,3	0.6, 0.1	-0.5
	^{62}Zn	$\sim$ 19 - 23	TB2[11,02] - [1(+)2,02]WD4	0.1, 0.5	0.4
		$\sim$ 14 - 16	ND8[00,02] - [01,02]ND9	0.4, 0.4	0.0
		$\sim$ 19 - 23	WD7-6[21,02] - [22,02]WD1	0.1, -0.4	-0.5
			Avg.diff		-0.2
$\nu(f_{7/2})$					
	^{61}Cu	$\sim$ 20 - 26	Q7a[21,12] - [21,22]Q5	0.0, -0.4	-0.4
		$\sim$ 20 - 26	Q4[21,02] - [21,12]Q7a	0.0, -0.1	-0.1
	^{62}Zn	$\sim$ 23 - 29	SD2[22,13] - [22,2(+)3]SD5	0.0, -0.8	-0.8
		$\sim$ 20 - 30	WD1[22,02] - [22,12]WD5	$-0.4, -1.0$	-0.6
			Avg.diff		-0.5
$\pi(f_{7/2})$					
	^{62}Zn	$\sim$ 12 - 16	ND6[01,01] - [11,01]TB1	$-0.1, -0.6$	-0.5
		$\sim$ 15 - 19	ND9[01,02] - [11,02]TB2	0.0, 0.0	0.0
		$\sim$ 20 - 25	WD4[12,02] - [22,02]]WD1	0.3, -0.5	-0.8
	^{58}Ni	$\sim$ 20 - 25	B1[21,22] - [31,22]B3	$-0.8, -1.2$	-0.4
			Avg.diff		-0.42

5.9.2 A General Method to Shift a j-shell With a Spin-Orbit Partner

The energy levels of the spherical modified oscillator potential in closed form is given by

$$E(Nlj) = \hbar\omega_0 \left[(N+3/2) - \kappa \left\{ \begin{array}{c} l \\ -(l+1) \end{array} \right\} - \mu' \left[l\,(l+1) - N\,(N+3)\,/2 \right] \right] \quad \text{for} \left\{ \begin{array}{l} j = l+1/2 \\ j = l-1/2 \end{array} \right\} \tag{5.21}$$

In this equation [77], κ is the strength of the $l \cdot s$- term and $\mu^{'}(=\kappa\mu)$ is the strength of the l^2- term. These parameters are generally chosen to have different values for the different $N-$shells. If we want to fit the energy values of the different subshells to experiment it is desirable to be able to move *one* subshell relative to the other subshells. This becomes possible if κ and μ are allowed to depend not only on *N* but also on l. However the $\langle l^2 \rangle_N$ = $N(N+3)/2$ term in Eq. 5.21 was introduced [77] to preserve the center-of- mass of each *N*- shell independent of μ. This is an important property, i.e., if one subshell is lowered by some energy, the other subshells will be lifted in energy. When shifting a single-particle orbital by having κ and μ l-dependent, there are more parameters than needed so it can be done in different ways. An easy way applicable for an orbital with an $l \cdot s$ partner, described in the Master thesis of B.G. Carlsson [78], is illustrated here.

First, the two partners are moved so that they get the desired distance by changing their $l \cdot s$ coupling strength, i.e changing their κ_{Nl}. In the second step, one of the orbitals is brought back to its original position preserving the distance between the orbitals by changing the l^2- coupling , i.e., the $\mu^{'}_{Nl}$ parameter. In the third step, all orbitals in the *N*-shell are moved by the same energy so that the center of mass is brought back to its original position. This procedure is illustrated in Fig. 5.26, where the $1f_{5/2}$ subshell is lowered by 0.07 $\hbar\omega_0$ relative to the other $N = 3$ subshells. With the standard parameters for protons, $\kappa = 0.09, \mu' = 0.027$, the $N = 3$ orbitals will have the positions shown in the second column of Fig. 5.26, where the different steps are illustrated in the consecutive columns. According to Eq. 5.21, the distance between two signature partners is $\kappa\,(2l+1)\,\hbar\omega_0$, i.e., κ should be decreased by 0.01 for these $N = 3$ orbitals. The $1f_{7/2}$ orbital should be moved back by 0.03 $\hbar\omega_0$ to get its original position. The $\mu^{'}$ term in Eq. 5.21 takes the value -$\mu^{'}_{33}(3 \cdot 4 - 3 \cdot 6/2) = -3\mu'_{33}\hbar\omega_0$ in this specific case, i.e., $\delta(\mu^{'}_{33}) = 0.01$. Finally, the center of mass should be brought back to its original position. Because the three $f_{5/2}$ orbitals have been lowered

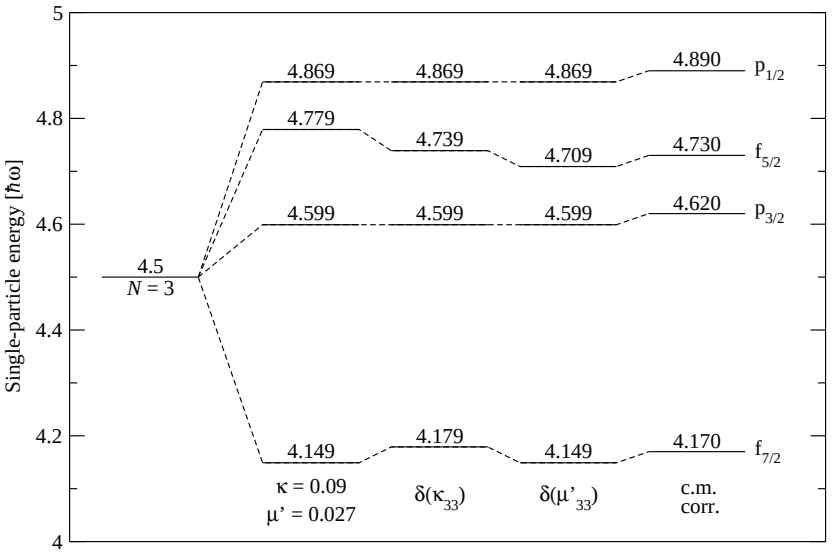

Figure 5.26: Illustration of how to shift a subshell using κ and μ parameters which depend on N and l, i.e, κ_{Nl} and μ_{Nl}. In this case, the $1f_{5/2}$ subshell is lowered by 0.07 $h\omega_0$, which is achieved by choosing $\delta(\kappa_{33}) = 0.01$ and $\delta(\mu_{33}) = 0.01$. The energy of each orbital is specified in each case. See text for details.

by 0.07 $\hbar\omega$, each of the ten $N = 3$ orbital is lifted by $0.07 \cdot 3/10 = 0.021\ \hbar\omega_0$. This results in the orbitals shown to the right in Fig. 5.26.

5.9.3 New Nilsson Parameters for N = 4 Shell

As already mentioned in section 5.9.1, for a better agreement between experimental and calculated band energies, from Tables 5.5 and 5.6, it is estimated that the $N = 4$ proton and neutron $1g_{9/2}$ orbitals should be shifted by a value which is somewhat larger than 0.5 MeV in different directions. After performing some tests, it appears that 0.7 MeV $\approx 0.066\hbar\omega_0$ (for the $A \sim 60$ mass region) is an appropriate value where the neutron $1g_{9/2}$ sub-

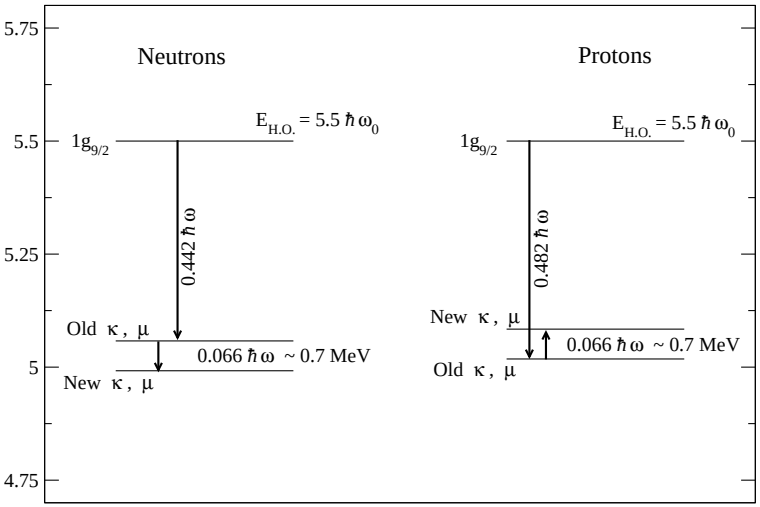

Figure 5.27: Energy shifts from the harmonic oscillator energy ($E_{H.O} = 5.5\hbar\omega_0$, which are calculated with old and new energy positions of $N = 4$, $1g_{9/2}$ orbital are drawn for neutrons (left side) and protons (right side). See text for details.

shell is shifted downwards while the proton $1g_{9/2}$ subshell is shifted upwards. The energy shifts from the harmonic oscillator value, 5.5 $\hbar\omega_0$, which results from the standard parameters and the additional shifts are shown in Fig. 5.27. The shells are expanded or compressed if the strength of the $l \cdot s$ and l^2 terms, i.e., the κ and $\mu^{'}$ parameters, are multiplied by the same factor. The factors which are calculated to get the new energy shifts of $N = 4, 1g_{9/2}$ neutron and proton subshells are 1.149 and 0.863, respectively. These factors have been used to obtain the new Nilsson parameters for the $N = 4$ shell. The old and new Nilsson parameters for $N = 4$ protons and neutrons are given in Table 5.7.

Table 5.7: Old and new Nilsson parameters for $N = 4$ shell protons and neutrons.

$N = 4$	κ_{old}	${\mu'}_{old}$	κ_{new}	${\mu'}_{new}$
Protons	0.065	0.0370	0.0560	0.0319
Neutrons	0.070	0.0273	0.0804	0.0313

5.9.4 New Nilsson Parameters for $N = 3$ shell

Lowering of $1f_{5/2}$ orbital by $\approx$ 1 MeV with respect to the $2p_{3/2}$ orbital

As discussed in [17], the disagreement of the high energy states 17^+ and 14^- of ND7 and ND3b bands in ^{62}Zn (see the lower panel energy differences of figures 22 and 23 in ^{62}Zn [17]) suggests that the $1f_{5/2}$ neutron shell should be lowered relative to the $2p_{3/2}$ shell. Furthermore, the wrong signature splitting in the ND4 band in ^{61}Zn [16] suggests a similar lowering of the $1f_{5/2}$ shell for the protons. It appears that a lowering of the $1f_{5/2}$ subshell by approximately 1 MeV ($\sim 0.1\ \hbar\omega_0$) will cure the problems. Following the same procedure as explained in section 5.9.2, the corresponding changes in κ and $\mu^{'}$ are $\delta\kappa_{33} = \frac{0.1}{0.07} \times -0.01 = -0.0142$ and $\delta\mu^{'}_{33} = \frac{0.1}{0.07} \times 0.01 = 0.0142$ (scaling has been done with respect to the $\delta\kappa$ and $\delta\mu^{'}$ values, which are calculated for the lowering of $1f_{5/2}$ orbital by 0.07 $\hbar\omega_0$, see section 5.9.2).

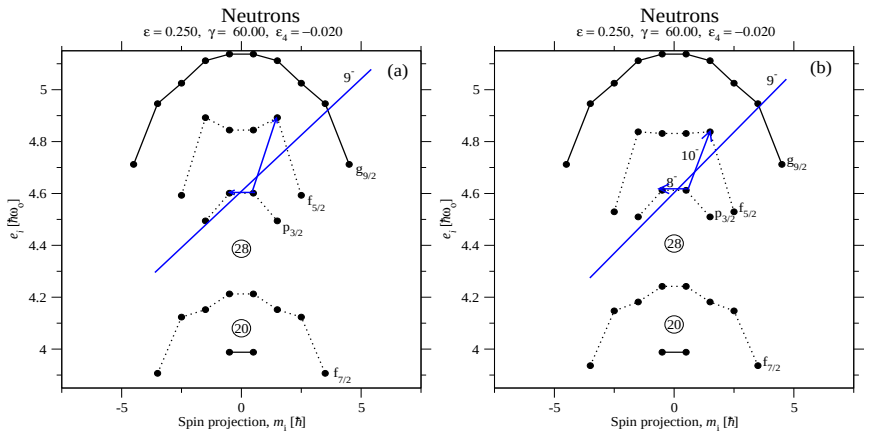

Figure 5.28: Sloping Fermi surface diagram at a deformation typical for the terminating [01,01] states of ^{62}Zn with (a) standard parameters (b) new κ and $\mu^{'}$ parameters for $N = 3$ shell, where the $f_{5/2}$ subshell has been lowered by 0.1 $\hbar\omega_0$ relative to the other $j-$ shells. The straight lines in both figures representing to define a favoured neutron state with $I_n = 9^-$, with signature $\alpha_n = 1$. For an aligned neutron configuration with $\alpha_n = 0$ signature, the $m_i = 1/2$ neutron can be moved either to the $m_i = -1/2$ orbital or to the $m_i = 3/2$ orbital as illustrated by arrows. See text for details.

With these changes in κ and $\mu^{'}$ for $N = 3$ shell, the sloping Fermi surface diagram at a deformation typical for the fully aligned states of the

[01,01] configuration of ^{62}Zn is shown in Fig. 5.28(b), whereas Fig. 5.28(a) is drawn with the standard parameters, i.e., it is identical to the right hand side panel of Fig. 5.5, (see more details in Ref. [17]). In both Figs. 5.28(a) and 5.28(b) , the favoured aligned states are formed in configurations defined by straight-line, or close-to-straight-line Fermi surfaces and these states are referred to as optimal states ($I_n = 9^-$, with $\alpha_n = 1$ signature). For an aligned neutron configuration with $\alpha_n = 0$ signature, the $m_i = 1/2$ neutron can be moved either to the $m_i = -1/2$ orbital or to the $m_i = 3/2$ orbital as illustrated by arrows. If we compare Fig. 5.28(b) with Fig. 5.28(a), it is noticed that the gap between $1f_{5/2}$ and $2p_{3/2}$ is decreased. With this new gap, the distance from the Fermi line to the $m_i = 3/2$ orbital which is occupied in the $I_n = 10^-$ state is comparatively smaller than the distance shown in Fig. 5.28(a) [17]. Therefore, this $I_n = 10^-$ state which is used to build the mentioned 17^+ and 14^- states in ^{62}Zn, is about as favoured as the $I_n = 8^-$ state.

Increase of the $Z = N = 28$ gap by $\sim$ 1 MeV

The average difference values of case 3 and case 4, from Tables 5.5 and 5.6, indicate that the $1f_{7/2}$ proton and neutron subshells should be lowered or the *Z = 28* and *N = 28* gaps should both be increased by $\sim$ 0.5 MeV. This is illustrated in Fig. 5.29, where the $1f_{7/2}$ orbital is lowered by $a = 0.5$ MeV. This is combined with the lowering of the $1f_{5/2}$ subshell by 1 MeV, i.e., 2a MeV, as discussed in the previous section. Because there are four $1f_{7/2}$ and three $1f_{5/2}$ Nilsson orbitals with in total ten $N = 3$ Nilsson orbitals, the center of mass is put back to its original position if all these ten orbitals from $N = 3$ shell are lifted by $X = a = 0.5$ MeV. This leads to no shift in the absolute position of the $1f_{7/2}$ subshell, see Fig. 5.29, which is true for any value of a. It also means that the average distance between the ($1f_{5/2}$, $2p_{3/2}$) shells and the $1f_{7/2}$ shell is more or less the same as before or rather somewhat smaller because there are more $1f_{5/2}$ than $2p_{3/2}$ orbitals.

For a real 28 gap increment, the $1f_{7/2}$ orbital must be lowered more, say $\sim$ 1 MeV. If both the $1f_{7/2}$ and the $1f_{5/2}$ shells are lowered by 1 MeV, it means that the spin-orbit splitting between these two shells is unchanged and it is not necessary to introduce any l-dependence for κ.
If μ' is independent on l, and the $l = 3$ $1f_{5/2}$ and $1f_{7/2}$ shells are lowered by 1 MeV $\approx 0.1\ \hbar\omega_0$ relative to the $l = 1$ $2p_{1/2}$ and $2p_{3/2}$ shells then the μ' term from Eq.5.21, which is $\mu'[l(l+1)-N(N+3)/2]$ gives $3\delta\mu^{'} - (-7\delta\mu^{'}) = 0.1\hbar\omega_0$ which leads to $\delta\mu^{'} = 0.01$. The old and new level energies of $1f_{7/2}$, $1f_{5/2}$, $2p_{3/2}$ and $2p_{1/2}$ from $N = 3$ and $1g_{9/2}$ from $N = 4$ shells are shown in Fig. 5.30. The old and new Nilsson parameters for $N = 3$ protons and neutrons are given in Table 5.8.

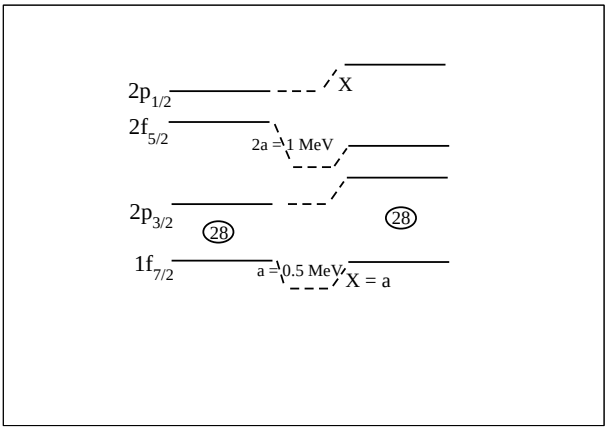

Figure 5.29: Illustration of level gap changes with $1f_{5/2}$ lowered by 1 MeV and $1f_{7/2}$ lowered (28 gap increment) by 0.5 MeV. See text for details.

Table 5.8: Old and new Nilsson parameters for $N = 3$ shell protons and neutrons.

$N = 3$	κ_{old}	μ'_{old}	κ_{new}	μ'_{new}
Protons	0.090	0.0270	0.090	0.0370
Neutrons	0.090	0.0225	0.090	0.0325

5.10 Results with the New Nilsson Parameters

By using the new Nilsson parameters for $N = 3$ and 4 shells listed in Tables 5.7 and 5.8, the results from Tables 5.5 and 5.6 are modified as shown in Tables 5.9 and 5.10.

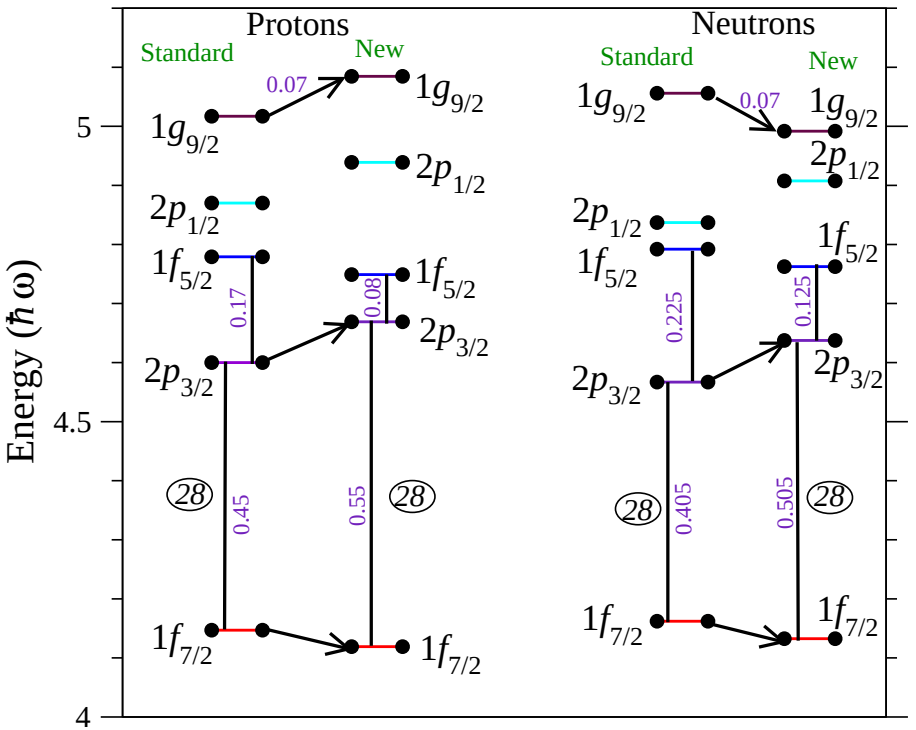

Figure 5.30: For $N = 3$, the $l = 3$ shells have been lowered by 0.1 $\hbar\omega_0$ relative to the $l = 1$ shells for both neutrons and protons, while for $N = 4$, the $1g_{9/2}$ shell has been lifted by 0.07 $\hbar\omega_0$ for the protons and lowered by 0.07 $\hbar\omega_0$ for the neutrons.

Table 5.9: Same as 5.5, except that the calculations are performed with the new Nilsson parameters.

	Nuclei	Spin range $\hbar$	Band 1 - Band 2	Energies (MeV)	Diff. (MeV)
$\nu(g_{9/2})$					
	^{57}Ni - ^{58}Ni	$\sim$ 17 - 23	SD1[2(+)1,21] - [2(+)1,22]B1a	-1.2, -1.3	-0.1
	^{58}Cu - ^{59}Cu	$\sim$ 17 - 23	SD[21,21] - [21,22]Band 5	-1.35, -1.35	0.0
	^{60}Zn - ^{61}Zn	$\sim$ 22 - 30	SD[22,22] - [22,23]SD1	-1.2, -1.2	0.0
	^{61}Zn - ^{62}Zn	$\sim$ 14 - 20	ND5b[11,01] - [11,02]TB2	-0.7, -0.6	0.1
		$\sim$ 22 - 28	SD1[22,23] - [22,24]SD3	-0.9, -0.3	0.6
			Avg.diff		0.12
$\pi(g_{9/2})$					
	^{58}Ni - ^{59}Cu	$\sim$ 14 - 18	D3a[20,11] - [21,11]8B	-0.1, -0.65	-0.55
	^{59}Cu - ^{60}Zn	$\sim$ 22 - 28	Band 5[21,22] - [22,22]SD	-1.5, -1.3	0.2
	^{61}Cu - ^{62}Zn	$\sim$ 20 - 26	Q4[21,02] - [22,02]WD	-0.6, -0.43	0.17
		$\sim$ 20 - 27	Q7b[21,1(+)2] - [22,1(+)2]WD5	-0.6, -0.6	0.0
			Avg.diff		-0.045
$\nu(f_{7/2})$					
	^{59}Ni - ^{58}Ni	$\sim$ 15 - 21	Band 1[20,01] - [20,11]D3	-0.15, -0.2	-0.05
		$\sim$ 14 - 22	Band 2[2(+)1,01] - [2(+)1,11]Q1b	-0.4, -0.55	-0.1
	^{58}Ni - ^{57}Ni	$\sim$ 15 - 22	B1a[21,22] - [21,21]SD1	-1.3, -1.2	0.1
	^{59}Cu - ^{58}Cu	$\sim$ 16 - 24	8A, 8B[21,11] - [21,21]SD	-0.9, -1.3	-0.4
			Avg.diff		-0.11
$\pi(f_{7/2})$					
	^{62}Zn - ^{61}Cu	$\sim$ 18 - 24	TB2[11,02] - [21,02]Q4	-0.7, -0.7	0.0
	^{59}Cu - ^{58}Ni	$\sim$ 22 - 28	Band 5[21,22] - [31,22]B3	-1.5, -1.5	0.0
			Avg.diff		0.0

Table 5.10: Same as 5.6, except that the calculations are performed with the new Nilsson parameters.

	Nucleus	Spin range $\hbar$	Band 1 - Band 2	Energies MeV	Diff. MeV
$\nu(g_{9/2})$					
	^{59}Cu	$\sim$ 18 - 24	6A[21,21] - [21,22]Band 5	$-1.0, -1.4$	-0.4
	^{62}Zn	$\sim$ 12 - 18	TB1a[11,01] - [11,02]TB2b	$-0.5, -0.4$	0.1
			Avg.diff		-0.15
$\pi(g_{9/2})$					
	^{58}Ni	$\sim$ 16 - 18	D3[20,11] - [21,11]Q1,2	0.0, -0.1	-0.1
	^{59}Ni	$\sim$ 14 - 18	Band 1[20,01] - [21,01]Band 2,3	$-0.1, -0.1$	0.0
	^{62}Zn	$\sim$ 19 - 23	TB2[11,02] - [1(+)2,02]WD4	$-0.7, -0.2$	0.5
		$\sim$ 19 - 23	WD7-6[21,02] - [22,02]WD1	$-0.2, -0.4$	-0.2
			Avg.diff		-0.01
$\nu(f_{7/2})$					
	^{61}Cu	$\sim$ 20 - 26	Q7[21,12]- [21,22]Q5	$-0.5, -0.7$	-0.2
		$\sim$ 20 - 26	Q4a,b[21,02] - [21,12]Q7a,b	$-0.5, -0.6$	-0.1
	^{62}Zn	$\sim$ 23 - 29	SD2[22,13] - [22,2(+)3]SD5	$-0.4, -0.7$	-0.3
		$\sim$ 20 - 30	WD1[22,02] - [22,12]WD5	$-0.5, -0.5$	0.0
			Avg.diff		-0.1
$\pi(f_{7/2})$					
	^{62}Zn	$\sim$ 12 - 16	ND6[01,01] - [11,01]TB1	$-0.5, -0.5$	0.0
		$\sim$ 15 - 19	ND9[01,02] - [11,02]TB2	$-0.6, -0.6$	0.0
		$\sim$ 20 - 25	WD4[12,02] - [22,02]WD1	$-0.2, -0.3$	-0.1
	^{58}Ni	$\sim$ 20 - 25	B1a[21,22] - [31,22]B3	$-1.2, -1.4$	-0.2
			Avg.diff		-0.07

Combining Tables 5.9 and 5.10, the average energy difference for all cases defined in Sec. 5.9.1 is close to zero, i.e., the new parameters give a much improved description of the relative properties of bands with similar configurations in neighbouring nuclei and in the same nucleus. The results with standard and new parameters are compared for the well established configurations in some of the nuclei in the following sections. A more complete comparision is presented in Ref. [65].

In a few cases the experimental bands have been reassigned to different configurations.

5.10.1 ^{62}Zn

For the low-spin band structures ND3, ND6, ND8, TB1 and TB2 with $I_{max} \leq 25\hbar$ of ^{62}Zn, the experimental energies with the rotating liquid drop energy subtracted are shown as a function of spin in the top panel of Fig. 5.31. The observed superdeformed bands SD1, SD2, SD3 and SD5 are shown in the top panel of Fig. 5.32. The middle panels of these figures show two sets of calculated bands, the red color set is drawn for standard parameters while the black color set is drawn for new Nilsson parameters, see Tables 5.7 and 5.8. The energy differences between calculations and experiment with the same color code as in middle panel are shown in the bottom panels. In the lower panel of Fig. 5.31, it can be seen that with the new Nilsson parameter set the low-spin bands (black color) lie on top of each other, more closely than the bands with the standard parameters (red color), which are more scattered. With the new parameter set, the difference for the ND8 band assigned to the configuration [00,02] gets larger than with standard parameters, which may suggests that another configuration should be assigned. Note also that the ND8 band is at a pretty high excitation energy which means that the relative energies of the yrast state in the $I \sim 10 - 20$ spin range are very well described by the new parameters. For the superdeformed bands SD1, SD2, SD3 and SD5 the calculations with new Nilsson parameters show some improvement compared with the calculations with the standard parameters, see the lower panel of Fig. 5.32. The black lines are closer together than the red lines. Note that as discuused above, the signature degenerate bands SD1 and SD2 are now assigned to the [22,13] configuration while in previous studies [17, 48], they were rather assigned to [22,2($\pm$)3]. Still some problems exist which appear to be independent of parameters. Thus, for the SD1,2 bands, there is a strong upslope in the differences in the lower panel of Fig. 5.32, which indicates that it is energetically too expensive to build high-spin states in the [22,13] configurations, where similar problems show up if the SD1 and SD2 are assigned to the [22,2($\pm$)3] configurations instead. Another problem is that the configura-

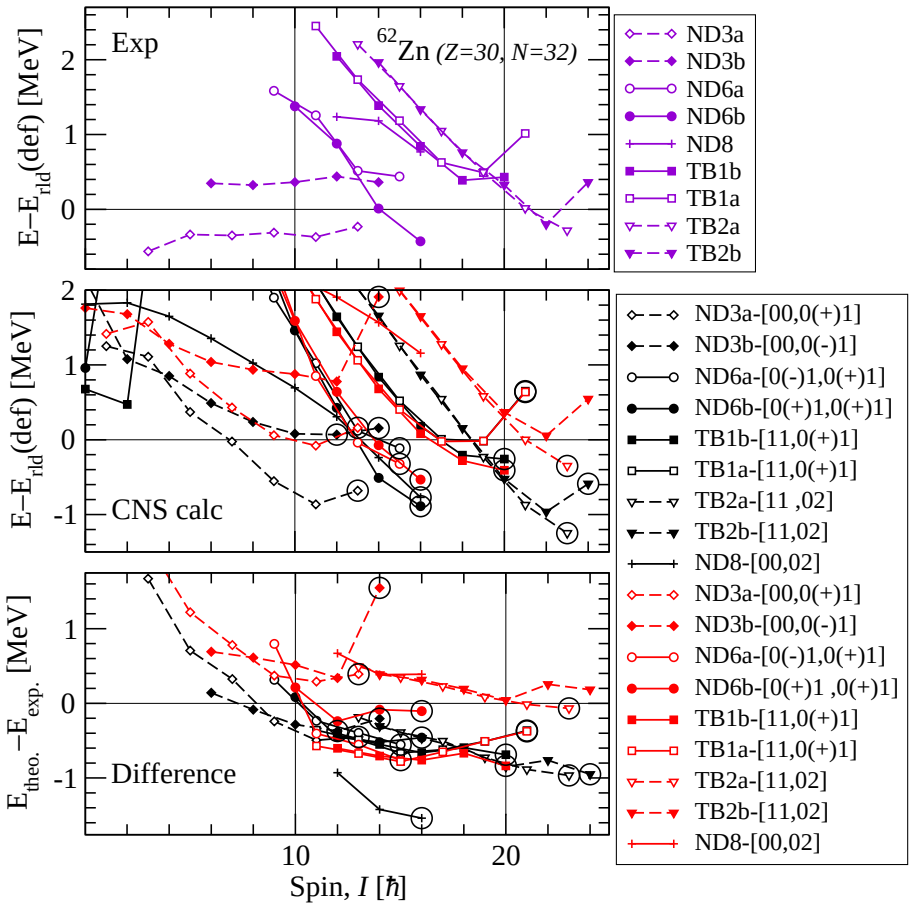

Figure 5.31: Differences between the low-spin band structures $I_{max} \leq 25\hbar$, in ^{62}Zn with both standard and new Nilsson parameter sets. All experimental bands are shown in the top panel. The middle panel shows the two sets of selected calculated bands, the red color set is for standard parameters while the black color set is drawn for new Nilsson parameters. The energy differences between calculations and experiment with the same color code as in middle panel are shown in the bottom panel.

tion which is calculated lowest [22,2(−)3] has no experimental counterpart.

The calculations with the new Nilsson parameter set for the well-deformed bands of ^{62}Zn are shown in Fig. 5.33. For these bands there are some

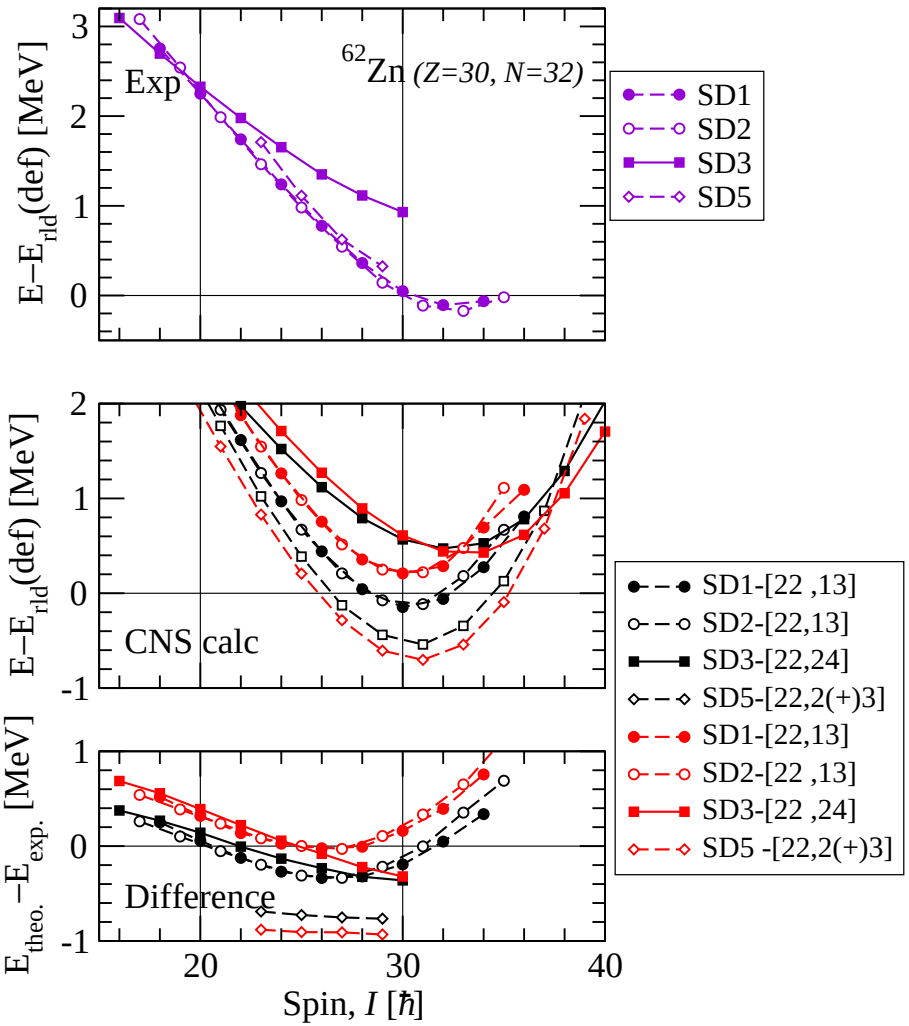

Figure 5.32: Same as Fig. 5.31, but drawn for superdeformed structures in ^{62}Zn.

changes of the configuration assignment relative to Ref. [17]. In previous studies [17], WD5 band was assigned to the [22,1(+)2] configuration, but with the new parameters, it is compared with the [22,1(−)2] configuration instead, which is calculated very close in energy. Previously assigned configurations to WD3 and WD7-6 are now interchanged, because of the reversed relative energies of the respective configurations with the new

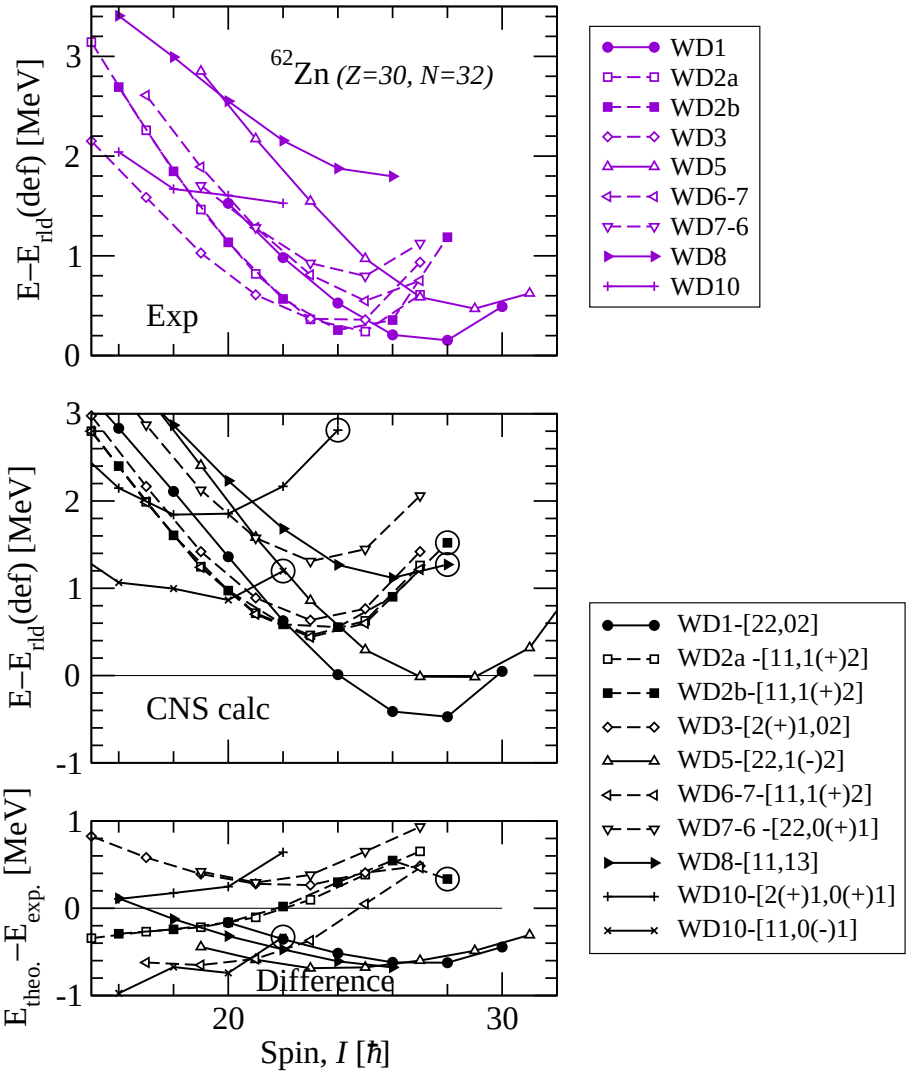

Figure 5.33: Same as Fig. 5.31, but drawn for well-deformed structures only with the new Nilsson parameter set in ^{62}Zn.

parameters. With the standard parameters, WD10 band has been assigned to [2(+)1,0(+)1] configuration, while with the new parameters, this band is in good agreement with the [11,0(−)1] configuration. With this assignemnet, the WD10 is seen to termination, which might explain the somewhat

uneven character of the observed energies.

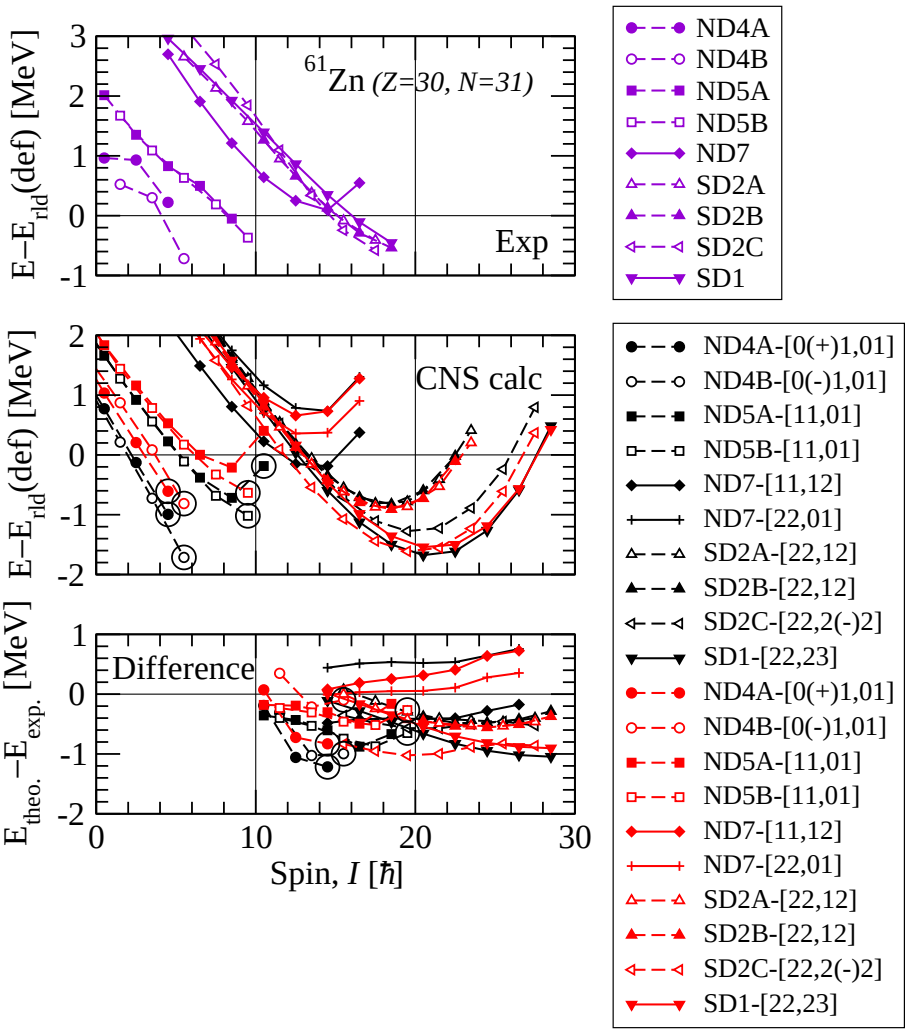

Figure 5.34: Same as Fig. 5.31, but drawn for selected band structures in ^{61}Zn. Note that ND7 is assigned to the [11,12] configuration, while the [22,01] configuration agrees better with standard parameters.

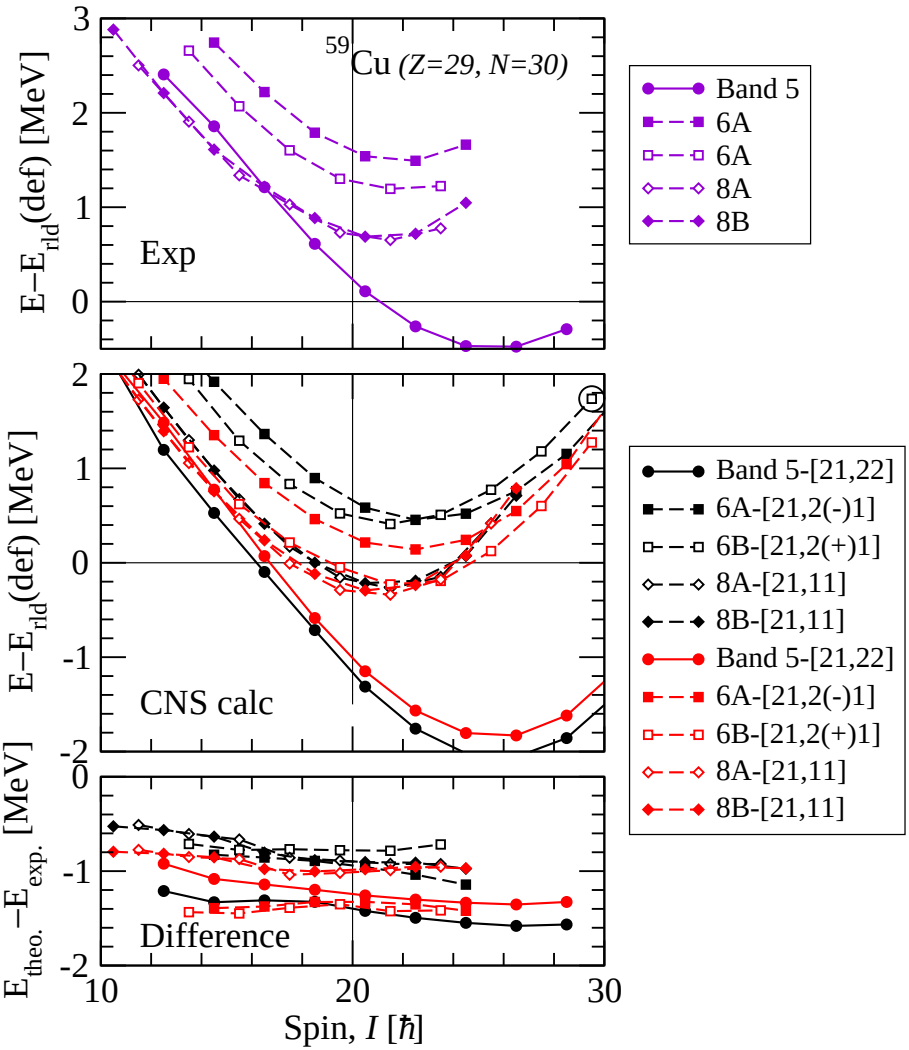

Figure 5.35: Same as Fig. 5.31, but drawn for selected band structures in ^{59}Cu.

5.10.2 ^{61}Zn

For the selected bands ND4A, ND4B, ND5A, ND5B, ND7, SD1, and SD2A, 2B, 2C of ^{61}Zn, the experimental energies with the rotating liquid drop energy subtracted are shown as a function of spin in the top panel of Fig. 5.34.

As already mentioned in Sec. 5.7.2, from the effective alignment method the tentatively assigned spins of SD2A, SD2B and SD2C are increased by $1\hbar$ as well as the excitation energies by 2 MeV. Fig. 5.34 is of the same type as Fig. 5.31, but drawn for selected bands in ^{61}Zn. With the new Nilsson parameters the two pairs of low-spin calculated signature partner bands $[0(\pm)1, 01]$ and [11,01] are much lower than with the standard parameters. With the new parameters SD2A and SD2B are in good agreement with the calculated signature partner bands [22,12], whereas SD2C is in good agreement with the calculated $[22, 2(-)2]$ band. With the new Nilsson parameters the ND7 band has been assigned to the new configuration [11,12], which is more yrast than the previously assigned configuration [22,01].

5.10.3 ^{59}Cu

With new parameters the differences between experiment and calculations for the two sets of signature partner bands 6A, 6B and 8A, 8B of ^{59}Cu are better collected and closer to zero than the calculations with the standard parameters. On the other hand, while the relative energies for band 5 leave no doubt about its interpretation, even larger values are calculated for the absolute differences with the new parameters.

5.10.4 ^{60}Ni

Similarly to Fig. 5.31, the experimental and calculated energies of selected bands M2a, M2b, WD1a, WD1b, WD2 and WD3 of ^{60}Ni are compared in Fig. 5.36. The results with the new parameters for M2a, M2b, WD1a, WD1b agree better than the calculations with standard parameters.
The parity of WD2 band was already discussed in the section 5.8. With the new parameters, the previously assigned configuration [31,0(+)1] for WD2 band with positive parity, leads to large differences between experiment and calculations, strongly supporting the conclusion that the parity of WD2 band is negative. With the new parameters, the WD2 band with negative parity is in good agreement with the [2(+)1, 02] configuration. Furthermore, with the standard parameters, the WD3 band with positive parity has been assigned to the [2(+)1,0(+)1] configuration. However, with such an interpretation, the differences between experiment and calculations become large at lower spin values. These differences become smaller with a [20,02] interpretation. With the new parameters, the [20,02] configuration comes lower at lower spin values in closer agreement with the observed WD3 band.

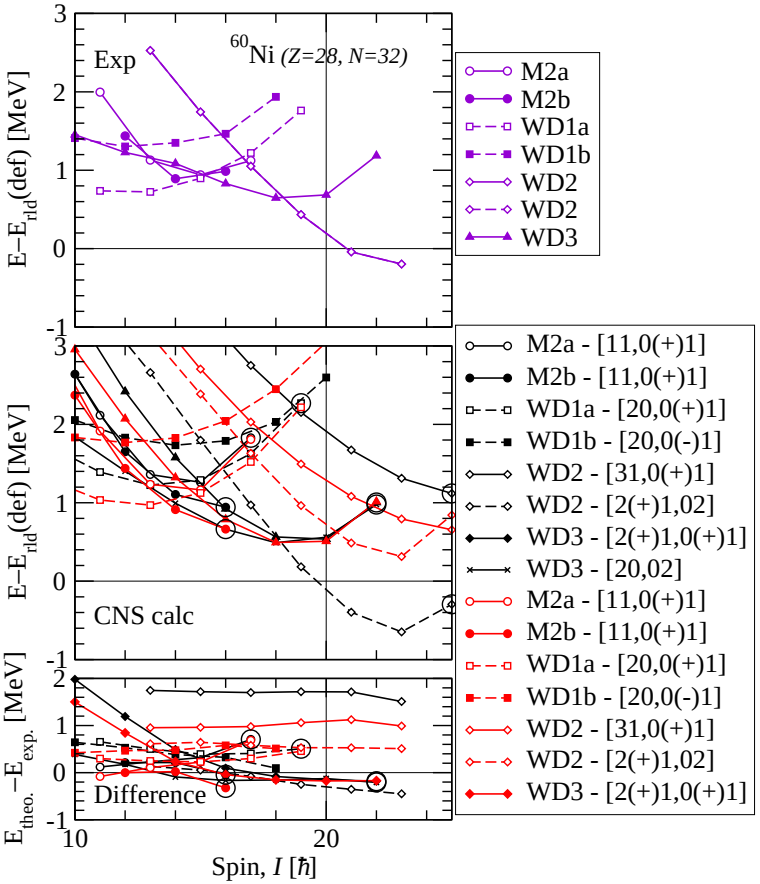

Figure 5.36: Same as Fig. 5.31, but drawn for selected band structures in ^{60}Ni. Note that with the new parameters, the preferred interpretation of the WD2 and WD3 band is [2(+)1,02] and [20,02], respectively, and the comparision with the [31,0(+)1] and [2(+)1,0(+)1] configuration is included only to show the larger differences.

Chapter 6

Conclusions and Outlook

The combined data from four different fusion-evaporation reaction experiments has been used to construct and analyse the excitation scheme of the nucleus ^{62}Zn. The resulting level scheme comprises some 250 energy levels and 430 γ-ray transitions. The proposed maximum spin is $I = 35\ \hbar$ at an excitation energy of $E_x = 42.5$ MeV; numbers comparable only to ^{58}Ni [13, 32]. One important result is that the configuration assignment puzzle has been solved for the first superdeformed band observed in the $A \sim 60$ region [8, 48] .

Next to previous results [8, 19], the present study includes a number of low-spin, normally deformed structures, ten new well-deformed rotational bands, and four additional superdeformed bands. These are summarized and presented in more depth in three publications of this thesis (Papers I, II and III). The combination of the GAMMASPHERE γ-ray spectrometer and ancillary particle detection systems allowed for the connection of rotational bands to well-known, low-lying excited states in ^{62}Zn. Several physics aspects have been observed in ^{62}Zn, like all kinds of band termination: structures ND9 and TB2 are nice examples of favoured and unfavoured band terminations while WD1 corresponds to a non-terminating band. The superdeformed bands, SD1-SD4 with strong collectivity, till their maximum spin values and favoured terminating states; examples are the 16^+ state from structure ND6, the 17^+ state from ND7, or the 19^- state from ND9. All these are fed by a large number of weak transitions as first seen in ^{157}Er [79].

Like for SD bands at $A \sim 150$ region, it is possible in the $A \sim 60$ region to follow the configurations with increasing particle number by adding one particle in a specific orbital [74, 80]. A unique quality of this mass region is to follow the configurations from close-to-spherical to large deformations from successive excitations of holes and particles.

The experimental characteristics of the rotational bands are analyzed and compared with results from Cranked Nilsson-Strutinsky calculations. Most of the structures are characterized by means of these calculations, where it is concluded that the low-spin normal deformed structures have no holes in the $1f_{7/2}$ orbitals, the two known terminating bands have one hole, the well-deformed bands have two holes and finally the superdeformed bands have three to four holes in the $1f_{7/2}$ orbitals. With more particles in the high-j $1g_{9/2}$ orbitals the terminating sequences become more down-sloping, when drawn relative to the rotating liquid drop reference, i.e., they are more favoured in energy at high-spin states. More holes in the high-j $1f_{7/2}$ orbitals on the other hand lead to terminating sequences with a large curvature, corresponding to small moments of inertia.

The effective alignment method has been applied to check out the spin, parity and theoretical configuration assignments of the existing experimental bands and thereby identify the behaviour of the band structures in the $A \sim 60$ mass region. Confirmed experimental bands and their theoretical configuration assignments are used to investigate an improved Nilsson parameter set in the $A \sim 60$ mass region. These new Nilsson parameters gave an improved overall description of data. With the new parameters, where the $l = 3$, $1f_{5/2}$ and $1f_{7/2}$ orbitals are lowered by approximately 1 MeV relative to the $l = 1$, $2p_{3/2}$ and $2p_{1/2}$ orbitals, the crossing between two calculated SD bands with two and three $f_{7/2}$ holes, respectively in ^{58}Ni comes at the correct energy (see more details in paper IV). However, preliminary results from ^{63}Ni suggests that a similar crossing in that nucleus is reproduced if only the $Z = 28$ gap decreased by $0.07\hbar\omega$ (see more details in paper V). These findings suggest that the $Z = 28$ gap is reduced by approximately 1 MeV when going from ^{58}Ni ($N = 30$) to ^{63}Ni ($N = 35$). This way of determining the gap from crossing frequencies between orbitals at high frequencies has advantage that it is calculated from essentially pure single-particle properties and therefore independent of e.g. pairing correlations.

As a future aspect it is important to do more investigations on superdeformed bands, which are still unclear at highest spin states, for examples, SD1 and SD2 bands of ^{62}Zn [17, 48] in this $A \sim 60$ mass region. For a better understanding of these bands, an alternative could be to reach high angular momentum in, for example, ^{61}Zn and ^{61}Cu and to definitely link the SD bands in these nuclei.

With the combination of new large arrays of detectors, such as AGATA (Advanced Gamma-ray Tracking Array) in Europe and GRETA (Gamma-Ray Energy Tracking Array) in the USA, and either high intensity stable beams or exotic radioactive ion beams, it will be possible to address the nuclear structure and nuclear astrophysics problems in the $A \sim 60$ mass

region in more detail. Some interesting scientific problems are:

⋆ More comprehensive γ-ray spectroscopy studies of neutron-deficient nuclei in the direct neighbourhood of ^{56}Ni, namely ^{55}Ni [81] and ^{57}Cu [82].
⋆ Study of low-lying proton unbound states and possible unclear astrophysics impact in primarily ^{57}Cu [83], ^{61}Ga and ^{65}As.
⋆ Search for SD bands in ^{57}Cu [82], ^{58}Zn [84], ^{59}Zn [85] and ^{61}Ga [86]. These will allow their comparison with analogue SD bands in their mirror partners, ^{57}Ni [68], ^{58}Ni [32], ^{59}Cu [14] and ^{61}Zn [16], respectively.
⋆ Isoscalar $T = 0$ properties at high spin in $N \approx Z$ nuclei.
⋆ Quest for more SD bands in more neutron-rich nuclei, for example, near ^{68}Zn [87]. These studies can give the evolution of shell gaps at $Z = N = 28$ and $N = 40$ with increasing neutron numbers, and provide links to the $A \sim 80$ SD region due to $h_{11/2}$ occupancies.

These studies will allow to test and challenge the present nuclear models at the limits of nuclear existence.

Popular Summary

All ordinary matter around us is made out of atoms. In turn, the building blocks of the atoms are nowadays known to be three types of particles: electrons, protons and neutrons. The latter are called nucleons, as they together form the positively charged nucleus of the atom, around which the electrons are moving. The radius of the nucleus is about three orders of magnitude smaller than that of the atom, while it comprises almost all its mass. The name of a chemical element relates to the number of protons inside the nucleus, while different numbers of neutrons can give rise to various isotopes of a certain element. To overcome the Coulomb repulsion amongst the protons inside the nucleus, there is the need for another fundamental force — the strong nuclear force.

To explain the properties of atomic nuclei, one needs an understanding of the forces acting between the nucleons. However, these forces are very complicated and still not known in all aspects. Here, the study of nuclei at extreme conditions, like, high excitation energy, high angular momenta, or at unusual proton to neutron ratios, can contribute to a better understanding of specific aspects of the nuclear force. It is also important to understand that nuclei can become deformed, i.e. nuclei at large deformation (or funny shapes like bananas or pears rather than spheres) is another example of extreme conditions. Ultimately, the deformation of nuclei are mainly determined by the quantum mechanical shell structure of the protons and neutrons which are described as moving in specific orbitals inside the nucleus. The shell structure is closely related to symmetries and becomes particularly strong at the highly symmetric spherical shape. However, the shell structure can be partly restored at specific deformations, for example at superdeformation corresponding to an axial shape with a 2:1 ratio between the long axis and the perpendicular axes.

To describe and simulate the outcome of experiments, it is necessary to compare experimental results with theoretical calculations, and thereby test and improve the present nuclear models. In this work, the level scheme of ^{62}Zn (with 30 protons and 32 neutrons) has been observed in great de-

tail, leading to one of the most complex and comprehensive excitation scheme ever deduced. It includes few hundreds of excited states with a 'world record' discrete quantum state at 42.5 MeV excitation energy. This energy is mainly stored as rotational energy, and it makes the nucleus ^{62}Zn rotate with a frequency of $f = 500000000000000000$ revolutions per second ($f = 5 \cdot 10^{20}$/s).

The experimental results are probed with the 'Cranked Nilsson Strutinsky model', where the nucleons move in an anisotropic harmonic oscillator potential generated by the other nucleons, and with two additional terms which are dependent on the orbital and internal motion of the nucleons. A more global assessment of rotational bands in nuclei near ^{62}Zn leads to a modification of parameters, i.e. a change of the strengths of these two terms. This leads in turn to an improved knowledge of the energies of various proton and neutron orbitals and thus contributes to the improved understanding of atomic nuclei.

Acknowledgments

With great pleasure, I take this opportunity to put my gratitude to all those who have contributed towards this thesis in various ways.
It is difficult to overstate my gratitude to my supervisor, Professor Dirk Rudolph, without whom this thesis would not have been possible. I have been very fortunate to have the privilege of working with him. Enlightening discussions, many hours spent in front of the computer, and great deal of effort put in reading this thesis are only few of the many things I am obliged for.
I also would like to thank my co-supervisor Professor Ingemar Ragnarsson for giving me the opportunity to contact the Lund Nuclear structure Group and for teaching me about CNS calculations as well as the all the things regarding physics. I feel very grateful to you both for always showing interest in my work, for your continuous encouragement and especially for correcting my thesis. I would also like to thank my other co-supervisor Professor Claes Fahlander for his support on this thesis. I am especially greatful to Gillis Carlsson for the time he spent on helping me to understand the physics behind the theoretical calculations. I am specially thankful to Prof. S.C. Pancholi and Prof. A.K. Jain, who introduce my carrier in nuclear physics.
It is a pleasure to thank all my friends, especially Douglas DiJulio and Ulrika Forsberg for their help. I am also thankful to the rest of the people working in and together with the Nuclear Structure Group and Mathematical Physics group in Lund. A special thanks goes to Lise-Lotte Andersson for her quick answers through mail. I am very thankful to Cecilia for her great advises and suggestions. I would also like to thank my Indian friends Shilpi, Tripta, Tanya, Milli, Madhu, Juveria and Rama for their fruitful company during my Ph.D time. I am also thankful to Amritanshu Shukla for his help at the final stage of my thesis.

Finally, I would like to convey my sincere gratitude to my dear husband Sandeep Kumar, my lovely daughter Saanvi and my family members for always standing by me and support me. There are no words to express my feelings towards my dear brother Vasu Dev, who always encourages me to built a good carrier in science.

Bibliography

[1] A.V. Afanasjev, D.B. Fossan, G.J. Lane, and I. Ragnarsson, Phys. Rep. **322**, 1 (1999).

[2] http://www.aip.org/png/html/shapes.htm.

[3] T. Troudet and R. Arvieu, Phys. Lett. **B82**, 308 (1979).

[4] I. Ragnarsson, Phys. Lett. **B199**, 317 (1987).

[5] S.M. Polikanov *et al.*, Sov. Phys. JETP **15**, 1016 (1962).

[6] C. Andreoiu, PhD thesis, Lund University, ISBN 91-628-5308-2 (KFS AB, Lund, 2002).

[7] C.E. Svensson *et al.*, Phys. Rev. Lett. **85**, 2693 (2000).

[8] C.E. Svensson *et al.*, Phys. Rev. Lett. **79**, 1233 (1997).

[9] C. Baktash *et al.*, Phys. Rev. Lett. **74**, 1946 (1995).

[10] P.J. Nolan *et al.*, J. Phys. G **11**, L17 (1985).

[11] P.J. Twin *et al.*, Phys. Rev. Lett. **57**, 811 (1986).

[12] E.F. Moore *et al.*, Phys. Rev. Lett. **63**, 360 (1989).

[13] E.K. Johansson *et al.*, Phys. Rev. C **80**, 014321 (2009).

[14] C. Andreoiu *et al.*, Eur. Phys. J. **A14**, 317 (2002).

[15] L.-L. Andersson *et al.*, Eur. Phys. J. **A36**, 251 (2008).

[16] L.-L. Andersson *et al.*, Phys. Rev. C **79**, 024312 (2009).

[17] J. Gellanki *et al.*, Phys. Rev. C **86**, 034304 (2012).

[18] C.E. Svensson *et al.*, Phys. Rev. Lett. **82**, 3400 (1999).

[19] C.E. Svensson *et al.*, Phys. Rev. Lett. **80**, 2558 (1998).

[20] I. Ragnarsson *et al.*, Phys. Rev. Lett **74**, 3935 (1995).

[21] C. Andreoiu *et al.*, Phys. Rev. Lett. **89**, 022501 (2002).

[22] B. Cederwall *et al.*, Nature **469**, 68-71 (2011).

[23] http://nucalf.physics.fsu.edu/ ∼riley/gamma/.

[24] G.F. Knoll, "Radiation and Measurement", 2nd edition, John Wiley & Sons, New York (1989).

[25] I.-Y. Lee, Nucl. Phys. **A520**, 641c (1990).

[26] EUROBALL *III*, A European γ-ray facility, Eds. J. Gerl and R.M. Lieder, GSI 1992.

[27] http:// axpd30.pd.infn.it/GASP/.

[28] D.G. Sarantites *et al.*, Nucl. Instrum. Meth. **A381**, 418 (1996).

[29] http://wunmr.wustl.edu/ ∼dgs/mball/.

[30] D. Rudolph *et al.*, Phys. Rev. Lett. **89**, 022501 (2002).

[31] D.A.Torres *et al.*, Phys. Rev. C **78**, 054318 (2008).

[32] D. Rudolph *et al.*, Phys. Rev. Lett. **96**, 092501 (2006).

[33] L.-L. Andersson, PhD thesis, Lund University, ISBN 978-91-628-7584-8 (KFS AB, Lund, 2008).

[34] E.K. Johansson, PhD thesis, Lund University, ISBN 978-91-628-7679-1 (KFS AB, Lund, 2009).

[35] M. Devlin *et al.*, Nucl. Instrum. Meth. **A383**, 506 (1996).

[36] C.E. Svensson *et al.*, Nucl. Instrum. Meth. **A396**, 288 (1997).

[37] D. C. Radford, Nucl. Instrum. Meth. **A361**, 297 (1995).

[38] J. Theuerkauf, S. Esser, S. Krink, M. Luig, N. Nicolay, O. Stuch, H. Wolters, Program Tv, University of Cologne, unpublished.

[39] D. Seweryniak *et al.*, Nucl. Instrum. Meth. **A340**, 353 (1994).

[40] B. Cederwall *et al.*, Nucl. Instrum. Meth. **A354**, 591 (1995).

[41] K.S. Krane, R.M. Steffen, and R.M.Wheeler, At. Data Nucl. Data Tables **11**, 351 (1973).

[42] H.J. Rose and D. Brink, Rev. Mod. Phys. **39**, 306 (1967).

[43] D. Rudolph *et al.*, Eur. Phys. J. **A4**, 115 (1999).

[44] J.F. Bruandet, Tsan Ung Chan, M. Agard, J.P. Longequeue, C. Morand, and A. Giorni, Z. Phys. **A 279**, 69 (1976).

[45] L. Mulligan, R. W. Zurmuhle, D. P. Balamuth, Phys. Rev. C **19**, 1295 (1979).

[46] N.J. Ward, L.P. Ekström, G.D. Jones, F. Kearns, T.P. Morrison, O.M. Mustaffa, D.N. Simister, P.J. Twin, and R. Wadsworth, J. Phys. G **7**, 815 (1981).

[47] K. Furutaka *et al.*, Z. Phys. **A 358**, 279 (1997).

[48] J. Gellanki *et al.*, Phys. Rev. C **80**, 051304(R) (2009).

[49] I. Ragnarsson, Z. Xing, T. Bengstsson, and M. A. Riley, Phys. Scr. **34**, 651 (1986).

[50] O. Haxel, J.H.D. Jensen, and H.E. Suess, Phys. Rev. **75**, 1766 (1949).

[51] M.G. Mayer, Phys. Rev. **75**, 1969 (1949).

[52] S.G. Nilsson, Dan. Mat. Fys. Medd. **29**, no. 16 (1955).

[53] S. G. Nilsson, I. Ragnarsson, Shapes and Shells in Nuclear Structure (Cambridge University Press, 1995).

[54] S. G. Nilsson *et al.*, Nucl. Phys. **A131**, 1 (1969).

[55] C. Gustafsson, I.L. Lamm, B. Nilsson and S.G. Nilsson, Ark. Fys. **36**, 613 (1967).

[56] D.R. Inglis, Phys. Rev. C **96**, 1059 (1954).

[57] D.R. Inglis, Phys. Rev. C **103**, 1786 (1956).

[58] T. Bengtsson and I. Ragnarsson, Nucl. Phys. **A436**, 14 (1985).

[59] B.G. Carlsson and I. Ragnarsson, Phys. Rev. C **74**, 011302(R) (2006).

[60] S.E. Larsson, Phys. Scr. **8**, 17 (1973).

[61] V.G. Zelevinskii *et al.*, J. Nucl. Phys. **22**, 565 (1975).

[62] K. Pomorski and J. Dudek, Phys. Rev. C **67**, 044316 (2003).

[63] V.M. Strutinsky, Nucl. Phys. **A95**, 420 (1967).

[64] G. Andersson *et al.*, Nucl. Phys. **A268**, 205 (1976).

[65] J. Gellanki *et al.*, to be submitted.

[66] E.K.Johansson *et al.*, Phys. Rev. C **77**, 064316 (2008).

[67] W. Satula *et al.*, Phys. Rev. C **81**, 054310 (2010).

[68] D. Rudolph *et al.*, J. Phys. G: Nucl. Part. Phys. **37**, 075105 (2010).

[69] C.H. Yu *et al.*, Phys. Rev. C **65**, 061302(R) (2002).

[70] D. Rudolph *et al.*, Eur. Phys. J. **A14**, 137 (2002).

[71] A.V. Afanasjev *et al.*, Phys. Rev. C **59**, 3166 (1999).

[72] I. Ragnarsson, Phys. Lett. **B264**, 5 (1991).

[73] A.V. Afanasjev and I. Ragnarsson, Nucl. Phys. **A628**, 508-596 (1998).

[74] I. Ragnarsson, Nucl.Phys. **A557**, 167c (1993).

[75] C.H. Yu *et al.*, Phys. Rev. C **60**, 031305(R) (1999).

[76] I. Ragnarsson, Nucl. Phys. **A520**, 67c (1990).

[77] C. Gustafsson, I.L. Lamm, B. Nilsson and S.G. Nilsson, Ark. Fys. **36**, 613(1967).

[78] B.G. Carlsson, Master thesis, Lund Institute of Technology, 2003, Lund-Mph-03/01.

[79] A.O. Evans *et al.*, Phys. Rev. Lett. **92**, 252502 (2004).

[80] W. Nazarewicz and I. Ragnarsson, Handbook of Nuclear Properties, edited by D. N. Poenaru and W. Greiner(Clarendon Press, Oxford, 1996), p. 80.

[81] D. Rudolph *et al.*, Z. Phys. **A 37**, 379 (1997).

[82] C.L. Jiang *et al.*, Phys. Rev. C **80**, 044613 (2009).

[83] X.G. Zhou *et al.*, Phys. Rev. C **53**, 982 (1996).

[84] A. Parikh *et al.*, Astroph. Jour. Suppl. Series **178** 110 (2008).

[85] C. Andreoiu *et al.*, Eur. Phys. J. **A15**, 459 (2002).

[86] L.-L. Andersson *et al.*, Phys. Rev. C **71**, 011303(R) (2005).

[87] M. Devlin *et al.*, Phys. Rev. Lett. **82**, 5217 (1999).